

**Final Report #1
(STTR Phase I)
“Theoretical Innovations in Combustion Stability Research:
Integrated Analysis and Computation”**

Period: 15 June 2010-14 March 2011
Contract FA9550-10-C-0088
Cage Code 5STP5

Kassoy Innovative Science Solutions
David R. Kassoy, Owner
Josette Bellan, JPL Collaborator

Date: 14 April 2011

Technical Monitor: Mitat Birkan
AFOSR/RSA
875 N. Randolph St., Suite 325, Rm. 3112
Arlington VA 22203-1768

Abstract

The Final Report contains a comprehensive description of the Phase I research effort by KISS and JPL personnel. Results obtained in the context of the project objectives cited in the Phase I proposal are described in an abbreviated form in an Executive Summary and in complete detail in technical papers in the Appendix. Assessments of technical feasibility are described in terms of value to the AFRL.

Report Documentation Page				Form Approved OMB No. 0704-0188	
Public reporting burden for the collection of information is estimated to average 1 hour per response, including the time for reviewing instructions, searching existing data sources, gathering and maintaining the data needed, and completing and reviewing the collection of information. Send comments regarding this burden estimate or any other aspect of this collection of information, including suggestions for reducing this burden, to Washington Headquarters Services, Directorate for Information Operations and Reports, 1215 Jefferson Davis Highway, Suite 1204, Arlington VA 22202-4302. Respondents should be aware that notwithstanding any other provision of law, no person shall be subject to a penalty for failing to comply with a collection of information if it does not display a currently valid OMB control number.					
1. REPORT DATE 14 APR 2011		2. REPORT TYPE Final		3. DATES COVERED 15-06-2010 to 14-04-2011	
4. TITLE AND SUBTITLE Theoretical Innovations in Combustion Stability Research: Integrated Analysis and Computation				5a. CONTRACT NUMBER FA9550-10-C-0088	
				5b. GRANT NUMBER	
				5c. PROGRAM ELEMENT NUMBER	
6. AUTHOR(S) David Kassoy; Josette Bellan				5d. PROJECT NUMBER	
				5e. TASK NUMBER	
				5f. WORK UNIT NUMBER	
7. PERFORMING ORGANIZATION NAME(S) AND ADDRESS(ES) Kassoy Innovative Science Solutions (DRK), Jet Propulsion Laboratory (JB), 000, Wright Patterson AFB, OH, 45433				8. PERFORMING ORGANIZATION REPORT NUMBER ; AFRL-OSR-VA-TR-2011-0201	
9. SPONSORING/MONITORING AGENCY NAME(S) AND ADDRESS(ES) AFOSR, 875 North Randolph Street, Suite 325, Arlington, VA, 22203				10. SPONSOR/MONITOR'S ACRONYM(S)	
				11. SPONSOR/MONITOR'S REPORT NUMBER(S) AFRL-OSR-VA-TR-2011-0201	
12. DISTRIBUTION/AVAILABILITY STATEMENT Approved for public release; distribution unlimited					
13. SUPPLEMENTARY NOTES					
14. ABSTRACT The final report contains a comprehensive description of the Phase I research effort by KISS and JPL personnel.					
15. SUBJECT TERMS Combustion, Thermomechanics, Turbulent Reacting Flow, Supercritical Gases, Rocket Engine Stability					
16. SECURITY CLASSIFICATION OF:			17. LIMITATION OF ABSTRACT Same as Report (SAR)	18. NUMBER OF PAGES 106	19a. NAME OF RESPONSIBLE PERSON
a. REPORT unclassified	b. ABSTRACT unclassified	c. THIS PAGE unclassified			

Table of Contents

1. Executive Summary.....	3
a. Phase I Program Objectives	
b. Phase I Research Accomplishments	
2. Bibliography.....	8
3. Appendix.....	9
a. The sub-grid scale scalar variance under supercritical pressure conditions, E. Masi and J. Bellan, submitted for publication, February 2011	
b. Thermomechanical response of a reactive gas to extremely rapid transient, spatially distributed energy addition: An asymptotic formulation, D.R. Kassoy and K. Wojciechowski, to be submitted for publication, May 2011	

1. Executive Summary

a. Phase I Program Objectives¹

1. Demonstrate the feasibility of formulating a nontraditional model of LRE stability in terms of well-known thermomechanical system principles, with the potential to provide quantitative predictions of combustion stability in an idealized engine configuration.
2. Demonstrate that the thermomechanical approach can be used to establish a direct correspondence between distributed, transient heat addition and mechanical (wave) disturbance growth in a semi-confined geometry.
3. Formulate stability concepts attributable to thermomechanics in a semi-confined system.

During the nine month Phase I contract period (15June2010-14March2011) the research program has focused on:

- an evaluation of the flamelet concept application as currently implemented to supercritical turbulent flows [1], and
- a quantitative thermomechanical formulation for gas motion and acoustic disturbances induced by localized, spatially distributed, transient heat addition, including that from exothermic chemical reactions, as a metaphor for physical and chemical phenomena occurring in a liquid rocket engine (LRE) combustion chamber,

to demonstrate the feasibility of the objectives cited above. Summaries of the results obtained and their technical value to the AFRL are given in b. below, based on the detailed technical papers in the Appendices.

¹ From the Phase I proposal to AFOSR (Sept. 2009)

b. Phase I Research Accomplishments

b.1-Flamelet concept application to supercritical flows

The focus of this study was on the examination of the subgrid-scale (SGS) scalar variance, as related to the potential utilization of flamelet models under supercritical conditions.

We first addressed the issue of the SGS scalar variance, σ_Z , as related to the LES modeling of the turbulent reaction through the flamelet model. Although we do not have yet a database of reactive turbulent supercritical flows, since the flamelet model relies on the definition of a conserved scalar Z , we have the necessary information from our previous species-mixing study to perform the investigation; if a conserved scalar can be defined for the reactive flow situation, because of the additional coupling due to reaction, this scalar is expected to have a more complex behavior than the present one resulting only from mixing, so the results of this study are conservative in terms of the level of difficulty to model the scalar variance.

In a first step of the study, we derived the σ_Z equation [1, 2] in two forms. The first form highlighted the new terms in the equation with respect to the atmospheric-pressure conditions case, and the second form emphasized the new SGS terms in the equation that would require modeling, as well as identified the nature of each term (i.e. production or dissipation). The result of assessing the activity of all terms in the two equations was to identify two new SGS terms that have comparable magnitude to the classical terms and thus cannot be neglected: (i) a SGS diffusion term, and (ii) a SGS Soret term that has a dissipative effect. Given the lack of models for these terms, it was decided that trying to model them in the σ_Z equation for the purpose of solving the equation was bound to be an unrewarding approach, and instead, it was decided to propose direct models for σ_Z . Examination of the database over several binary-species systems revealed that indeed the PDF of Z is best approximated by a β PDF, which justified investing time in modeling σ_Z since the PDF can be constructed from its mean provided by the LES solution and a model of σ_Z .

Thus, in the second step of the study we explored two models for σ_Z : (1) the approximate deconvolution model (ADM), and (2) a dynamic gradient-based (GRD) model. These models are conceptually different as ADM relies on a mathematical derivation with no assumptions required regarding the nature of the scale interactions, while the GRD relies on the mixing-length hypothesis in conjunction with an equilibrium assumption. The ADM is generally very good to excellent at relatively small filter widths, but as the filter width becomes large, there is evidence that the series expansion on which ADM relies does not converge with increasing order of approximation, as an overshoot becomes increasingly visible with increasing filter width. Thus, ADM should be considered here as an approximation rather than a converging procedure to obtain σ_Z , and in this particular case an approximation order of 3 is recommended. For the GRD-based model, we formulated a new model which we exercised and compared to

the results obtained with a classical model in conjunction with two approximations for the filter width. Compared to the classical model which increasingly departs from the filtered DNS template with either type of filter approximation, our model maintains high fidelity even at very large filter widths and in a range where test filtering is performed close to the production range of wavenumbers.

A manuscript has been submitted for publication [1] and a presentation [2] has been made at a national conference of this subject.

b.2-Thermomechanics of reactive gases

Transient, spatially distributed combustion in a turbulent flow is thought to be the source of acoustic and stronger mechanical disturbances in a LRE chamber. Surprisingly, a quantitative model for mechanical wave generation in a transient, spatially distributed reacting flow does not appear to be available in the technical literature. As a first step in the development of such a theory, Kassoy [3] describes a thermomechanics-based study to identify a quantitative relationship between time resolved, localized power deposition into a finite volume of **inert** gas and the magnitude of acoustic or stronger disturbances generated in the neighboring unheated, unconfined gas. The results demonstrate that the thermomechanical response of the heated gas depends on a complex relationship between the magnitude of energy deposited and the time scale for that deposition, but not simply on the power deposition alone. The theory is limited to heating time scales small compared to the acoustic time of the volume, a condition necessary for the pressure to rise with temperature (while the density change is marginal). When the energy deposition is quantitatively limited, nearly constant volume heating occurs (near-inertial confinement), characterized by a small internal gas expansion Mach number, defined with respect to the high temperature hot spot speed of sound. Temperature and pressure rise together within the hot spot. Localized high pressure, relative to that in the cold neighboring gas, is necessary to create the pressure gradient source of induced mechanical motion (both fluid speed and acoustic disturbances). Gas expelled from the boundary of the hot spot (the “piston effect”) is the source of mechanical disturbances in the unheated environmental gas. The expelled gas Mach number, measured with respect to the cold gas speed of sound will be exceptionally small when the energy deposition is sufficiently small relative to the quantitative limitation referred to above. The resulting mechanical disturbances in the cold environment are linear acoustic waves. Larger energy deposition within the quantitative limitation is associated with much larger expelled gas Mach numbers and significantly stronger shock wave propagation in the cold environmental gas. Beyond the quantitative limitation referred to above, the heating process is fully compressible, characterized by a very large internal Mach number. The asymptotic theory demonstrates that this type of thermomechanical response to energy deposition is the source of strong blast waves [4] in the unheated external environment. The formulation in Ref. 3 has been generalized during the Phase I program to examine thermomechanical effects in a reactive gas with one-step kinetics [5]. The complete technical description appears in Appendix 3.b

The primary objective of the study in Ref. 5 is to quantify the thermomechanical response of a reactive gas affected by a localized exothermic chemical reaction. Relative to the objectives of the Phase I program cited above, this type of theory provides fundamental insights into the sources of mechanical disturbances within a LRE chamber containing a turbulent reacting flow. Crucial length and time scales, as well as dominant physico-chemical processes derived from an asymptotic formulation may be employed by numerical modelers to fully resolve transient reactive flow phenomena and to produce reliable predictions of combustion stability in realistic LRE configurations.

The theory in Ref. 5 is formulated for a subcritical gas with one-step, high activation energy exothermic kinetics. The asymptotic formulation demonstrates that the thermomechanical response of a reactive gas to localized, rapid² chemical heat addition is similar in nature to that for an inert gas with external heating [3]. Nearly inertially-confined heating occurs only when the chemical heat release and the high activation energy are quantitatively restricted. Within that limitation one finds linear acoustic wave generation for the smallest range of energy addition and stronger wave generation for more significant energy deposition.

Numerical solutions to the equations describing the nearly-inertially confined reaction-generated heat addition process show that a spatially distributed reaction wave appears spontaneously in the hottest portion of the hot spot, and propagates through the relatively slowly moving fluid at a supersonic speed, relative to the hot gas speed of sound. As the front nears the much colder boundary of the hot spot it decelerates significantly and steepens considerably. The configuration evolves toward a discontinuous front separating hot, high-pressure, burned gas on one side from cold, low pressure reactant on the other side. Although the pressure, temperature and reactant concentration jumps across the front are reminiscent of a reactive shock wave, the front does not propagate at a supersonic speed relative to the unburned cold reactant near the boundary of the hot spot. In fact, during the relevant heating time scale the entire process occurs in a nearly incompressible medium. Fluid expelled from the hot spot boundary acts as source of mechanical disturbances propagating into the neighboring cold gas. The amplitude of those disturbances depends upon the energy addition level during the reactive phase of the hot spot.

In analogy with the inert gas results, a fully compressible heat addition process occurs when the chemical energy addition exceeds the quantitative restriction referred to above. The internal expansion Mach number, defined relative to the hot gas speed of sound is substantial and can be supersonic. The hot spot transients must be determined from a numerical solution to the compressible, reactive, gasdynamic equations, to be completed in the future.

In summary, an asymptotic formulation of the reactive hot spot problem has been developed to quantify the thermomechanical response of reactive gas to localized energy addition on a time scale short compared to the acoustic time of the finite volume.

² Heating time-scale short compared to the local acoustic time

Explicit results have been obtained for relatively modest levels of energy addition compatible with nearly-constant volume heating and linear acoustic wave propagation in the gas beyond the hot spot. The formulation includes a rational derivation of the compressible, reactive, gasdynamic equations describing the thermomechanical response of a hot spot to larger values of energy addition. This comprehensive quantitative analysis substantiates the feasibility of using thermomechanical concepts to achieve many of the objectives cited in 1a above.

2. Bibliography

- [1] Masi, E. and Bellan J., The subgrid-scale scalar variance under supercritical pressure conditions, submitted for publication February 2011,
- [2] Masi, E. and Bellan J., The subgrid scalar variance equation under supercritical pressure conditions, paper 1C04 presented at the 7th US National Combustion meeting, Atlanta, GA., March 21-23, 2011,
- [3] Kassoy, D.R., The response of a compressible gas to extremely rapid transient, spatially resolved energy addition: An asymptotic formulation, J. Eng. Math. 68(3), 249-262, (2010)
- [4] Whitham, G.B., Linear and Nonlinear Waves, Wiley Interscience, New York (1974)
- [5] Kassoy, D.R. and Wojciechowski, K., Thermomechanical response of a reactive gas to extremely rapid transient, spatially distributed energy addition: An asymptotic formulation, to be submitted for publication, May 2011, Elements of this and related work in [3] have been presented at the Division of Fluid Mechanics, American Physical Society Meeting, Nov. 2010, Long Beach, under the title, "Thermomechanical phenomena in rapidly heated inert and reactive gases."

3. Appendix

- 3.a Masi, E. and Bellan J., The subgrid-scale scalar variance under supercritical pressure conditions
- 3.b Kassoy, D.R. and Wojciechowski, K. , Thermomechanical response of a reactive gas to extremely rapid transient, spatially resolved energy addition : An asymptotic formulation

The subgrid-scale scalar variance under supercritical pressure conditions

Enrica Masi* and Josette Bellan*,**

**California Institute of Technology, Pasadena, CA 91125, USA and*

***Jet Propulsion Laboratory, California Institute of Technology,*

Pasadena, CA 91109-8099, USA, TEL: 1-818-354-6959,

FAX: 1-818-393-6682, josette.bellan@jpl.nasa.gov

(Dated: February 23, 2011)

Abstract

To model the Subgrid-Scale (SGS) scalar variance under supercritical-pressure conditions, an equation is first derived for it. This equation is considerably more complex than its equivalent for atmospheric-pressure conditions. Using a previously created Direct Numerical Simulation (DNS) database of transitional states obtained for binary-species systems in the context of temporal mixing layers, the activity of terms in this equation is evaluated and it is found that some of these new terms have magnitude comparable to that of governing terms in the classical equation. Most prominent among these new terms are those expressing the variation of diffusivity with thermodynamic variables and a Soret terms having dissipative effects. Since models are not available for these new terms that would enable solving the SGS scalar variance equation, the adopted strategy is to directly model the SGS scalar variance. Two models are investigated for this quantity, both developed in the context of compressible flows. The first one is based on an approximate deconvolution approach and the second one is a gradient-like model which relies on a dynamic procedure using the Leonard term expansion. Both models are successful in reproducing the SGS scalar variance extracted from the filtered DNS database, and moreover, when used in the framework of a Probability Density Function (PDF) approach in conjunction with the β -PDF, they excellently reproduce a filtered quantity which is a function of the scalar. For the dynamic model, the proportionality coefficient spans a small range of values through the layer cross-stream coordinate, boding well for the stability of Large Eddy Simulations using this model.

I. INTRODUCTION

One of the most useful concepts in turbulent combustion is that of a ‘flamelet’ ([1]). Its usefulness stems from the fact that the flamelet model is applicable in conjunction with finite rate chemistry and it is the only turbulent combustion model which contains the essential coupling between classically-computed molecular mass-diffusion and chemical reaction rate. This model is applicable when the chemical reactions have a relatively short characteristic time with respect to the flow, so that the flame is thin and turbulent eddies move it and distort it as an entity rather than penetrating into the flame and affecting there the reaction. When the flame is not penetrated by turbulence, the interior of the flame is akin to a laminar flame, and turbulence modeling is only needed for the flow external to the flame; this is a substantial advantage for modeling of turbulent reactive flows. Finding the evolution of the flame is then reduced to obtaining its statistical position. For non-premixed combustion, several assumptions and mathematical manipulations of the governing equations lead to an equation devoid of chemical sources for a quantity which is thus a conserved scalar. This quantity is called ‘the mixture fraction’, Z , and the statistics of the stoichiometric value of Z , Z_s , determine the flame location; whereas the temporal solution of the species mass fraction, Y , and temperature, T , in the Z coordinate system determines the internal flame structure. In the species and energy equations written in the Z coordinate system, the scalar dissipation, χ , acts as a diffusion coefficient. This scalar dissipation is that within the flamelet, and thus is at a scale smaller than the solution of the flow field; it is thus the Subgrid-Scale (SGS) scalar dissipation. Generally, it is hypothesized that Z assumes the form of a β Probability Density Function (PDF) ([2, 3]), and thus finding this distribution reduces to obtaining its mean and variance. Summarizing, in order to utilize the flamelet model one must have available the mean and variance of Z , and the SGS χ . In the context of Large Eddy Simulation (LES) in which the filtered governing equations are solved subject to models included to introduce palliatives for the filtered-out SGS effects, the mean Z value is known from the LES solution. However, neither the SGS Z variance nor the SGS dissipation of Z can be found from the LES solution, and thus they must be modeled. For example, several investigators [4, 5] modeled the SGS scalar variance as proportional to the resolved (i.e. LES) scalar dissipation, a model which follows from the classical mixing length assumption considering that the scalar variance is a measure of the level of scalar

fluctuations.

Given the aforementioned importance of the SGS scalar variance in modeling combustion, and the numerous studies devoted to solving the SGS scalar variance equation by modeling those of its terms that are not computable from the LES solution (e.g. [6, 7]), we are here investigating the modeling of the SGS scalar variance under supercritical pressure conditions and use a previously created Direct Numerical simulations (DNS) database for examining the capability of several models. The difference between this situation and the much studied atmospheric-pressure conditions is that here the species mass fluxes include Soret effects, that real gas equations of state (EOSs) instead of the perfect gas EOS are used and that the transport properties are all complex functions of the thermodynamic quantities. In Section II we derive the SGS scalar variance equation and show that it includes a large number of subgrid terms the modeling of which is uncertain. Considering this uncertainty, we next examine in Section III the conserved scalar extracted from the DNS database and explore whether it can be represented in LES by a presumed PDF for which the SGS scalar variance would be needed. Further, in Section IV, we assess the ability of two models to accurately portray the SGS scalar variance. The databases are summarized in Section V. Model assessments are here performed on these databases representing transitional states obtained from simulating mixing of two chemical species under supercritical pressure. The database consists of three sets of species and was created in the context of a temporal mixing layer. The mixing situation has been here selected rather than a chemically reacting case because the former represents a conservative choice in that the scalar could have a considerably more complex distribution in a reactive flow due to coupling among thermodynamic variables that would introduce increased flow structure, so that if a model is not accurate for the mixing situation, it will certainly be even less accurate for a reactive flow. On the other hand, an acceptable model describing the conserved scalar only during mixing may not be acceptable for reactive flows but it represents the departing point for constructing such a model. Additionally, one commonality among the evolution of the flow for all layers was the formation of High Density-Gradient Magnitude (HDGM) regions populating the entire flow, which originate from the combination of the distortion of the original boundary separating the two fluids and the mixing of species having disparate molar masses. These HDGM regions are the sites where mixing between species occurs. Thus, the conserved scalar, which is any of the two species in a layer, displays high non-uniformities and the HDGM

regions resemble in geometry the flamelets much studied in reactive flows; this resemblance adds relevance to the databases utilized in this study. Results are presented in Section VI. A summary and conclusions are offered in Section VII.

II. THE SGS SCALAR VARIANCE TRANSPORT EQUATION

Considering Z to be one of the species, the SGS scalar variance is

$$\sigma_Z = \{Z^2\} - \{Z\}^2 \quad (1)$$

where the operator $\{*\}$ denotes Favre-filtered quantities (we depart in this Section from the typical \tilde{Z} notation given the complex expressions in the SGS scalar variance equation below), i.e.

$$\{Z\} = \frac{\overline{\rho Z}}{\overline{\rho}} \quad (2)$$

where ρ is the mixture density and for any function $g(\mathbf{x})$ the filtered value is expressed in physical space by

$$\overline{g}(\mathbf{x}) = \int_{\Omega} g(\mathbf{x}') G(\mathbf{x} - \mathbf{x}') d\mathbf{x}' \quad (3)$$

where G is the filter function associated with the characteristic filter size $\overline{\Delta}$ and Ω is the entire spatial domain. According to the scalar equation under supercritical conditions [8–12],

the transport equation of the SGS scalar variance is

$$\begin{aligned}
\bar{\rho} \frac{D\sigma_Z}{Dt} = & \underbrace{\nabla \cdot [\bar{\rho} \{D\alpha_D\} \nabla \sigma_Z]}_{\text{term 1}} + \underbrace{2\bar{\rho} \{D\alpha_D\} \nabla \{Z\} \cdot \nabla \{Z\}}_{\text{term 2}} \\
& - \underbrace{2\bar{\rho} [\{D\alpha_D\} \{\nabla Z \cdot \nabla Z\}]}_{\text{term 3}} - \underbrace{\nabla \cdot (\bar{\rho}\omega)}_{\text{term 4}} + \underbrace{2 \{Z\} \nabla \cdot (\bar{\rho}\eta)}_{\text{term 5}} \\
& - \underbrace{2\bar{\rho} [\{D\alpha_D \nabla Z \cdot \nabla Z\} - \{D\alpha_D\} \{\nabla Z \cdot \nabla Z\}]}_{\text{term 6}} \\
& + \underbrace{2\nabla \cdot [\bar{\rho} \{D\alpha_D Z \nabla Z\} - \bar{\rho} \{D\alpha_D\} \{Z \nabla Z\}]}_{\text{term 7}} \\
& - \underbrace{2 \{Z\} \nabla \cdot [\bar{\rho} \{D\alpha_D \nabla Z\} - \bar{\rho} \{D\alpha_D\} \{\nabla Z\}]}_{\text{term 8}} \\
& + \underbrace{2\nabla \cdot \left[\bar{\rho} \left\{ \alpha_{BK}(1-Z)Z^2 \frac{D}{T} \nabla T \right\} \right]}_{\text{term 9}} - \underbrace{2\bar{\rho} \left\{ \alpha_{BK}(1-Z)Z \frac{D}{T} \nabla T \cdot \nabla Z \right\}}_{\text{term 10}} \\
& + \underbrace{2\nabla \cdot \left[\bar{\rho} \left\{ D \frac{(1-Z)Z^2}{R_u T} \frac{m_1 m_2}{m} \Lambda \nabla p \right\} \right]}_{\text{term 11}} \\
& - \underbrace{2\bar{\rho} \left\{ D \frac{(1-Z)Z}{R_u T} \frac{m_1 m_2}{m} \Lambda \nabla p \cdot \nabla Z \right\}}_{\text{term 12}} \\
& - \underbrace{2 \{Z\} \nabla \cdot \left[\bar{\rho} \left\{ \alpha_{BK}(1-Z)Z \frac{D}{T} \nabla T \right\} \right]}_{\text{term 13}} \\
& - \underbrace{2 \{Z\} \nabla \cdot \left[\bar{\rho} \left\{ D \frac{(1-Z)Z}{R_u T} \frac{m_1 m_2}{m} \Lambda \nabla p \right\} \right]}_{\text{term 14}}
\end{aligned} \tag{4}$$

where $\frac{D\sigma_Z}{Dt} = \frac{\partial \sigma_Z}{\partial t} + \{\mathbf{u}\} \cdot \nabla \sigma_Z$ is the material derivative, t is time, \mathbf{u} denotes the velocity, p is the pressure, T is the temperature, R_u is the universal gas constant, D and α_D are the variable diffusion coefficient and mass diffusion factor respectively, α_{BK} is the Bearman-Kirkwood form of the thermal diffusion factor and Λ is defined as

$$\Lambda = \left(\frac{1}{m_2} \frac{\partial(m/\rho)}{\partial X_2} - \frac{1}{m_1} \frac{\partial(m/\rho)}{\partial X_1} \right), \tag{5}$$

with m denoting the molar mass and X labeling the molar fraction (for both m and X , subscript 2 refers to Z and subscript 1 refers to the complement of Z in the mixture, $(1-Z)$). Vectors ω and η are the SGS fluxes

$$\omega = \{Z^2 \mathbf{u}\} - \{Z^2\} \{\mathbf{u}\}, \tag{6}$$

$$\eta = \{Z\mathbf{u}\} - \{Z\}\{\mathbf{u}\}. \quad (7)$$

Equation (4) clearly differs from the classical SGS-scalar-variance transport equation under atmospheric conditions (e.g. Jiménez *et al.* [6]). On the right hand side (r.h.s.) of Eq. (4), one recognizes familiar terms such as the molecular diffusion (term 1), the Fick-issued resolved and filtered scalar dissipation rate (terms 2 and 3, respectively), the transport of the square of the scalar and of the scalar by the SGS turbulence (terms 4 and 5, respectively); however, new terms appear as a consequence of the spatial variation of $D\alpha_D$ under supercritical conditions and also because of filtering the nonlinear pressure-gradient and Soret terms. We distinguish here between the total dissipation, which is the irreversible entropy production [13]

$$\chi \propto \mathbf{J}_\alpha \cdot \mathbf{J}_\alpha, \quad (8)$$

and which is the sum of six terms (since the species mass-diffusion flux, \mathbf{J}_α , is the sum of three terms [8, 9, 13]), and the Fick-issued dissipation which represents only one of these six terms.

Whereas the form of Eq. (4) highlights the new terms due to the supercritical-pressure aspect, another form of the SGS scalar variance equation can highlight new SGS contributions

to the SGS scalar variance; this latter form is similar to that of Pera *et al.* [7]:

$$\begin{aligned}
\bar{\rho} \frac{D\sigma_Z}{Dt} = & \underbrace{\nabla \cdot [\bar{\rho} \{D\alpha_D\} \nabla \sigma_Z]}_{\text{Resolved Molecular Diffusion}} - \underbrace{\nabla \cdot [\bar{\rho} (\omega - 2 \{Z\} \eta)]}_{\text{SGS Turbulent Fluxes}} \\
& - \underbrace{2\bar{\rho} \{D\alpha_D\} [\{\nabla Z \cdot \nabla Z\} - \nabla \{Z\} \cdot \nabla \{Z\}]}_{\text{Fick-issued SGS Dissipation}} - \underbrace{2\bar{\rho} \eta \cdot \nabla \{Z\}}_{\text{SGS Production}} \\
& + \underbrace{2\nabla \cdot [\bar{\rho} \{D\alpha_D Z \nabla Z\} - \bar{\rho} \{D\alpha_D\} \{Z \nabla Z\}]}_{\text{SGS Diffusivity 1}} \\
& - \underbrace{2\nabla \cdot [\bar{\rho} \{Z\} (\{D\alpha_D \nabla Z\} - \{D\alpha_D\} \nabla \{Z\})]}_{\text{SGS Diffusivity 2}} \\
& + \underbrace{2[\bar{\rho} \{D\alpha_D \nabla Z\} - \bar{\rho} \{D\alpha_D\} \nabla \{Z\}] \cdot \nabla \{Z\}}_{\text{SGS Diffusivity 3}} \\
& - \underbrace{2\bar{\rho} [\{D\alpha_D \nabla Z \cdot \nabla Z\} - \{D\alpha_D\} \{\nabla Z \cdot \nabla Z\}]}_{\text{SGS Diffusivity 4}} \\
& + \underbrace{2\nabla \cdot \left[\bar{\rho} \left(\left\{ \alpha_{BK} (1-Z) Z^2 \frac{D}{T} \nabla T \right\} - \left\{ \alpha_{BK} (1-Z) Z \frac{D}{T} \nabla T \right\} \{Z\} \right) \right]}_{\text{SGS Soret 1}} \\
& - \underbrace{2\bar{\rho} \left[\left\{ \alpha_{BK} (1-Z) Z \frac{D}{T} \nabla T \cdot \nabla Z \right\} - \left\{ \alpha_{BK} (1-Z) Z \frac{D}{T} \nabla T \right\} \cdot \nabla \{Z\} \right]}_{\text{SGS Soret 2}} \\
& + \underbrace{2\nabla \cdot \left[\bar{\rho} \left(\left\{ D \frac{(1-Z) Z^2}{R_u T} \frac{m_1 m_2}{m} \Lambda \nabla p \right\} - \left\{ D \frac{(1-Z) Z}{R_u T} \frac{m_1 m_2}{m} \Lambda \nabla p \right\} \{Z\} \right) \right]}_{\text{SGS Pressure 1}} \\
& - \underbrace{2\bar{\rho} \left[\left\{ D \frac{(1-Z) Z}{R_u T} \frac{m_1 m_2}{m} \Lambda \nabla p \cdot \nabla Z \right\} - \left\{ D \frac{(1-Z) Z}{R_u T} \frac{m_1 m_2}{m} \Lambda \nabla p \right\} \cdot \nabla \{Z\} \right]}_{\text{SGS Pressure 2}} \quad (9)
\end{aligned}$$

where term 5 in Eq. (4) was split into the classical turbulent-flux form and SGS production, the turbulent fluxes were combined and only SGS-type terms emphasized. The meaning of the new SGS terms is not obvious and must be investigated.

It will be shown in Section VI A that the additional SGS terms in Eq. (4) have significant activity, and thus are important to model. Moreover, the root mean square (r.m.s.) activity and the mean values of the SGS terms in Eq. (9) will be examined to understand their influence on the SGS variance evolution. Models for the new SGS terms in either Eq. (4) or Eq. (9) are not currently available, a fact which motivated investigating whether the conserved scalar conforms to a PDF having a known mathematical expression. If this is the case, the PDF could be used in a presumed-PDF approach and therefore the SGS scalar

variance could be useful for constructing the PDF, a fact which would motivate finding a model for it. The investigation of the SGS PDF shape is described next. In the remaining part of this study, we revert to the usual notation, \tilde{Z} , for the Favre filtered quantities.

III. THE PDF OF THE CONSERVED SCALAR

The scalar statistics is the important information desired for flamelet modeling (e.g. [14]). However, if the PDF is complex, it has the drawback that it can only be approximately reconstructed by a large number of its moments [15]. It is certainly computationally easier if it can be shown that the PDF of the scalar conforms to a PDF having a simple mathematical form for which only a small number of moments is necessary for its reconstruction. Such simple PDFs are, for example, the Dirac, the Gaussian and the β functions for which one needs a maximum number of two moments for reconstruction. As stated above, the first moment of the local (SGS) PDF, is always computable from LES, so that the focus is on computing the second moment, i.e. the SGS scalar variance. An extensive literature exists on the topic of the SGS scalar variance computation [2, 4, 5, 7, 16, 17] but not for supercritical turbulent flows for which, as seen in Section II, the variance equation is considerably more complex than in the already studied flows, indicating possible departures from previous findings, as implied by previous results [8]. To inquire about the form of the SGS PDF, we recall here its definition and discuss a practical way to calculate it under compressible conditions.

The instantaneous SGS PDF (f_{sgs}) of a scalar quantity Z may be defined using the fine-grained density $\gamma[\xi, Z(\mathbf{x})] \equiv \delta[Z(\mathbf{x}) - \xi]$, by weighting it with the filter function G [18, 19] as

$$f_{sgs}(\xi; \mathbf{x}) = \int_{\Omega} \delta[Z(\mathbf{x}') - \xi] G(\mathbf{x} - \mathbf{x}') d\mathbf{x}' \quad (10)$$

where δ is the Dirac delta function and ξ is the scalar-space variable representing Z . If G is a positive filter kernel, f_{sgs} has the property of a PDF. As every PDF, it is constrained by the normalization condition stating that the integral over the scalar space is unity. For $Z \in [0,1]$, the instantaneous filtered value of any quantity $g(Z(\mathbf{x}))$ may be obtained by integration over the scalar space as [17]

$$\bar{g}(\mathbf{x}) = \int_0^1 g(\xi) f_{sgs}(\xi; \mathbf{x}) d\xi. \quad (11)$$

In the same spirit, for obtaining the Favre-filtered value of every quantity $g(Z(\mathbf{x}))$ by using a PDF, a mass-weighted SGS PDF must be defined [20]

$$f_{sgs_c}(\xi; \mathbf{x}) = \frac{1}{\bar{\rho}(\mathbf{x})} \int_{\Omega} \rho(\mathbf{x}') \delta[Z(\mathbf{x}') - \xi] G(\mathbf{x} - \mathbf{x}') d\mathbf{x}' \quad (12)$$

where the subscript c denotes the compressible situation, and then

$$\tilde{g}(\mathbf{x}) = \int_0^1 g(\xi) f_{sgs_c}(\xi; \mathbf{x}) d\xi. \quad (13)$$

The mass-weighted SGS PDF (referred to as Filtered Mass Density Function (FMDf)) is defined by Jaber *et al.* [21] and Raman *et al.* [22] in a probabilistic manner using the property that the integral of f_{sgs_c} over the sample space gives the filtered density value. This definition is then used in the framework of a PDF approach where a transport equation for the PDF is solved. Here, instead, a PDF normalized by $\bar{\rho}(\mathbf{x})$, i.e. Eq. (12), is needed as we wish to satisfy the classical definition of the PDF integrating to unity. The SGS PDF, as defined by Eqs. (10) and (12), is not a statistical quantity as it is a one-point distribution conditioned to a given flow realization. Following Jiménez *et al.* [3], Fox [23] and Pitsch [24], an appropriate SGS PDF utilizable for modeling purposes should instead be understood as a statistical quantity arising from a statistical sample of equivalent grid elements. Since in the *a priori* analysis using the DNS database the exact statistical quantity is not available, we will instead use, as an approximation of the statistical SGS PDF for evaluating the accuracy of models, statistics computed employing the one-point SGS PDF defined above. The expectation of this PDF over homogeneous directions and the conditional (on moments) expectation are used to assess presumed PDF shapes against the DNS-extracted ones, as described below.

Assuming the filter width to be smaller than the variation scale of mean quantities and that filtering and averaging operators commute, a Favre mean (i.e. expectation) of the filtered local value may be obtained

$$\langle \tilde{g}(\mathbf{x}) \rangle_c = \int_0^1 g(\xi) \langle f_{sgs_c}(\xi; \mathbf{x}) \rangle_c d\xi \quad (14)$$

where the operator $\langle \cdot \rangle_c$ denotes planar averages weighted by the filtered density. The quantity $\langle f_{sgs_c} \rangle_c$ is equivalent to a filtered PDF of the scalar as defined by Jiménez *et al.* [3] for incompressible flows and it is given by the mass-weighted PDF of the scalar over planes of height equal to the filter width (coarsened-grid planes). The filtered PDF may be

computed as

$$\langle f_{sgs_c}(\xi; \tilde{\xi}, \sigma_\xi) \rangle_c = \int f_c(\tilde{\xi}, \sigma_\xi) f_{sgs_c}(\xi; \tilde{\xi}, \sigma_\xi) d\tilde{\xi} d\sigma_\xi \quad (15)$$

by using the mass-weighted joint-moment PDF f_c in conjunction with the PDF f_{sgs_c} , defined as a function of couples of moments $(\tilde{\xi}, \sigma_\xi)$ instead than \mathbf{x} where σ_ξ is the moment-space variable representing σ_Z , and integrating over the LES-moment space $(\tilde{\xi}, \sigma_\xi)$. The definition of Eq. (15) may be computationally practical since any assumed PDF model may be evaluated by replacing in Eq. (15) the presumed PDF, $f_{sgs_c}(\xi; \tilde{\xi}, \sigma_\xi)$, computed from any couple of mapped values $(\tilde{\xi}, \sigma_\xi)$, and $f_c(\tilde{\xi}, \sigma_\xi)$ as obtained from the filtered DNS database over homogeneous (coarsened-grid) directions. The f_{sgs_c} expectation, $\langle f_{sgs_c} \rangle_c$, is used to evaluate the presumed-PDF shapes against the DNS-extracted ones.

To approximate the statistical SGS PDF, we also consider as an alternate to the above method, the optimal estimator method of Moreau *et al.* [25] which uses the conditional expectation. The latter is obtained by averaging the PDF $f_{sgs_c}(\xi; \tilde{\xi}, \sigma_\xi)$, over a sample of PDFs having the same couples of exact moments $(\tilde{\xi}, \sigma_\xi)$. Practically, the computation is performed by averaging over SGS volumes having couple of moments $(\tilde{\xi}, \sigma_\xi)$ very close to a selected one, according with a fixed standard deviation chosen such as to have accurate statistics. The conditional expectation of the DNS-extracted quantity $f_{sgs_c}(\xi; \tilde{\xi}, \sigma_\xi)$ is then compared to the assumed PDFs computed using the exact moments. Here, the Favre-conditional expectation is obtained by mass-weighted averaging using the filtered local density, and statistics are computed over a slab of the mixing layer in order to increase the sample size.

In this study, three local PDFs will be assessed: the β PDF, the Gaussian and the Dirac ones. These PDFs are here briefly recalled:

- The β PDF:

$$f_{sgs_c}(\xi; \alpha(\tilde{\xi}, \sigma_\xi), \beta(\tilde{\xi}, \sigma_\xi)) = \frac{\Gamma(\alpha + \beta)}{\Gamma(\alpha)\Gamma(\beta)} \xi^{\alpha-1} (1 - \xi)^{\beta-1} \quad (16)$$

where Γ is the Gamma function and parameters α and β are defined by

$$\alpha = \tilde{\xi} \left(\frac{\tilde{\xi}(1 - \tilde{\xi})}{\sigma_\xi} - 1 \right), \quad \beta = (1 - \tilde{\xi}) \left(\frac{\tilde{\xi}(1 - \tilde{\xi})}{\sigma_\xi} - 1 \right). \quad (17)$$

- The Gaussian PDF:

$$f_{sgs_c}(\xi; \tilde{\xi}, \sigma_\xi) = \frac{\frac{1}{\sqrt{2\pi\sigma_\xi}} e^{-\frac{(\xi - \tilde{\xi})^2}{2\sigma_\xi}}}{\frac{1}{2} \left(1 + \operatorname{erf} \frac{b - \tilde{\xi}}{\sqrt{2\sigma_\xi}} \right) - \frac{1}{2} \left(1 + \operatorname{erf} \frac{a - \tilde{\xi}}{\sqrt{2\sigma_\xi}} \right)}, \quad (18)$$

As the scalar ξ is bounded between 0 and 1, the Gaussian distribution is truncated and the resulting PDF is thus re-normalized using the difference between the cumulative distribution functions evaluated at $b = 1$ and $a = 0$. This computed distribution has no longer the same mean and variance as the original distribution. As an alternate, a clipped Gaussian is also considered [26].

- The Dirac PDF:

$$f_{sgsc}(\xi; \tilde{\xi}) = \delta(\xi - \tilde{\xi}). \quad (19)$$

The Dirac PDF is utilized when the scalar ξ is only modeled through its mean, $\tilde{\xi}$.

In Section VI B we present results from computations with these PDFs using both methods to approximate the statistical SGS PDF, and particularly we show that whereas the Dirac and Gaussian PDF are generally deficient, the β -PDF typically yields a good approximation, a fact which provided the incentive to directly model the scalar variance, as described in the following.

IV. DIRECT MODELING OF THE SGS SCALAR VARIANCE

Two types of models appear to be promising candidates for modeling small-scale effects removed through filtering. The first model is of a structural type [27] based on the Approximate Deconvolution Model (ADM) [28] while the second one is of a functional type using a gradient-based scaling law [4]. The two models are conceptually different as the first one arises from a mathematical derivation with no assumption regarding the nature of scale interactions, while the second one uses a mixing-length hypothesis in conjunction with an equilibrium assumption. The original contribution of our work is the investigation of the ADM capability for computing σ_Z in variable density flows, and the extension of a recent dynamic gradient-based formulation [5] to compressible conditions for modeling σ_Z .

A. The approximate deconvolution model

The deconvolution procedure [28] relies on the assumption that there exists an inverse operator $G^{-1} = \sum_{l=0}^{\infty} (I - G)^l$ such as

$$Z^* = \left[\sum_{l=0}^N (I - G)^l \right] * \bar{Z} \quad (20)$$

where I is the identity operator and Z^* represents an approximation of the original field Z , on the LES mesh grid, at the series truncation order N . The series is known to converge for $\|I - G\| < 1$, and written using de van Cittert method [29] based on the Neumann series leads to

$$Z^* = \bar{Z} + \left(\bar{Z} - \bar{\bar{Z}} \right) + \left(\bar{Z} - 2\bar{\bar{Z}} + \bar{\bar{\bar{Z}}} \right) + \dots \quad (21)$$

where the accuracy of Z^* depends on N . In practice, due to the numerical discretization (projection on a coarse mesh grid), only the recoverable part of the original field Z may be obtained by a deconvolution procedure [30]. Furthermore, the deconvolution relies on the form of the convolution-filter kernel and on the shape of the spectrum of the field [17].

The series' rate of convergence is situation dependent. For example, it has been found [31] that $N = 3$ is sufficient to bring an improvement in that for a quantity ϕ , $(\phi^* - \bar{\phi})$ is not null showing that the expansion is indeed effective, and for $N \geq 5$ the value of $(\phi^* - \bar{\phi})$ did not change appreciably from that obtained with $N < 5$. In other studies specifically directed at Z , it was found that the series converges very slowly. Pantano and Sarkar [16] tested the deconvolution procedure in an *a priori* analysis using the DNS of a temporal mixing layer; they showed that even with $N = 5$ (i.e. fourth-order approximation) and a small filter size ($\bar{\Delta}/\Delta x_{DNS} = 4$, where Δx_{DNS} is the grid spacing for a simulation where all scales relevant to most of the dissipation are resolved, as in DNS), no more than 88% of the total SGS-scalar-variance amount (in the peak zone) was recovered. The rate of convergence of the series and the recoverable amount of the field are thus the main issues of the method. In order to recover all effects of the smallest scales, Stolz *et al.* [28] suggested a secondary filtering through the use of a relaxation parameter in the Navier-Stokes (NS) equations. To mitigate both these issues, Pantano and Sarkar [16] and Mellado *et al.* [17] proposed an approximate reconstruction using moments (ARM) method which, based on the definition of an intermediate field, leads to computing the SGS scalar variance by imposing equality between the real moment and that of the intermediate field. This procedure results in an

expression for a parameter c_0 , characterizing the model, that is obtained by finding the real and positive solution of a second-order polynomial equation. The polynomial coefficients a_0, a_1, a_2 are computed using the presumed shape of the spectrum of the scalar quantity. Once the shape of the spectrum is selected, c_0 may be precomputed and stored in a two-dimensional table of coordinates represented by two dimensionless quantities: the Péclet number, and the ratio between the filter width and a large scale of the scalar fluctuations. That approach was developed for incompressible flows. Under compressible conditions, that model requires rewriting for the conservative quantities for which the governing equations are solved in LES of compressible flows; but then, equality between moments would not lead to an explicit expression for the SGS scalar variance unless additional assumptions are invoked. Moreover, when in presence of variable density, the shape of the spectrum cannot be built using calibrated constants computed either by using the Reynolds-averaged scalar variance or by employing the Favre-averaged one. This is why, considering the practical utilization in LES, we opt to explore a classical deconvolution procedure.

Since in LES it is the conservative rather than primitive quantities which are calculated, we are legitimately inquiring as to whether the SGS scalar variance could be accurately reconstructed employing a deconvolution procedure for these quantities. Indeed, for reconstructing the approximated scalar field and building the SGS (Favre) scalar variance, we must reconstruct ρ and Z through

$$\rho^* = \bar{\rho} + (\bar{\rho} - \bar{\bar{\rho}}) + (\bar{\rho} - 2\bar{\bar{\rho}} + \bar{\bar{\bar{\rho}}}) + \dots \quad (22)$$

$$(\rho Z)^* = \overline{\rho Z} + (\overline{\rho Z} - \overline{\bar{\rho Z}}) + (\overline{\rho Z} - 2\overline{\bar{\rho Z}} + \overline{\bar{\bar{\rho Z}}}) + \dots \quad (23)$$

which then permits writing

$$Z^{**} = (\rho Z)^* / \rho^*. \quad (24)$$

invoking the assumption

$$Z^{**} \simeq Z^*. \quad (25)$$

Equation (25) implies equality between second-order moments of Z^{**} and Z^* . The non-linear function of the approximate field, the Favre SGS scalar variance, is then built, for consistency [16], by using of deconvoluted fields as

$$\sigma_Z = \frac{\overline{\rho^* Z^{**} Z^{**}}}{\bar{\rho}^*} - \frac{\overline{\rho^* Z^{**}}}{\bar{\rho}^*} \frac{\overline{\rho^* Z^{**}}}{\bar{\rho}^*}. \quad (26)$$

The assumption of Eq. (25) is exact if both ρ and ρZ fields are totally recovered and an infinite expansion is used. Otherwise, there is no proof that ratio between series (23) and (22) converges to the recoverable part of the quantity Z , which is Z^* at a given truncation order N . Such an assumption, although not trivial, has already been used by Stolz *et al.* [32] while reconstructing flux terms of the compressible NS equations, and by Dubois *et al.* [33] in the first of a two-step procedure for estimating the SGS stress tensor. The difference between the previous studies and our investigation is that ADM is here used in the context of a soft-deconvolution problem ([27]) in which no additional models for recovering the deficient SGS part are provided. In Section VI C 1 we evaluate the assumption of Eq. (25) and the equality between moments of Z^{**} and Z^* for several truncation orders. We also assess the ADM model using the series Eqs. (22) and (23), with, consistently, both series truncated at same order.

B. The dynamic model

A Smagorinsky-type model for predicting the SGS scalar variance of compressible flows was proposed by Pierce and Moin [4] using a dynamic procedure [34]. This model was similar to that of Moin *et al.* [35] for modeling the SGS stress tensor and heat flux under compressible conditions. The model of Pierce and Moin [4] has been extensively used over the years [7, 20, 36, 37] as an alternate to the scale-similarity model suggested by Cook and Riley [2] based on the idea of Bardina *et al.* [38]. The scale-similarity model has been explored in several different configurations [3, 7, 39, 40]. Recently, Balarac *et al.* [5], using the optimal estimator concept of Moreau *et al.* [25], showed that the irreducible error associated with a Smagorinsky-type model is relatively small if compared to that evaluated for a scale-similarity model, meaning that the functional form of a gradient-based model has significant potential in LES for reproducing the SGS scalar variance. This has also been observed by Wall *et al.* [36] when studying the performance of the two models used in that study in conjunction with a presumed PDF approach. On the other hand, Balarac *et al.* [5] showed that the quadratic error associated with the gradient-based model notably increases with filter width when a classical dynamic procedure is used for computing the model coefficient. In the present study, the Balarac *et al.* [5] model, which is for incompressible flow, is reformulated under compressible conditions and evaluated for compressible supercritical

turbulent mixing layers in Section VI C 2.

For completeness, the Pierce and Moin [4] dynamic model is briefly recalled and for consistency we use their notation, where $\widehat{(\cdot)}$ is the unweighted test filter at test-filter level \widehat{G} corresponding to the filter width $\widehat{\Delta}$ and

$$\breve{\breve{Z}} = \widehat{\widetilde{\rho Z}} / \widehat{\rho}. \quad (27)$$

In the classical dynamic model [4], first the variance is related to the gradient of the resolved scalar field as

$$\overline{\rho \sigma_Z} = \overline{\rho}(\widetilde{Z Z} - \widetilde{Z} \widetilde{Z}) = C_d \overline{\Delta}^2 \overline{\rho} \left| \nabla \widetilde{Z} \right|^2 \quad (28)$$

which, when filtered, yields the following expression

$$\widehat{\overline{\rho Z Z}} - \widehat{\overline{\rho} \widetilde{Z} \widetilde{Z}} = C'_d \overline{\Delta}^2 \left(\widehat{\overline{\rho} \left| \nabla \widetilde{Z} \right|^2} \right). \quad (29)$$

A similar model is then proposed at the filter level corresponding to the double convolution of \overline{G} and \widehat{G} , i.e. $\widehat{\widehat{G}} = \overline{G} * \widehat{G}$, associated to the filter width $\widehat{\Delta}$:

$$\widehat{\overline{\rho Z Z}} - \widehat{\overline{\rho} \breve{\breve{Z}} \breve{\breve{Z}}} = C''_d \widehat{\Delta}^2 \widehat{\rho} \left| \nabla \breve{\breve{Z}} \right|^2. \quad (30)$$

Finally, subtracting Eq. (29) from Eq. (30) and assuming $C'_d = C''_d = C_d$ (implying either that the flow variation is such that filtering with the grid or test filter produces analogous fields or that the coefficients have a slow variation) yields

$$\widehat{\overline{\rho} \widetilde{Z} \widetilde{Z}} - \widehat{\overline{\rho} \breve{\breve{Z}} \breve{\breve{Z}}} = C_d \left[\widehat{\Delta}^2 \widehat{\rho} \left| \nabla \breve{\breve{Z}} \right|^2 - \overline{\Delta}^2 \left(\widehat{\overline{\rho} \left| \nabla \widetilde{Z} \right|^2} \right) \right] \quad (31)$$

which may be generically written as

$$\mathcal{L} = C_d \mathcal{M} \quad (32)$$

where $\mathcal{L} \equiv \left(\widehat{\overline{\rho} \widetilde{Z} \widetilde{Z}} - \widehat{\overline{\rho} \breve{\breve{Z}} \breve{\breve{Z}}} \right)$ is the generalized Leonard term and \mathcal{M} is defined as

$$\mathcal{M} = \widehat{\Delta}^2 \widehat{\rho} \left| \nabla \breve{\breve{Z}} \right|^2 - \overline{\Delta}^2 \left(\widehat{\overline{\rho} \left| \nabla \widetilde{Z} \right|^2} \right). \quad (33)$$

Since both \mathcal{L} and \mathcal{M} are computable from the LES solution, C_d may be dynamically computed over homogeneous directions either as the ratio between averaged \mathcal{L} and \mathcal{M} , or through the least-square averaging (Lilly [41]) which optimizes the local value by minimizing the

quadratic error. This dynamic procedure uses a compressible version of the Germano identity [42], originally written for the SGS stress tensor [35, 43]

$$L_{ij} = \widehat{\bar{\rho}} T_{ij} - \widehat{\bar{\rho} \tau_{ij}}, \quad (34)$$

which adapted to the scalar variance may be written as

$$L = \widehat{\bar{\rho}} \Sigma_Z - \widehat{\bar{\rho} \sigma_Z} \quad (35)$$

where

$$\widehat{\bar{\rho}} \Sigma_Z \equiv \left(\widehat{\bar{\rho} Z Z} - \widehat{\bar{\rho}} \widetilde{Z} \widetilde{Z} \right). \quad (36)$$

Equation (30) was questioned by Balarac *et al.* [5] who emphasized that a generic filtered quantity \widehat{f} is not directly obtained through a single convolution, but rather from two sequential filterings. Using the Bedford and Yeo [44] expansion (which provides a power series for the non-linear filtered generic term \overline{fg} as a function of the resolved quantities \bar{f} and \bar{g}), applied twice to the filtered quantities, Balarac *et al.* [5] pointed out a missing leading-order term in Eq. (30) and provided an alternative model for \mathcal{M} that involves the use of the Leonard term expansion. The same reasoning is possible for compressible flows using an appropriate Taylor expansion. Such an approximate expansion was suggested by Vreman [43] for modeling the SGS stress tensor and is adapted here for isotropic filter to the scalar variance as

$$\begin{aligned} \bar{\rho} \sigma_Z &= \overline{\rho Z Z} - \overline{\rho Z} \overline{\rho Z} / \bar{\rho} \\ &= \rho Z Z + \frac{\bar{\Delta}^2}{24} \nabla^2 (\rho Z Z) - (\rho Z + \frac{\bar{\Delta}^2}{24} \nabla^2 (\rho Z)) (\rho Z + \frac{\bar{\Delta}^2}{24} \nabla^2 (\rho Z)) / (\rho + \frac{\bar{\Delta}^2}{24} \nabla^2 \rho) + O(\bar{\Delta}^4) \\ &= \frac{\bar{\Delta}^2}{12} \rho |\nabla Z|^2 + O(\bar{\Delta}^4) \end{aligned} \quad (37)$$

where the approximation

$$\left(\rho + \frac{\bar{\Delta}^2}{24} \nabla^2 \rho \right)^{-1} = \frac{1}{\rho} - \frac{\bar{\Delta}^2}{24 \rho^2} \nabla^2 \rho + O(\bar{\Delta}^4) \quad (38)$$

has been made to obtain the final result. A similar expansion

$$\rho = \bar{\rho} + O(\bar{\Delta}^2), \quad Z = \widetilde{Z} + O(\bar{\Delta}^2) \quad (39)$$

used in Eq. (37) leads to

$$\widetilde{\bar{\rho} Z Z} = \bar{\rho} \widetilde{Z} \widetilde{Z} + \frac{\bar{\Delta}^2}{12} \bar{\rho} |\nabla \widetilde{Z}|^2 + O(\bar{\Delta}^4). \quad (40)$$

Equation (40) is conceptually similar to that used by Balarac *et al.* [5] for incompressible conditions and in the same way it may be used for obtaining $\widehat{\bar{\rho}}\Sigma_Z$, i.e. the left hand side (l.h.s.) term of Eq. (30). First, the test filter \widehat{G} , is applied to Eq. (40)

$$\widehat{\widehat{\bar{\rho}ZZ}} = \widehat{\bar{\rho}\widetilde{Z}\widetilde{Z}} + \frac{\overline{\Delta}^2}{12} \left(\widehat{\bar{\rho}|\nabla\widetilde{Z}|^2} \right) + O(\overline{\Delta}^4), \quad (41)$$

then the first term on the r.h.s. is expanded at the filter level \widehat{G} based on $\bar{\rho}$ and \widetilde{Z} using the approximate expansion of Eqs. (37)-(39) applied to these variables, leading to:

$$\widehat{\widehat{\bar{\rho}ZZ}} = \widehat{\bar{\rho}}\check{\check{Z}}\check{\check{Z}} + \frac{\widehat{\Delta}^2}{12} \widehat{\bar{\rho}}|\nabla\check{\check{Z}}|^2 + \frac{\overline{\Delta}^2}{12} \left(\widehat{\bar{\rho}|\nabla\widetilde{Z}|^2} \right) + O(\widehat{\Delta}^4, \overline{\Delta}^4). \quad (42)$$

The above equation, reformulated using a constant to account for the truncation error, leads to

$$\widehat{\widehat{\bar{\rho}ZZ}} - \widehat{\bar{\rho}}\check{\check{Z}}\check{\check{Z}} = C_d''' \left[\widehat{\Delta}^2 \widehat{\bar{\rho}}|\nabla\check{\check{Z}}|^2 + \overline{\Delta}^2 \left(\widehat{\bar{\rho}|\nabla\widetilde{Z}|^2} \right) \right] \quad (43)$$

which represents another form for the l.h.s. term in Eq. (30). Subtracting Eq. (29) from Eq. (43) and assuming $C_d' = C_d''' = C_d$ (under the same implications as when adopting $C_d' = C_d'' = C_d$) leads to a new formulation of \mathcal{M} , \mathcal{M}_n

$$\mathcal{M}_n = \widehat{\Delta}^2 \widehat{\bar{\rho}}|\nabla\check{\check{Z}}|^2 \quad (44)$$

representing the leading order of the Leonard term expansion when C_d palliates for the truncated terms in the Taylor series expansion. Balarac *et al.* [5] pointed out that Eq. (42) contains a new leading order term with respect to Eq. (30) which, when taken into account, yields the new formulation of \mathcal{M} , \mathcal{M}_n . Although we obtain the same result as Balarac *et al.* [5], \mathcal{M}_n for compressible conditions, Eq. (30) is different from the corresponding equation of Balarac *et al.* [5] as far as filter width used. Balarac *et al.* [5] did not discuss the disparity between the filter width used in the classical formulation and the filter width needed in the Leonard term expansion, and it appears that the same filter width was used. However, when the correct filter width is used, the issue of the new leading order term in the formulation of Eq. (30) is moot, and the result is that only an alternative formulation for $\widehat{\bar{\rho}}\Sigma_Z$ is derived. According to Eq. (44), it is clear that the new formulation uses $\widehat{\Delta}$. For the classical formulation, according to Eq. (33), the filter is though $\widehat{\Delta}$. This finding is in agreement with the study of Brun and Friedrich [45]. Using the Vreman *et al.* [46] estimate, the filter width associated with the filter level \widehat{G} is

$$\widehat{\Delta}^2 = \widehat{\Delta}^2 + \overline{\Delta}^2, \quad (45)$$

representing an approximation for double top-hat filtering. In order to explore the impact of the filter width used in the classical formulation, and thus to assess the correctness of the results, we present in Section VI C 2 an *a priori* analysis using the classical formulation in conjunction with each of the approximations for the filter width $\widehat{\Delta}$ at the filter level \widehat{G} : i) $\widehat{\Delta}^2 = \widehat{\Delta}^2 + \overline{\Delta}^2$ (correct approximation) and ii) $\widehat{\Delta} = \widehat{\Delta}$ (incorrect with a top-hat filter), and compare the results from these two computations with those from the new formulation based on the Leonard term expansion for which the filter is demonstrated to be $\widehat{\Delta}$.

We can thus evaluate the gradient-based model for σ_Z using two different formulations. The first formulation is the classical one employing

$$C_d = \frac{\langle \mathcal{LM} \rangle}{\langle \mathcal{MM} \rangle} \quad (46)$$

where $\langle \rangle$ denote averages over homogeneous planes. The second formulation, which we call the “new model”, is the present one, and uses

$$C_d = \frac{\langle \mathcal{LM}_n \rangle}{\langle \mathcal{M}_n \mathcal{M}_n \rangle}. \quad (47)$$

Since the evaluation of the correct filter width at filter-level \widehat{G} represents the main issue for computing C_d using a dynamic procedure, the model based on the Leonard term expansion represents a solution to this quandary, as shown in Section VI C 2.

V. DESCRIPTION OF THE DNS DATABASE

A complete and detailed description of the DNS database has already been provided in [8–12]. Out of the complete database consisting of three sets of species heptane/nitrogen (HN), oxygen/hydrogen (OH) and oxygen/helium (OHe) for which several simulations were conducted, we select here three simulations, HN600, OH750 and OHe600 for examination so as to enhance the generality of the results. The DNS were conducted for a temporal mixing layer and initiated with (vorticity-thickness based) Reynolds number of 600 (HN600, OHe600) and 750 (OH750) where $\delta_{\omega,0} = \Delta U_0 / \langle \partial u_1 / \partial x_2 \rangle$ is the initial vorticity thickness, $\langle \rangle$ is here performed over (x_1, x_3) planes and ΔU_0 is the initial velocity difference across the layer. In all cases, the DNS grid, Δx_{DNS} , was fine enough to resolve the scales overwhelmingly responsible for the dissipation. Transitional states were achieved for all of these layers at $t_{tr}^* = 135$ for HN600, $t_{tr}^* = 150$ for OH750, $t_{tr}^* = 220$ for OHe600, where $t^* \equiv t \Delta U_0 / \delta_{\omega,0}$;

the corresponding transitional Reynolds numbers were 1452, 1507 and 2004. Selle *et al.* [9] showed that this database is relevant for fully-turbulent flow modeling.

VI. RESULTS

In all computations, the results of which are presented below, we use a top-hat filter and a trapezoidal integration method.

A. Activity of terms in the scalar variance equation

All terms in Eqs. (4) and (9) were *a priori* evaluated using the three DNS realizations discussed above. The goal of this evaluation is: i) to assess the magnitude of the filtered terms with respect to that of the resolved terms for modeling purposes (Eq. 4) and ii) to assess the magnitude of the SGS terms with respect to that of the resolved terms in order to identify which SGS quantities are important to model (Eq. 9). A cubic top-hat filter and several filter widths, $\overline{\Delta}$, were used in the evaluation but only the analysis corresponding to the ratio $\overline{\Delta}/\Delta x_{DNS} = 8$ is here presented, being representative of all ratio values.

Depicted in the Figure (1) is the activity of terms in Eq. (4) as measured by the r.m.s. magnitude of each term. The results indicate that terms 4 and 5, which involve the classical subgrid fluxes, dominate showing that our transitional databases have indeed the turbulent characteristics that make them relevant to this study. The importance of the advective term increases with the strength of the HDGM at transition [11] (compare OH750 with HN600) and with increasing Reynolds number value at transition [9] (compare HN600 and OHe600). The diffusion term (term 1) is of same order of magnitude as the advection term only for OH750 because the hydrogen diffusivity is very large. Terms 2 and 3 are somewhat smaller than the advection term for HN600 and OHe600, but significantly larger for OH750. For both HN600 and OHe600, and less so for OH750, term 3 is larger than term 2, which is a manifestation of the SGS magnitude associated with the Fick-issued dissipation. Term 6, representing SGS effects, could be neglected in all cases. Evaluation of term 7, expressing the diffusivity spatial variation, shows that it is of the same order of magnitude as the resolved diffusion (term 1) for HN600 and OHe600 simulations, and even larger for the OH750. Thus, term 7 is non negligible in Eq. (4) under all circumstances. Similarly, term 8 representing

the effect of spatially varying diffusivity is comparable to term 1 for all cases and should be included when modeling Eq. (4), particularly when diffusion plays an important role during mixing (i.e. OH750). In contrast, the terms arising from filtering of the Soret contribution, i.e. terms 9, 10 and 13 are only substantial for the HN600 case, while those stemming from filtering of the term proportional to the pressure gradient, namely terms 11 and 14, only play a minor role in the OH750 and OHe600 layers and are unimportant for the HN600 case. Term 12 is found negligible everywhere.

Figure (2) shows the results from the *a priori* assessment of the terms in Eq. (9). Both the planar average and the r.m.s. activity are computed in order to evaluate not only the importance but also the nature (i.e. diffusive, dissipative, etc.) of each term. Considering the planar averages, in all cases, the magnitude of the diffusion terms is comparable to that of the advection term, and the production term is comparable in magnitude to the Fick-issued SGS dissipation term. Due to the difficulty of entraining the lower-stream heavy fluid, the mixing layer growth is moderate which explains the small value of the advection term compared to that of the SGS production and SGS Fick-issued dissipation. Additionally, for the HN600 layer the term denoted by SGS Soret 2 has considerable negative magnitude, adding to the Fick-issued dissipation. This observation is consistent with the definition of the total scalar dissipation [13]

$$\chi_T = \frac{1}{\rho D \alpha_D} \mathbf{J}_\alpha \cdot \mathbf{J}_\alpha \quad (48)$$

that is here contrasted to the Fick-issued dissipation

$$\chi_F = \rho D \alpha_D \nabla Z \cdot \nabla Z, \quad (49)$$

which is only one of the six terms of Eq. (48). Obviously, the Soret contribution plays an important role for the HN600 layer in the destruction of the scalar fluctuations at the smallest scales, but clearly its importance is binary-species dependent as it has no impact on the mixing of the oxygen with hydrogen or helium. In order to understand the behavior of χ_F with respect to χ_T , we illustrate in Fig. (3) the average of χ_T conditioned on χ_F in two planes of the HN600 mixing layer ($x_2/\delta_{\omega,0} = 0.44$ which is in the central part of the layer and $x_2/\delta_{\omega,0} = 5.11$ which is away from the center but still in a significant mixing region). The results indicate that χ_T is larger than χ_F , particularly at the periphery of the layer. Noteworthy, the linear dependency between χ_T and χ_F in Fig. (3) justifies the use of the scaling law based on the \tilde{Z} gradient for modeling the SGS scalar variance (see Section

VIC2) since the behavior of χ_T and χ_F is similar.

Considering the r.m.s. activity, in concert with the findings from analysis of Eq. (4), the effect of the $D\alpha_D$ variation at small scales cannot be underestimated. For HN600 and OHe600 the SGS turbulent fluxes are larger in magnitude than the molecular diffusion flux, meaning that the scalar fluctuations contribute to the mixing at the SGS scales. Among the four SGS diffusivity terms, the second one assumes large values when compared to the other diffusion-like terms or advection term, indicating that it must be retained and modeled in the SGS scalar variance equation; the third and fourth SGS diffusivity terms have smaller magnitudes and their nature is dissipative; finally, the first one compares in magnitude to the resolved diffusion in HN600 and OHe600 but is much larger than the resolved diffusion for OH750. The conclusion is that particular attention should be devoted to SGS Diffusivity 1 and SGS Diffusivity 2 terms because they have a dominant contribution to the mixing of oxygen with hydrogen at the SGS scales. The Soret contribution, labeled SGS Soret 1, has a diffusion-like behavior and is non negligible only in the HN600 mixing layer. Also, the SGS contributions stemming from filtering of the pressure-gradient terms are negligible in all cases.

B. Assessment of the presumed-PDF approach for computing filtered non-linear scalar-dependent quantities

An *a priori* evaluation of the statistical SGS PDF for the HN600 layer is illustrated in Fig. (4) for the same two (x_1, x_3) homogeneous planes of coordinates $x_2/\delta_{\omega,0} = 0.44$ and $x_2/\delta_{\omega,0} = 5.11$ as in Fig. (3). The DNS-extracted filtered PDF $\langle f_{sgs_c} \rangle_c$ is evaluated by mass-weighted averaging the Z PDF over coarsened-grid planes. The presumed averaged SGS PDFs are computed employing mapped LES moments $(\tilde{\xi}, \sigma_{\xi})$ and using Eq. (15). As expected, the figure displays the best prediction when a β PDF is used. The difference between one-moment and two-moment distributions is evident both in the central part of the mixing layer ($x_2/\delta_{\omega,0} = 0.44$) and away from it ($x_2/\delta_{\omega,0} = 5.11$). The difference between the two-moment distributions, Gaussian and β , is also clear, particularly in zones of poor mixing where a Gaussian distribution is not appropriate.

Figure (5) portrays the corresponding OH750 results over the same x_2 planes as for the HN600 layer. In the OH750 case, no large difference between PDF models are visible which

is conjectured to result from the high hydrogen diffusivity which promotes good mixing. Finally, OHe600 layer results are shown in Figure (6). For OHe mixing, the two-moment PDFs increase the model accuracy compared to the single-moment one, and a β PDF gives slightly better results than the Gaussian PDF, as expected.

Results from the optimal estimators are displayed in Fig. (7). Because this methodology is based on conditioning over a couple of moments, the Dirac presumed PDF is not considered. In order to increase the sample size, the conditional expectations are computed over a slab of the mixing layer of coordinates $x_2/\delta_{\omega,0} = \pm 5.3$. As expected, in regions of well-mixed species, the β PDF and the Gaussian PDF give similar predictions while the β PDF is more appropriate for unmixed situations.

Thus, we have shown that two methodologies are in agreement regarding the appropriateness of the presumed β PDF shape. However, it is known that for atmospheric conditions [17] good agreement with a template for averaged distributions (as given by both methodologies) does not necessarily imply similar pointwise agreement, so it is important to test the capabilities of the three distributions of Eqs. (16), (18) and (19) to provide local agreement (as needed in reactive flows) in computations where they would be used to reproduce filtered non-linear terms (e.g. reaction rates). For this purpose, we select a simple non-linear Z -function

$$F(\xi) = \exp \left\{ -2 \left[\operatorname{erf}^{-1} (2\xi - 1) \right]^2 \right\}, \quad (50)$$

representing the χ functional form in a one-dimensional unsteady laminar subcritical mixing layer [47]. Then, the filtered value of $F(\xi)$ may be estimated by integration over the scalar space using Eq. (13) as

$$\widetilde{F(\mathbf{x})} = \int_0^1 F(\xi) f_{sgs_c}(\xi; \mathbf{x}) d\xi. \quad (51)$$

Figure (8) illustrates scatter plots of the modeled quantity $\widetilde{F(Z)}^{mod}$ (superscript *mod* labels a modeled quantity) versus the exact quantity $\widetilde{F(Z)}$ extracted from the filtered DNS database HN600, over two planes, in the central part and at the periphery of the layer. The modeled functions are computed by replacing $f_{sgs_c}(\xi; \mathbf{x})$ in Eq. (51) with the presumed SGS PDF (Dirac, Gaussian or β) constructed from the exact moments extracted from the filtered DNS database at t_{tr}^* . The local results are in accord with the assessment of the statistical SGS PDFs presented in Figs. (4) and (7). A drastic improvement in predictions is obtained by using the β -PDF in the mixing of heptane and nitrogen. An improvement is also obtained

for the oxygen/helium system (not shown) while in the oxygen/hydrogen mixing layer the differences are minor (not shown).

As mentioned in Section III, a clipped Gaussian was also considered. For the filtered PDF, results using the clipped Gaussian exhibited small differences from those obtained with the truncated Gaussian for the HN600 mixing layer (not shown), and imperceptible differences for the OH750 and OHe600 mixing layers (not shown). The clipped Gaussian also provided slightly more accurate results when used to model the non-linear Z -function (not shown).

Whereas the Z -function of Eq. (50) is here used only to test the ability of the models to reproduce nonlinearities, the function is not necessarily expected to represent the real χ for three-dimensional supercritical flows. This topic is addressed in Appendix A.

C. Evaluation of direct models for the SGS scalar variance

Having shown in Section VIA that under supercritical p conditions modeling of new terms in the σ_Z equation is necessary (but uncertain), and shown in Section VIB that well-known assumed β PDFs may be used in modeling nonlinear scalar-dependent functions, the next step is to assess models for computing σ_Z from the filtered DNS solution to enable the construction of the presumed SGS PDFs. Results from two such models are presented below.

1. Evaluation of the approximate deconvolution model

All presented results were computed on the DNS (rather than LES) grid. In all figures, the information is shown for several $\overline{\Delta}/\Delta x_{DNS}$ values and for each $\overline{\Delta}/\Delta x_{DNS}$ value for five orders of reconstruction.

Since Eq. (24) is at the core of the compressible ADM procedure, we first inquired about the convergence of Z^{**} to Z according to the approximation of Eq. (25). To explore this issue, we first computed the local second-order moment of Z^* and compared it to the exact moment extracted from the filtered DNS database of the HN600 mixing layer at t_{tr}^* ; the results are illustrated in Fig. (9). Then, we calculated the local second-order moment of Z^{**} and compared it to the exact moment extracted from the filtered DNS database of the

HN600 mixing layer at t_{tr}^* ; the results are illustrated in Fig. (10). Whereas the moment of Z^* converges to that of Z as N increases, the observations are that the moment of the deconvoluted approximate field Z^{**} does not converge to that of Z , and that in some zones this second-order moment is overestimated. This overestimate occurs for a filter width as small as $6\Delta x_{DNS}$ and the situation deteriorates with increasing values of $\bar{\Delta}/\Delta x_{DNS}$. The r.m.s. activity of the difference between Z^{**} and Z^* is presented in Fig. (11). Clearly, this difference increases with the filter width and it also globally increases with N . In order to inquire about the impact of the $Z^{**} \simeq Z^*$ approximation on the SGS-scalar-variance predictions for compressible flows, the ADM procedure is tested using the Favre SGS scalar variance.

The results of Fig. (12) portray the ADM procedure applied to the primitive variable \bar{Z} as in Eq. (21), and the SGS scalar variance is computed using the exact local density and the approximate field Z^* as $\sigma_Z = (\overline{\rho Z^* Z^* / \bar{\rho}}) - (\overline{\rho Z^* / \bar{\rho}}) (\overline{\rho Z^* / \bar{\rho}})$. The results of Fig. (13) differ from those of Fig. (12) in that the ADM procedure is applied to both conservative variables $\bar{\rho}$ and $\bar{\rho Z}$, as one would do in a practical case, and the reconstructed density ρ^* with the approximate field Z^{**} are used to compute the SGS scalar variance according to Eq. (26). Comparing Figs. (12) and (13) at same $\bar{\Delta}/\Delta x_{DNS}$ value, it is clear that using the ADM on the conservative variables improves the model predictions. For example, for $\bar{\Delta}/\Delta x_{DNS} = 8$, a third-order approximation is sufficient for reproducing $\langle \bar{\rho} \sigma_Z \rangle$ at the center of the mixing layer, while by using the primitive quantities only 90% of its value is recovered. The difference between the ADM based on primitive variables and that based on conservative variables becomes enlarged as the filter width increases. For small filter widths ($\bar{\Delta}/\Delta x_{DNS} = 2, 4, 6$), a second-order reconstruction (3 terms) gives very good agreement compared to the exact value. Similarly to the observation of Pantano and Sarkar [16] for incompressible flows, the ADM accuracy depends at least on the level of turbulence, i.e. the Reynolds number, and on the filter width; here, there is the additional complication of variable density which introduces Eq. (24). Figures (14) and (15) show corresponding results for OH750 and OHe600, respectively, when the ADM is performed using the conservative variables.

Despite the better performance of the ADM conservative-variable based model compared to the primitive-variable based one for the third-order approximation, the convergence issue discussed above is still an item of concern when using the approximation Eq. (25). One

conclusion from the presented assessment is that users of the ADM should be cautious when employing this methodology for conservative variables in the context of compressible flows, and results should be carefully verified. Here, because the overestimation of the SGS second-order moment of Z is combined with an underestimation of ρ , the global result is a satisfactory prediction of the SGS (Favre) scalar variance. However, ADM should only be considered here as an approximation rather than an asymptotically convergent expansion.

2. Evaluation of the dynamic gradient-based model

Figure (16) depicts planar averages of the modeled SGS scalar variance conditioned on the exact one extracted from the filtered HN600 DNS database. The plots represent averages at t_{tr}^* over a plane close to the center of the mixing layer ($x_2/\delta_{\omega,0} = 0.44$) as a function of $\bar{\rho}\sigma_Z$, for several filter widths; the vertical arrow represents $\langle\bar{\rho}\sigma_Z\rangle$ and provides an indication of the model fidelity at that particular value. For $\bar{\Delta}/\Delta x_{DNS} = 2$, filtering is clearly performed in the dissipation range, whereas, as an example, for $\bar{\Delta}/\Delta x_{DNS} = 14, 16$ test-filtering is performed close to the production range, and thus neither of these values are in concert with SGS modeling assumptions, but they are here presented for illustrative purposes. At $\bar{\Delta}/\Delta x_{DNS} = 2$, the model based on the Leonard term expansion agrees with the classical model used in conjunction with the correct filter width, but neither one of the models reproduces the exact value, which is better rendered by the classical model utilized in conjunction with an incorrect filter width; this result should serve as a warning that if SGS modeling is tested in the incorrect wavenumber range, results from this test are not necessarily reliable. Over the $\bar{\Delta}/\Delta x_{DNS} = 4$ to 8 range, the new model and the classical model using the correct filter width agree and additionally reproduce the DNS-extracted value, whereas the classical model utilized with the incorrect filter width overpredicts it; however, the $\langle\bar{\rho}\sigma_Z\rangle$ value is equally well predicted by all models. For $\bar{\Delta}/\Delta x_{DNS} = 10, 12$, the fidelity of the new model to predict the exact $\langle\bar{\rho}\sigma_Z\rangle$ is maintained, but that of the classical model with the correct filter deteriorates by underpredicting the template, and for $\bar{\Delta}/\Delta x_{DNS} = 12$ severe underpredictions are obtained with the classical model in conjunction with the incorrect filter width. Most important, the classical model used with either filter widths produces incorrect values even for $\langle\bar{\rho}\sigma_Z\rangle$, whereas the new model maintains high fidelity for this quantity. The robustness of the new model is highlighted by the $\bar{\Delta}/\Delta x_{DNS} = 14, 16$ results where its predictions

are still excellent whereas those with the classical model used with the correct filter width display severe deteriorations and those of the classical model using the incorrect filter width are totally compromised by producing negative values of the SGS scalar variance. Similar to the $\bar{\Delta}/\Delta x_{DNS} = 10, 12$ situation, $\langle \bar{\rho}\sigma_Z \rangle$ is correctly only predicted by the new model, and negative values of the SGS scalar variance are exhibited by the classical model in conjunction with the incorrect filter width. To show that these comparisons are not x_2 -plane dependent, scatter plots at t_{tr}^* of modeled SGS scalar variances against actual values for several filter widths, over a plane close to the periphery of the mixing layer ($x_2/\delta_{\omega,0} = 5.11$) are illustrated in Fig. (17). Only for $\bar{\Delta}/\Delta x_{DNS} = 8$ do the scatter plots overlap for all three models, and predicted negative variances by the classical model using the incorrect filter width appear for a filter ratio of $\bar{\Delta}/\Delta x_{DNS} = 12$ which is smaller than the 14 and 16 where we found negative values in the $x_2/\delta_{\omega,0} = 0.44$ plane.

The Figs. (16) and (17) results were for two selected x_2 planes. To further evaluate the potential of the various models we illustrate in Fig. (18) comparisons of the modeled $\langle \bar{\rho}\sigma_Z \rangle$ with the exact one for the same $\bar{\Delta}/\Delta x_{DNS}$ values and for the entire x_2 significant range. The advantage of the new model over the classical model using the correct filter width is evident for as small value as $\bar{\Delta}/\Delta x_{DNS} = 8$, and comparing with the classical model using the incorrect filter width for as small value as $\bar{\Delta}/\Delta x_{DNS} = 4$. The high fidelity of the new model persists at large $\bar{\Delta}/\Delta x_{DNS}$ whereas it substantially deteriorates for the other two models with increasing $\bar{\Delta}/\Delta x_{DNS}$ values. The model coefficients computed with the three models are depicted in Fig. (19). The indications are that over all x_2 -planes of the mixing layer, the use of the Leonard term expansion for the dynamic model yields model coefficient values which span a smaller range at fixed $\bar{\Delta}/\Delta x_{DNS}$ value than those of the classical model, thereby showing greater potential in maintaining stability of a LES computation.

Corresponding results for the OH750 database are displayed in Fig. (20), (21), (22), and for the OHe600 database are depicted in Figs. (23), (24), (25). For the OH750 conditional averages and mean profiles, the advantage of the new model predictions are less drastic when compared to the classical model than for the HN600 database. The new model and the classical one with the correct filter width are in close agreement, while their results differ from those using the classical procedure with the incorrect filter width $\hat{\bar{\Delta}} = \bar{\Delta}$. For the OHe600 database which has the highest Re_{tr} value among the three examined, the results at small to moderate $\bar{\Delta}/\Delta x_{DNS}$ values are the same as for HN600 for the $x_2/\delta_{\omega,0} = 0.44$

conditional averages, however, for large $\overline{\Delta}/\Delta x_{DNS}$ values close to the production range the predictions from all three models at this particular x_2 -coordinate converge and underestimate the exact value. The advantage of the new model is though evident for predicting the mean SGS variance value (Fig. (24)) over all x_2 -planes of the mixing layer even at large $\overline{\Delta}/\Delta x_{DNS}$ values.

D. Modeled scalar variance in conjunction with the presumed-PDF approach

As a recall, the results of Fig. (8) were obtained with the exact moments of the SGS PDF, as extracted from the filtered DNS database. It is thus important to explore the potential of the two SGS-scalar-variance models examined in Section VIC, namely the ADM using a third-order approximation and the new dynamic gradient-like model. To this end, we use each of these models to construct the β -PDF and assess their performance in reproducing the same filtered non-linear Z -function of Eq. (50), as in Section VIB. Predictions are illustrated in Fig. (26) for HN600 at $\overline{\Delta}/\Delta x_{DNS} = 8$ and $x_2/\delta_{\omega,0} = 0.44$, as an example. Each of the models is evaluated through scatter plots. Independent of the SGS-scalar-variance model used, the predictions are excellent, showing *a priori* the potential of the new σ_Z models combined with a PDF approach to reproduce filtered non-linear functions of the scalar, as would be the dissipation rate, reaction rates, etc. Examining the scatter plots, the ADM results show a smaller dispersion than the gradient-based model. On the other hand, the former is more expensive than the latter and the ADM exhibits convergence problems of the deconvolution series for compressible flow, casting uncertainty on success at high Reynolds numbers where convergence will be further influenced by turbulence-dependent aspects.

VII. SUMMARY AND CONCLUSIONS

The goal of this study was to investigate the modeling of the SGS scalar variance under supercritical-pressure conditions where the real-gas equation of state, the full (3-term) expression for the species mass diffusion flux and transport properties varying with the thermodynamic variables, all preclude assuming that the same models as those at atmospheric pressure conditions are valid. To this end, we followed the classical approach whereby

the SGS scalar variance equation is derived and terms non-computable from the LES solution are modeled, with the intent of providing closure and solving the equation. Thus, we first developed the equation describing the evolution of the SGS scalar variance under supercritical-pressure conditions and highlighted its complexity, particularly recognizing terms not present under atmospheric-pressure conditions. We also presented a second form of the equation which was more adept at highlighting the nature of the new SGS terms and their contributions. The activity of terms in the first form of the equation was examined using a filtered DNS database represented by transitional states describing the mixing of binary species, for three systems of species, under supercritical pressure conditions. The findings were that the activity of some of these new terms is of same magnitude as that of classical terms, meaning that they cannot be neglected. Most important among these new terms were those expressing subgrid activity due to spatially variable diffusion coefficients. The second form of the equation confirmed the importance of the SGS diffusivity and identified for this equation a new dissipation contribution arising from the Soret term. Recognizing that no SGS models are available to model these terms, and thus to close the SGS scalar variance equation, the attention was instead refocused on a second method, that is, the direct modeling of the SGS scalar variance.

This second route first involved examining the SGS PDF of the scalar by assuming the form of the PDF and using the same filtered DNS database to extract the exact moments of the PDF. Three PDF forms were investigated - the Dirac, Gaussian and β PDF - and the results showed that they ranked in increasing success in the order cited. This encouraging ability of the β PDF motivated the development of two direct models for the SGS scalar variance. The first SGS-scalar-variance model was based on the ADM procedure reformulated for application to compressible flows. The second SGS-scalar-variance model was based on a gradient-like dynamic model using the Leonard term expansion. Success with these two models motivated a reassessment of the ability to model a filtered non-linear function of the scalar by using the β PDF in conjunction with either one of these models for the SGS scalar variance, and with the mean computed from the filtered DNS. The findings were that either one of the direct SGS scalar variance models provided a high-fidelity duplication of the DNS-extracted SGS PDF, which is manifested by the excellent reproduction of a filtered non-linear function of the scalar. Although the ADM was generally more accurate than the gradient-based model, it was shown that the ADM procedure is not necessarily convergent

for compressible flows; thus, the results could be interpreted as an approximation rather than a model the accuracy of which asymptotically increases with series higher truncation order.

Therefore, although supercritical-pressure conditions entail new challenges in the modeling of the SGS scalar variance, these challenges were met for describing the mixing of several binary-species systems. Further *a posteriori* studies should reveal the true potential of these models, and applications to reacting flows would represent the ultimate test.

APPENDIX A: ASSESSMENT OF THE ONE-DIMENSIONAL LAMINAR SCALAR DISSIPATION FOR TRANSITIONAL SUPERCRITICAL-PRESSURE MIXING LAYERS

The dissipation rate in the context of the flamelet model is often modeled in the framework of a one-dimensional counterflow [48]. Under this assumption, an analytical solution for the dissipation rate is available under subcritical conditions [1] which is the functional form of Eq. (50). In order to evaluate whether this form still holds in the present case, the averages of both χ_T and χ_F of Eqs. (48) and (49) are computed from the DNS conditioned on $F(Z)$ (Eq. 50). The results are illustrated in Fig. (27). For both χ_T and χ_F , there is a linear dependency on $F(Z)$ in zones corresponding to large values of Z , while departures are observed for smaller values of Z . This indicates that $F(Z)$ is unreliable since it cannot handle regions of fluid mixing where the gradients would be largest.

Acknowledgment

This study was conducted at the Jet Propulsion Laboratory (JPL) of the California Institute of Technology (Caltech) under sponsorship of the U.S. Department of Energy and of the U.S. Air Force Office of Scientific Research. Computational resources were provided by the supercomputing facility at JPL.

-
- [1] N. Peters, *Turbulent combustion* Cambridge University Press, Cambridge UK (2000).
 - [2] A. W. Cook and J. Riley, A subgrid model for equilibrium chemistry in turbulent flows, *Phys. Fluids* 6, 2868 (1994).

- [3] J. Jiménez, A. Linan, M. M. Rogers and F. J. Higuera, A priori testing of subgrid models for chemically reacting non-premixed turbulent shear flows, *J. Fluid Mech.* 349, 149 (1997).
- [4] C. D. Pierce and P. Moin, A dynamic model for subgrid variance and dissipation rate of a conserved scalar, *Phys. Fluids* 10 (12), 3041 (1998).
- [5] G. Balarac, H. Pitsch and V. Raman, Development of a dynamic model for the subfilter scalar variance using the concept of optimal estimators, *Phys. Fluids* 20, 035114 (2008).
- [6] C. Jiménez, F. Ducros, B. Cuenot and B. Bédard, Subgrid scale variance and dissipation of a scalar field in large eddy simulations. *Phys. Fluids* 13(6), 1748 (2001).
- [7] C. Pera, J. Réveillon, L. Vervisch and P. Domingo, Modeling subgrid scale mixture fraction variance in LES of evaporating spray, *Combust. Flame* 146, 635 (2006).
- [8] N. A. Okong'o and J. Bellan, Direct numerical simulation of a transitional supercritical binary mixing layer: heptane and nitrogen, *J. Fluid Mech.* 464, 1 (2002).
- [9] L. C. Selle, N. A. Okong'o, J. Bellan and K. G. Harstad, Modelling of subgrid-scale phenomena in supercritical transitional mixing layers: an a priori study, *J. Fluid Mech.* 593, 57 (2007).
- [10] N. Okong'o, K. Harstad and J. Bellan, Direct numerical simulations of O_2/H_2 temporal mixing layers under supercritical conditions, *AIAA J.* 40(5), 914 (2002).
- [11] N. A. Okong'o and J. Bellan, Turbulence and fluid-front area production in binary-species, supercritical, transitional mixing layers, *Phys. Fluids* 16(5), 1467 (2004).
- [12] E. S. Taşkinoglu and J. Bellan, A posteriori study using a DNS database describing fluid disintegration and binary-species mixing under supercritical pressure: heptane and nitrogen, *J. Fluid Mech.* 645, 211 (2010)
- [13] N. A. Okong'o and J. Bellan, Entropy production of emerging turbulent scales in a temporal supercritical n-heptane/nitrogen three-dimensional mixing layer, *Proc. Combust. Inst.* 28, 497 (2000).
- [14] H. Pitsch and H. Steiner, Large-eddy simulation of a turbulent piloted methane-air diffusion flame (Sandia flame D), *Phys. Fluids* 12 (10), 2541 (2000).
- [15] V. John, I. Angelov, A. A. Öncül and D. Thévenin, Techniques for the reconstruction of a distribution from a finite number of its moments, *Chem. Eng. Sci.* 62, 2890 (2007).
- [16] C. Pantano and S. Sarkar, A subgrid model for nonlinear functions of a scalar, *Phys. Fluids* 13, 3803 (2001).
- [17] J. P. Mellado, S. Sarkar and C. Pantano, Reconstruction subgrid models for nonpremixed

- combustion, *Phys. Fluids* 15, 3280 (2003).
- [18] S. B. Pope, PDF methods for turbulent reactive flows, *Prog. Energy Combust. Sci.* 11, 119 (1985).
 - [19] P. J. Colucci, F. A. Jaber and P. Givi, Filtered density function for large eddy simulation of turbulent reacting flows, *Phys. Fluids* 10 (2), 499 (1998).
 - [20] H. Steiner and W. K. Bushe, Large eddy simulation of a turbulent reacting jet with conditional source-term estimation, *Phys. Fluids* 13 (3), 754 (2001).
 - [21] F. A. Jaber, P. J. Colucci, S. James, P. Givi and S. B. Pope, Filtered mass density function for large-eddy simulation of turbulent reacting flows, *J. Fluid Mech.* 401, 85 (1999).
 - [22] V. Raman, H. Pitsch and R. O. Fox, Hybrid large-eddy simulation/Lagrangian filtered-density-function approach for simulating turbulent combustion, *Combust. Flame* 143, 56 (2005).
 - [23] R. Fox, *Computational Models for Turbulent Reacting Flows*, Cambridge University Press, Cambridge (2003).
 - [24] H. Pitsch, Large-Eddy Simulation of Turbulent Combustion, *Annu. Rev. Fluid Mech.* 38, 453 (2006).
 - [25] A. Moreau, O. Teytaud and J. P. Bertoglio, Optimal estimation for large-eddy simulation of turbulence and application to the analysis of subgrid models, *Phys. Fluids* 18, 105101 (2006).
 - [26] E. A. Brizuela and R. W. Bilger, On the eddy break-up coefficient, *Combust. flame* 104, 208 (1996)
 - [27] P. Sagaut, *Large-Eddy Simulation for Incompressible Flows: An Introduction*, Springer-Verlag, Berlin/New York (2001).
 - [28] S. Stolz and N. A. Adams, An approximate deconvolution procedure for large-eddy simulation, *Phys. Fluids* 11, 1699 (1999).
 - [29] P. H. van Cittert, Zum Einfluss der Spaltbreite auf die Intensitätsverteilung in Spektrallinien ii., *Zeitschrift für Physik* 69, 298 (1931).
 - [30] J. A. Domaradzki and N. A. Adams, Direct modelling of subgrid scales of turbulence in large eddy simulations, *Journal of Turbulence* 3 (2002).
 - [31] S. Stolz, N. A. Adams and L. Kleiser, An approximate deconvolution model for large-eddy simulation with application to incompressible wall-bounded flows, *Phys. Fluids* 13(4), 997 (2001).
 - [32] S. Stolz, N. A. Adams and L. Kleiser, The approximate deconvolution model for large-eddy

- simulations of compressible flows and its application to shock-turbulent-boundary-layer interaction, *Phys. Fluids* 13 (10), 2985 (2001).
- [33] T. Dubois, J. A. Domaradzki and A. Honien, The subgrid-scale estimation model applied to large eddy simulations of compressible turbulence, *Phys. Fluids* 14(5), 1781 (2002).
 - [34] M. Germano, U. Piomelli, P. Moin and W. H. Cabot, A dynamic subgrid-scale eddy viscosity model, *Phys. Fluids A* 3 (7), 1760 (1991).
 - [35] P. Moin, K. Squires, W. H. Cabot, and S. Lee, A dynamic subgrid-scale model for compressible turbulence and scalar transport, *Phys. Fluids A* 3, 2746 (1991).
 - [36] C. Wall, B. J. Boersma and P. Moin, An evaluation of the assumed beta probability density function subgrid-scale model for large eddy simulation of nonpremixed, turbulent combustion with heat release, *Phys. Fluids* 12, 2522 (2000).
 - [37] S. H. Kim and H. Pitsch, Mixing characteristics and structure of a turbulent jet diffusion flame stabilized on a bluff-body, *Phys. Fluids* 18, 075103 (2006).
 - [38] J. Bardina, J. H. Ferziger and W. C. Reynolds. Improved subgrid scale models for large eddy simulation, AIAA paper 80-1357 (1980).
 - [39] J. Réveillon and L. Vervisch, Response of the dynamic LES model to heat release induced effects, *Phys. Fluids* 8 (8), 2248 (1996).
 - [40] P. DesJardin and S. Frankel, Large eddy simulation of a nonpremixed reacting jet: Application and assessment of subgrid-scale combustion models, *Phys. Fluids* 10 (9), 2298 (1998).
 - [41] K. Lilly, A proposed modification of the Germano subgrid-scale closure method, *Phys. Fluids A* 4, 633 (1992).
 - [42] M. Germano, Turbulence: The filtering approach, *J. Fluid Mech.* 238, 325 (1992).
 - [43] A. W. Vreman, Direct and Large-Eddy Simulation of the compressible turbulent mixing layer, PhD Dissertation, University of Twente (1995).
 - [44] K. W. Bedford and W. K. Yeo, in *Large Eddy Simulation of Complex Engineering and Geophysical Flows*, edited by B. Galperin and S. A. Orszag Cambridge University Press, New York (1993).
 - [45] C. Brun and R. Friedrich, Modeling the test SGS tensor T_{ij} : An issue in the dynamic approach, *Phys. Fluids* 13 (8), 2373 (2001).
 - [46] B. Vreman, B. Geurts and H. Kuerten, On the formulation of the dynamic mixed subgrid scale model, *Phys. Fluids* 6, 4057 (1994).

- [47] A. W. Cook and J. Riley, Subgrid-Scale modeling for turbulent reacting flows, *Combust. Flame* 112, 593 (1998).
- [48] A. W. Cook, J. J. Riley, G. A. Kosály, Laminar flamelet approach to subgrid-scale chemistry in turbulent flows, *Combust. Flame* 109, 332 (1997).

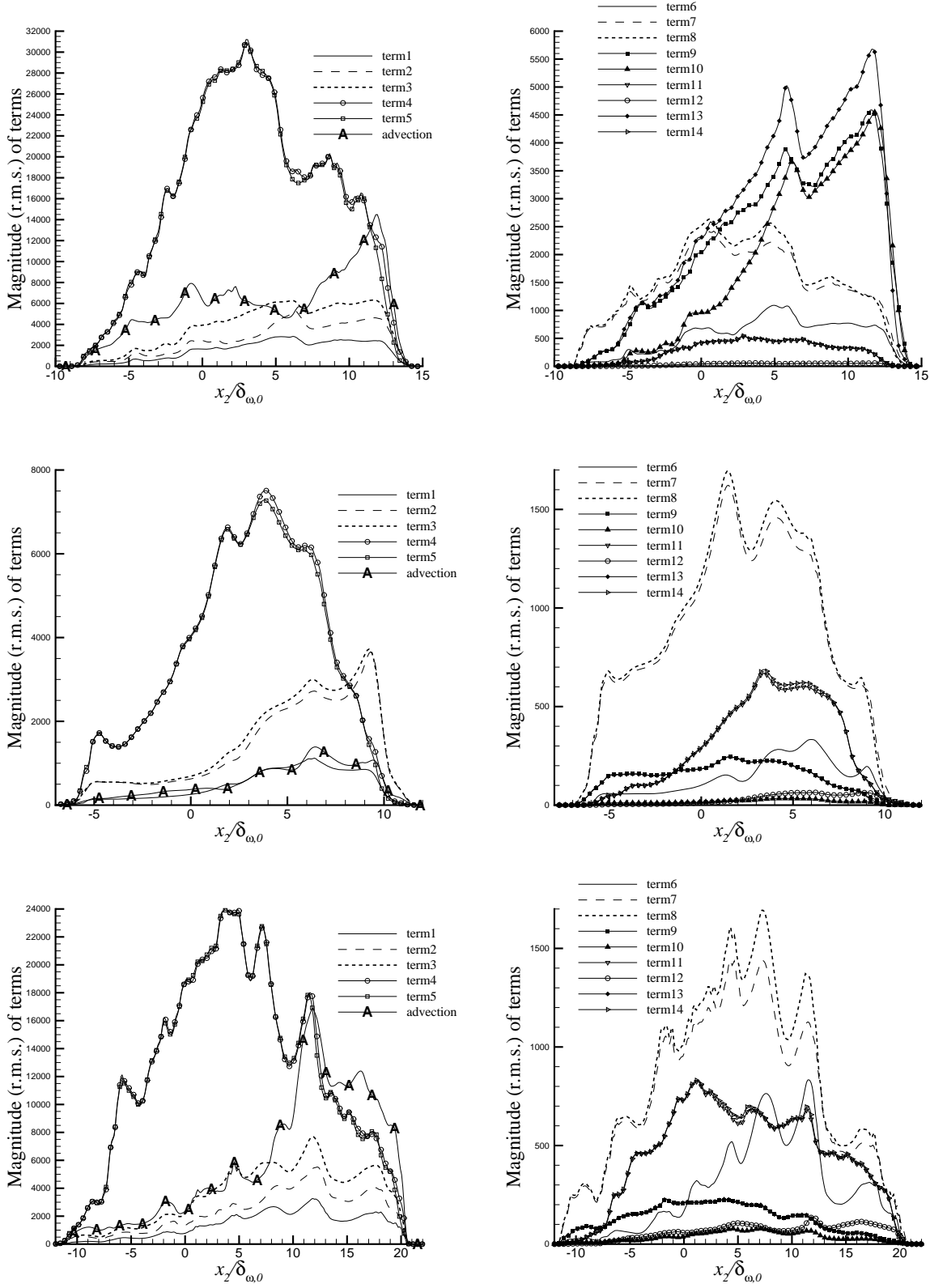


FIG. 1: Planar r.m.s. activity of terms in Eq. (4) as extracted from the filtered DNS databases at t_{tr}^* . Top: HN600; center: OH750; bottom: OHe600. $\bar{\Delta}/\Delta x_{DNS} = 8$. Units are $\text{kg}/(\text{m}^3 \text{ s})$.

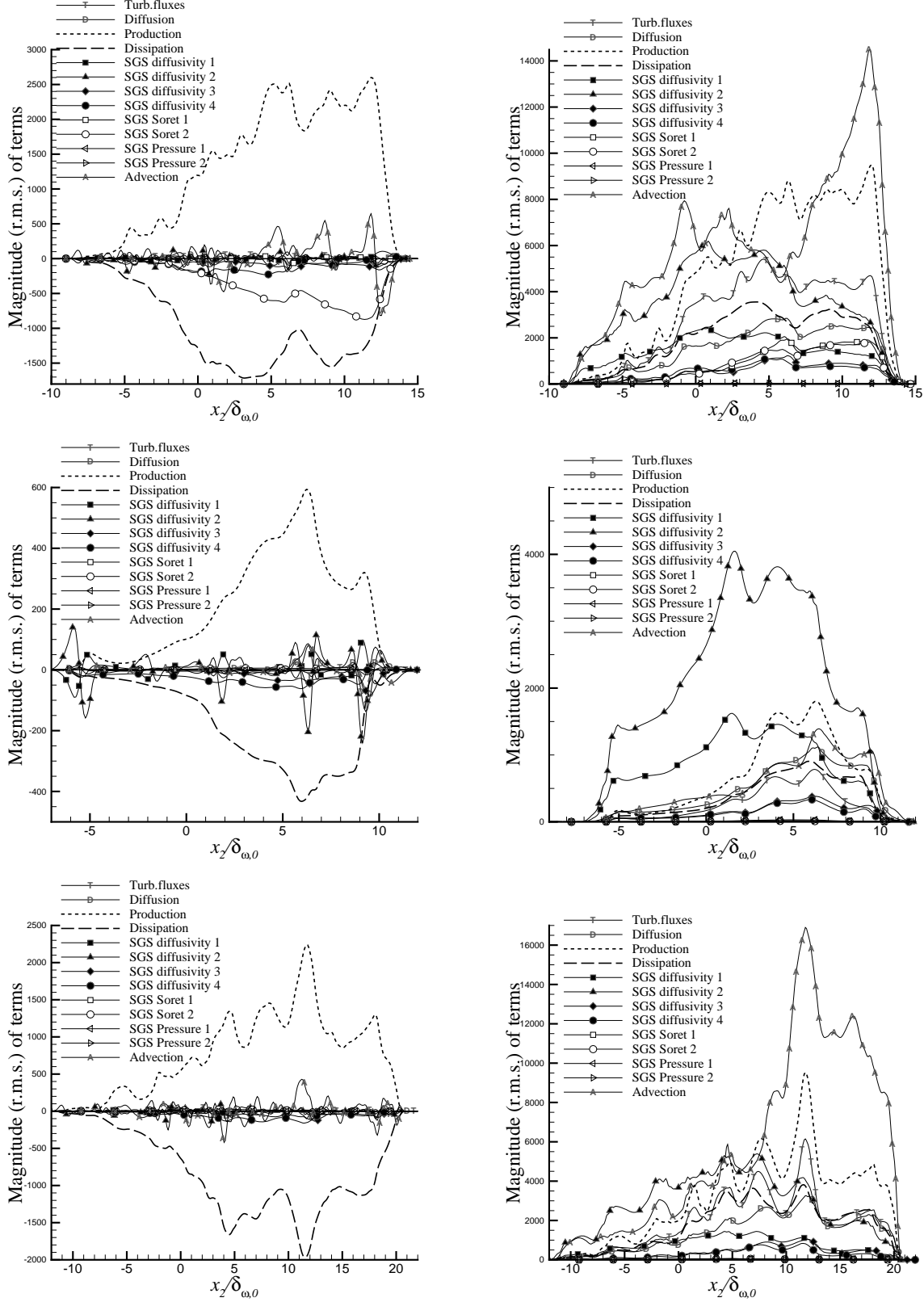


FIG. 2: Planar averages (left) and planar r.m.s. activity (right) of terms in Eq. (9). Extracted from the filtered DNS databases at t_{tr}^* . Top: HN600; center: OH750; bottom: OHe600. $\bar{\Delta}/\Delta x_{DNS} = 8$. Units are $\text{kg}/(\text{m}^3 \text{ s})$.

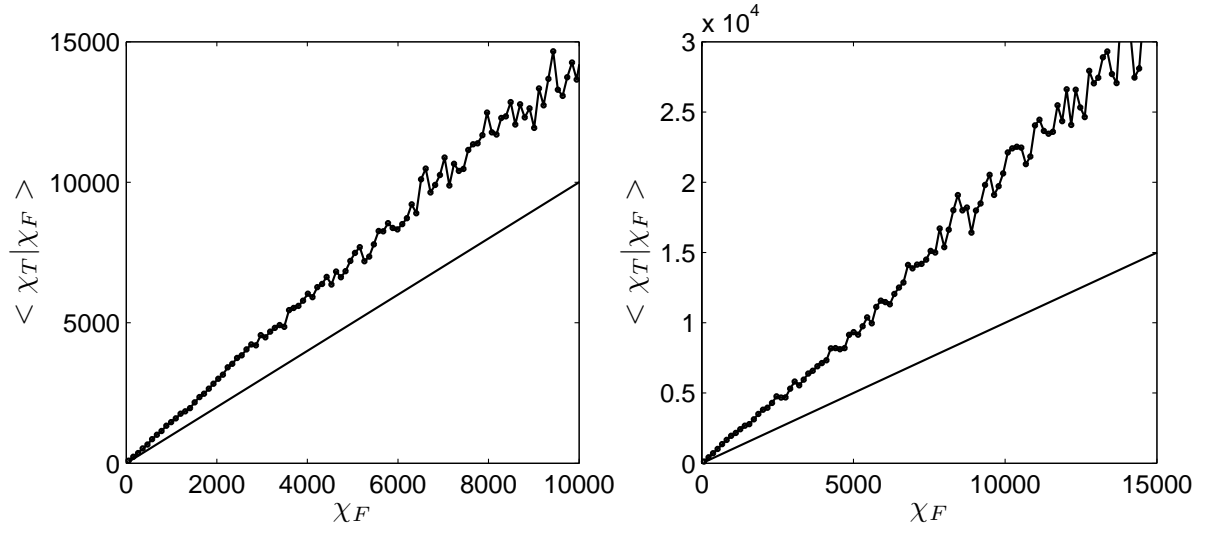


FIG. 3: Conditional average of χ_T on χ_F extracted from the HN600 DNS database over planes of coordinates $x_2/\delta_{\omega,0} = 0.44$ (left) and $x_2/\delta_{\omega,0} = 5.11$ (right) at t_{tr}^* . $\overline{\Delta}/\Delta x_{DNS} = 8$.

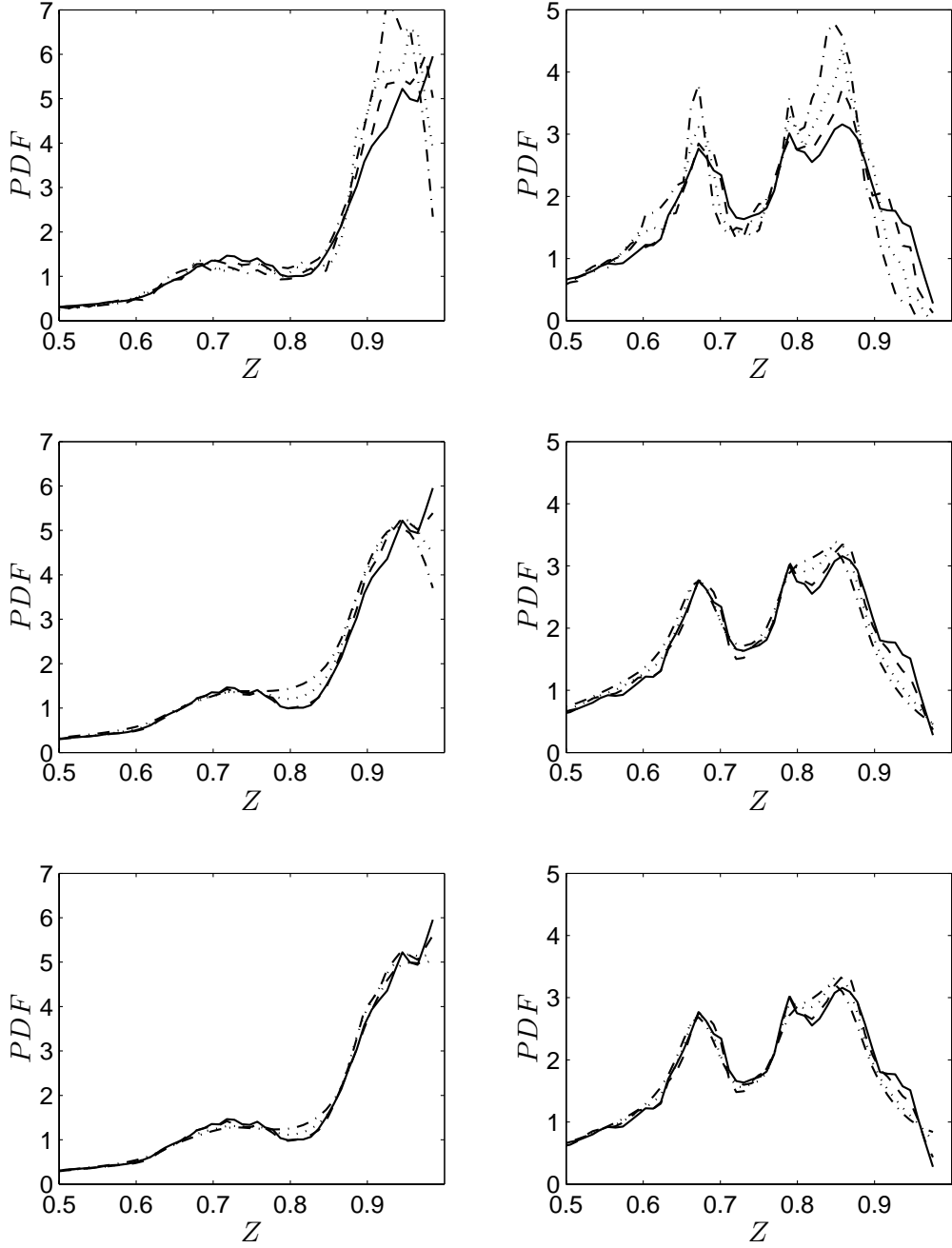


FIG. 4: Filtered PDFs $\langle f_{sgs_c} \rangle_c$, from the HN600 DNS at t_{tr}^* over planes of coordinates $x_2/\delta_{\omega,0} = 0.44$ (left) and $x_2/\delta_{\omega,0} = 5.11$ (right). Exact SGS: solid lines. Assumed PDFs are the Dirac (top), the Gaussian (center) and the Beta (bottom) functions. $\overline{\Delta}/\Delta x_{DNS} = 4$, dashed lines; $\overline{\Delta}/\Delta x_{DNS} = 8$, dotted lines; $\overline{\Delta}/\Delta x_{DNS} = 12$, dot-dashed lines.

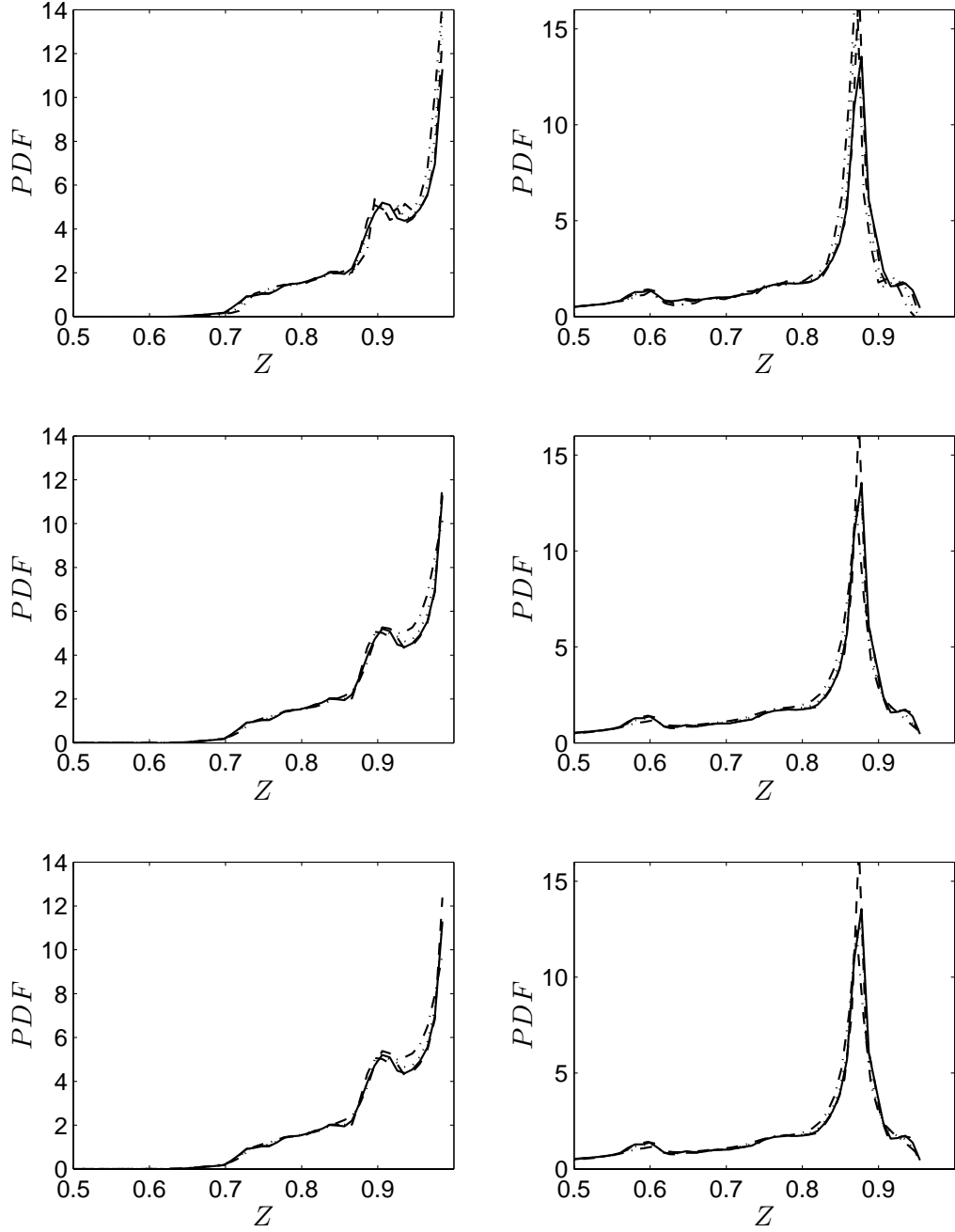


FIG. 5: Filtered PDFs $\langle f_{sgs_c} \rangle_c$, from the OH750 database at t_{tr}^* over planes of coordinates $x_2/\delta_{\omega,0} = 0.44$ (left) and $x_2/\delta_{\omega,0} = 5.11$ (right). Exact SGS: solid lines. Assumed PDFs are the Dirac (top), the Gaussian (center) and the Beta (bottom) functions. $\overline{\Delta}/\Delta x_{DNS} = 4$, dashed lines; $\overline{\Delta}/\Delta x_{DNS} = 8$, dotted lines; $\overline{\Delta}/\Delta x_{DNS} = 12$, dot-dashed lines.

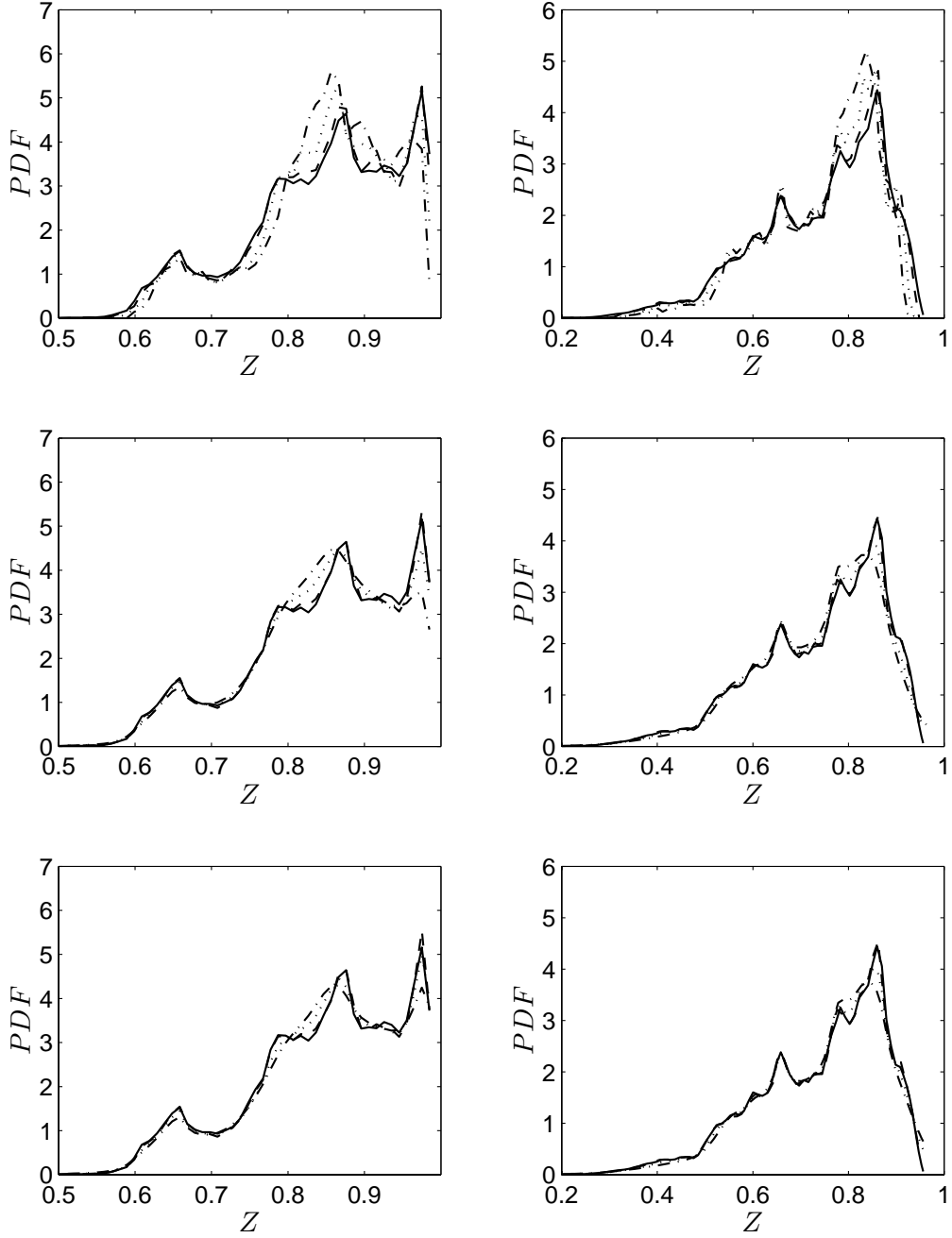


FIG. 6: Filtered PDFs $\langle f_{sgsc} \rangle_c$, from the OHe600 database at t_{tr}^* over planes of coordinates $x_2/\delta_{\omega,0} = 0.44$ (left) and $x_2/\delta_{\omega,0} = 5.11$ (right). Exact SGS: solid lines. Assumed PDFs are the Dirac (top), the Gaussian (center) and the Beta (bottom) functions. $\overline{\Delta}/\Delta x_{DNS} = 4$, dashed lines; $\overline{\Delta}/\Delta x_{DNS} = 8$, dotted lines; $\overline{\Delta}/\Delta x_{DNS} = 12$, dot-dashed lines.

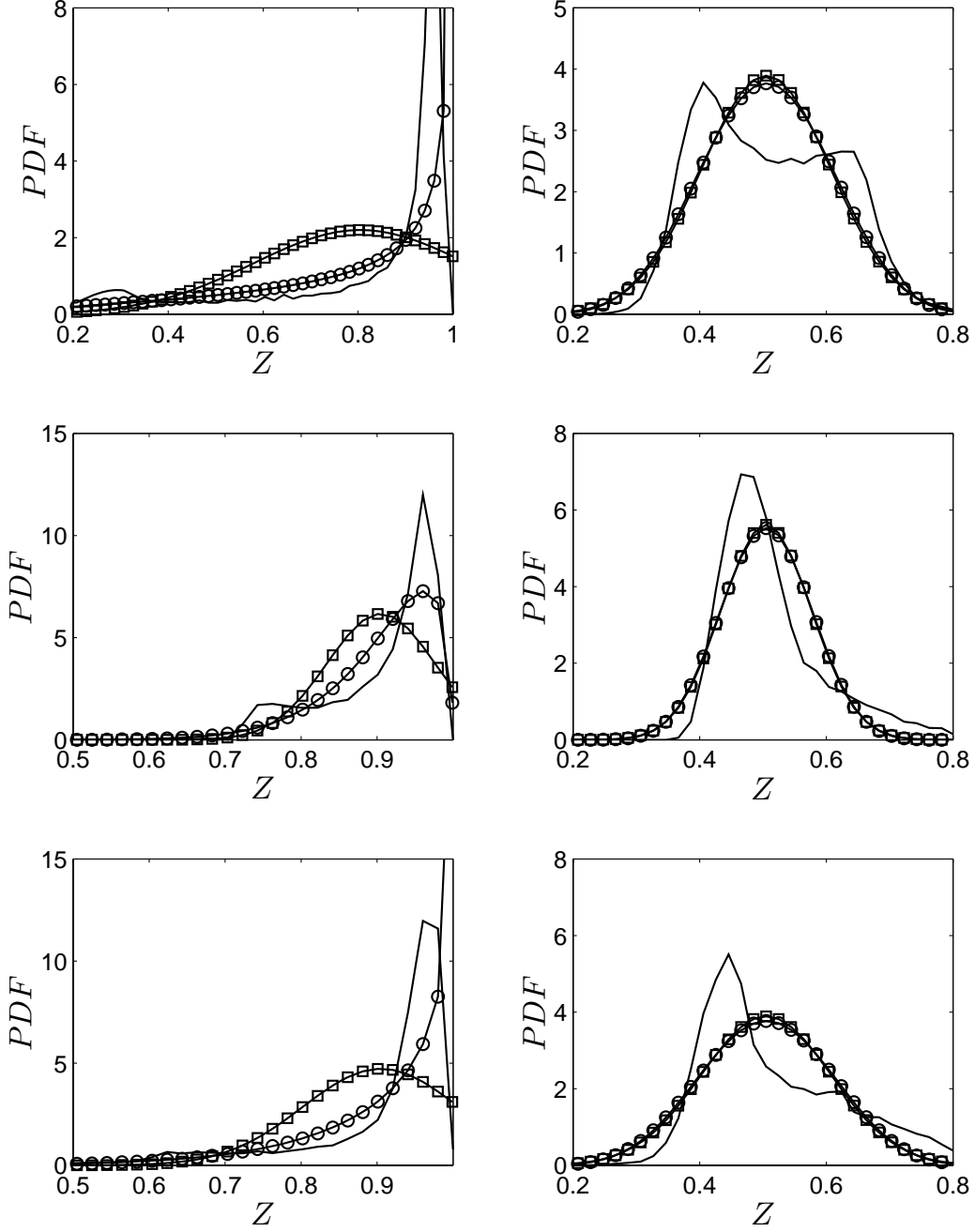


FIG. 7: Conditional expectation of $f_{sgsc}(\xi; \tilde{\xi}, \sigma_\xi)$ over $(\tilde{\xi}, \sigma_\xi)$ and over the slab at $x_2/\delta_{\omega,0} = \pm 5.3$. Top: HN600, $\tilde{\xi} = 0.805 \pm 0.005, \sigma_\xi = 0.0505 \pm 0.0005$ (left) and $\tilde{\xi} = 0.505 \pm 0.005, \sigma_\xi = 0.0105 \pm 0.0005$ (right). Center: OH750, $\tilde{\xi} = 0.905 \pm 0.005, \sigma_\xi = 0.00505 \pm 0.00005$ (left) and $\tilde{\xi} = 0.505 \pm 0.005, \sigma_\xi = 0.00505 \pm 0.00005$ (right). Bottom: OHe600, $\tilde{\xi} = 0.905 \pm 0.005, \sigma_\xi = 0.0105 \pm 0.0005$ (left) and $\tilde{\xi} = 0.505 \pm 0.005, \sigma_\xi = 0.0105 \pm 0.0005$ (right). $\overline{\Delta}/\Delta x_{DNS} = 8$.

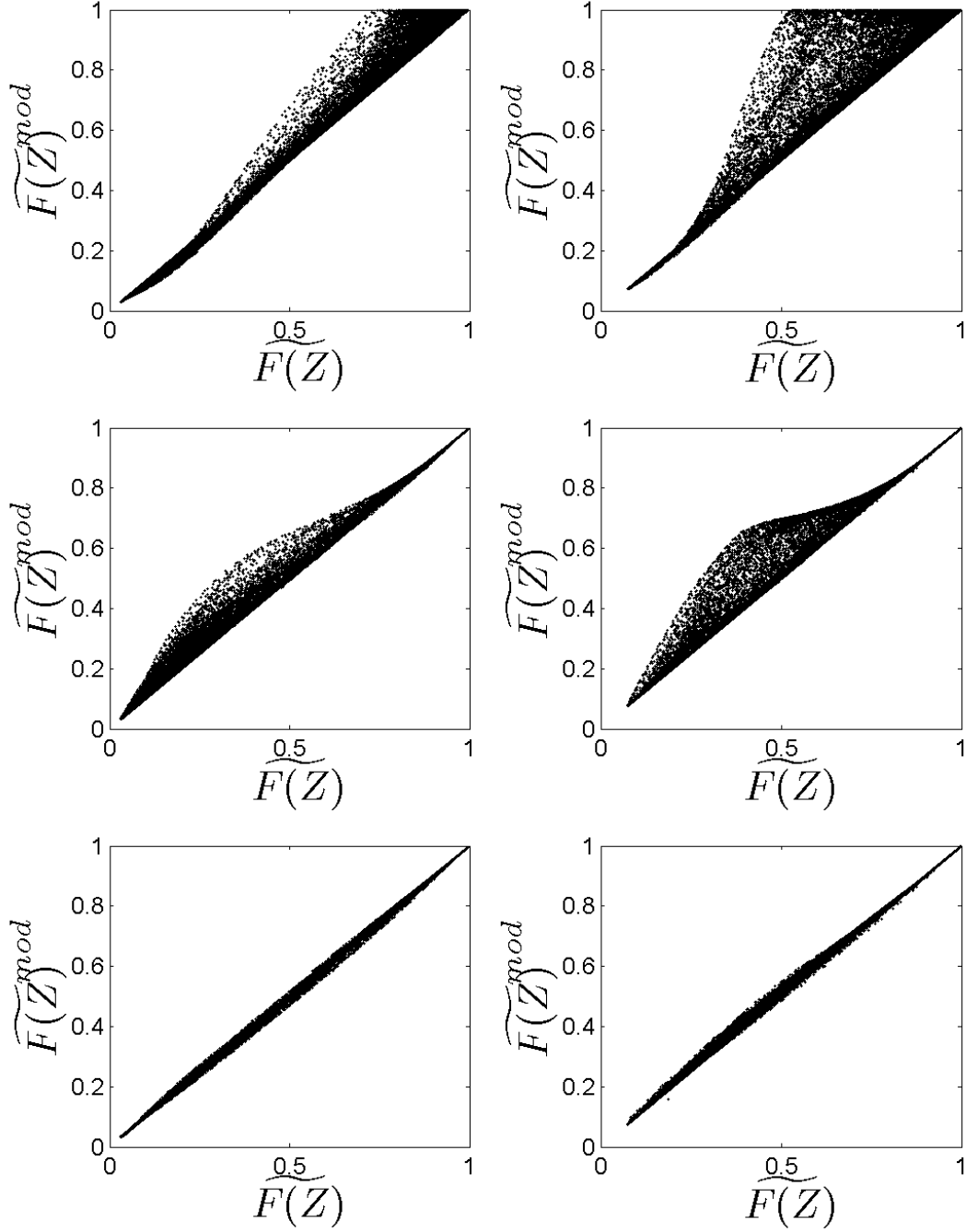


FIG. 8: Scatter plot of the modeled function $\widetilde{F(Z)}^{mod}$ versus the exact quantity $\widetilde{F(Z)}$ computed over planes $x_2/\delta_{\omega,0} = 0.44$ (left) and $x_2/\delta_{\omega,0} = 5.11$ (right). The exact quantity is the filtered HN600 DNS at t_{tr}^* and the models are the Dirac PDF (top), Gaussian PDF (center) and β PDF (bottom). $\overline{\Delta}/\Delta x_{DNS} = 8$.

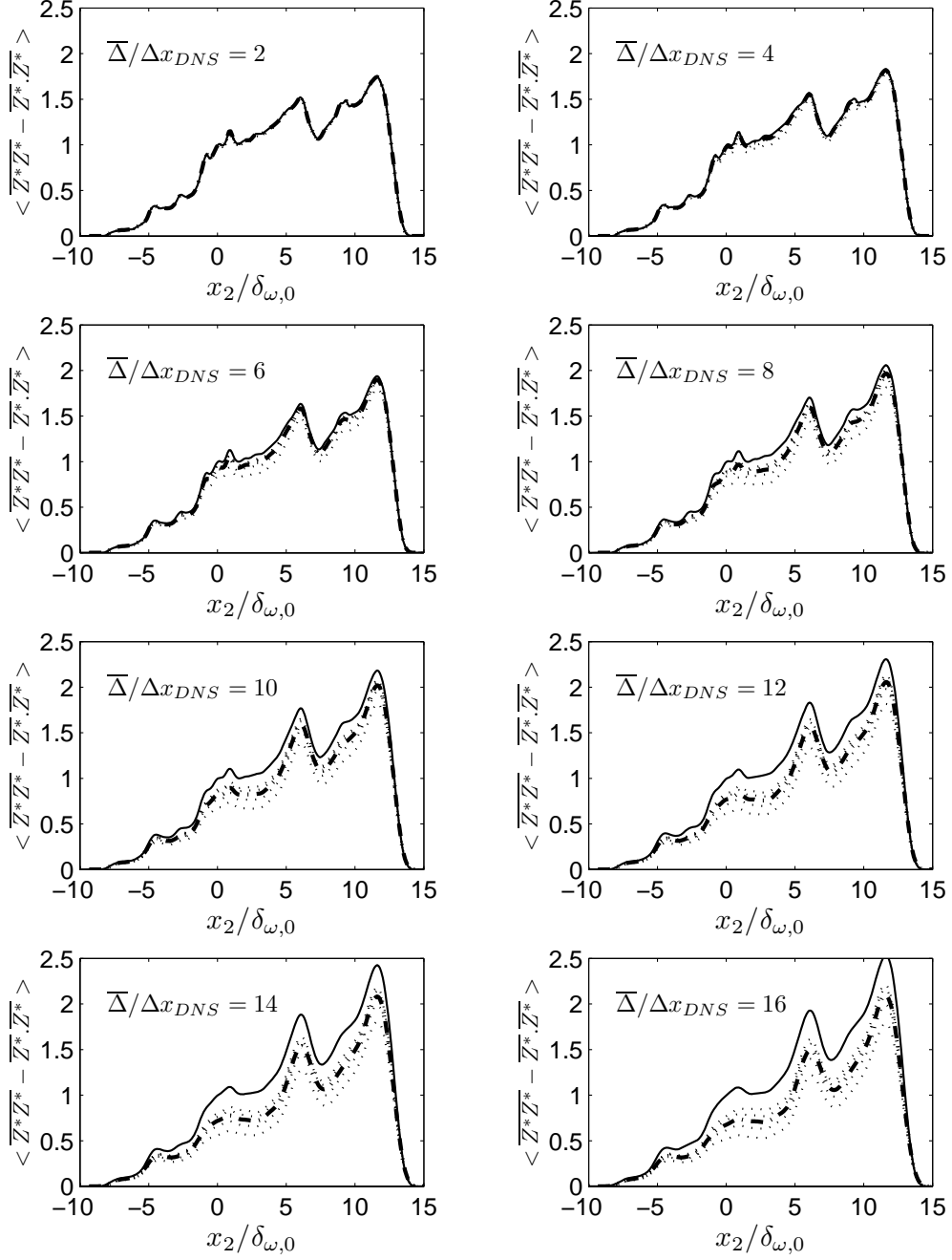


FIG. 9: Predictions of the SGS scalar variance using the deconvoluted field Z^* . Several orders of approximation are shown for different filter widths at t_{tr}^* for the HN600 mixing layer. Exact SGS scalar variance: solid line. Dotted lines are the first to fifth order approximations, the third order being distinguished by a dash-dotted line. Variances are non-dimensionalized by the exact value at the center of the mixing layer.

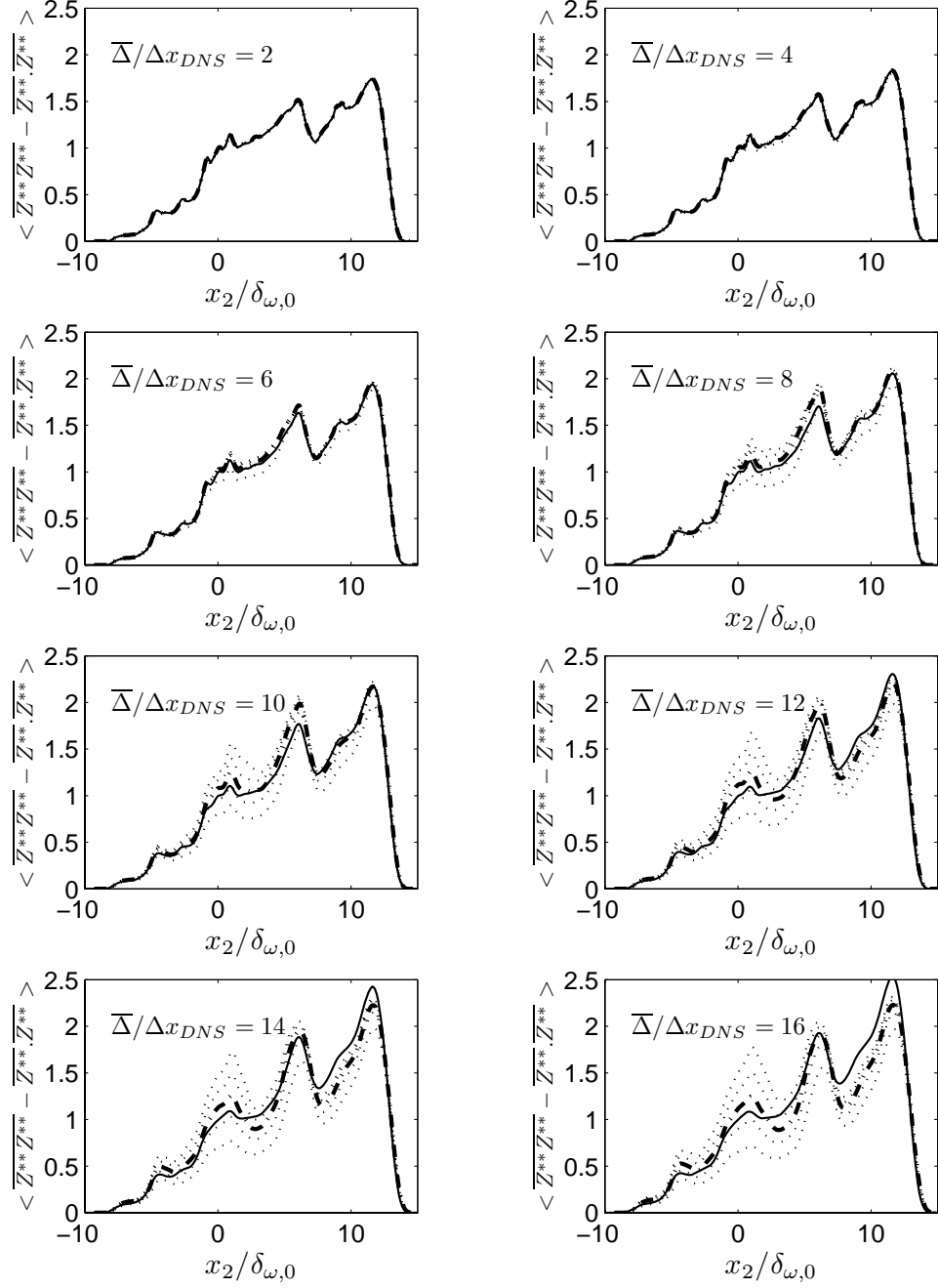


FIG. 10: Predictions of the SGS scalar variance using the deconvoluted field Z^{**} . Several orders of approximation are shown for different filter widths at t_{tr}^* for the HN600 mixing layer. Exact SGS scalar variance: solid line. Dotted lines are the first to fifth order approximations, the third order being distinguished by a dash-dotted line. Variances are non-dimensionalized by the exact value at the center of the mixing layer.

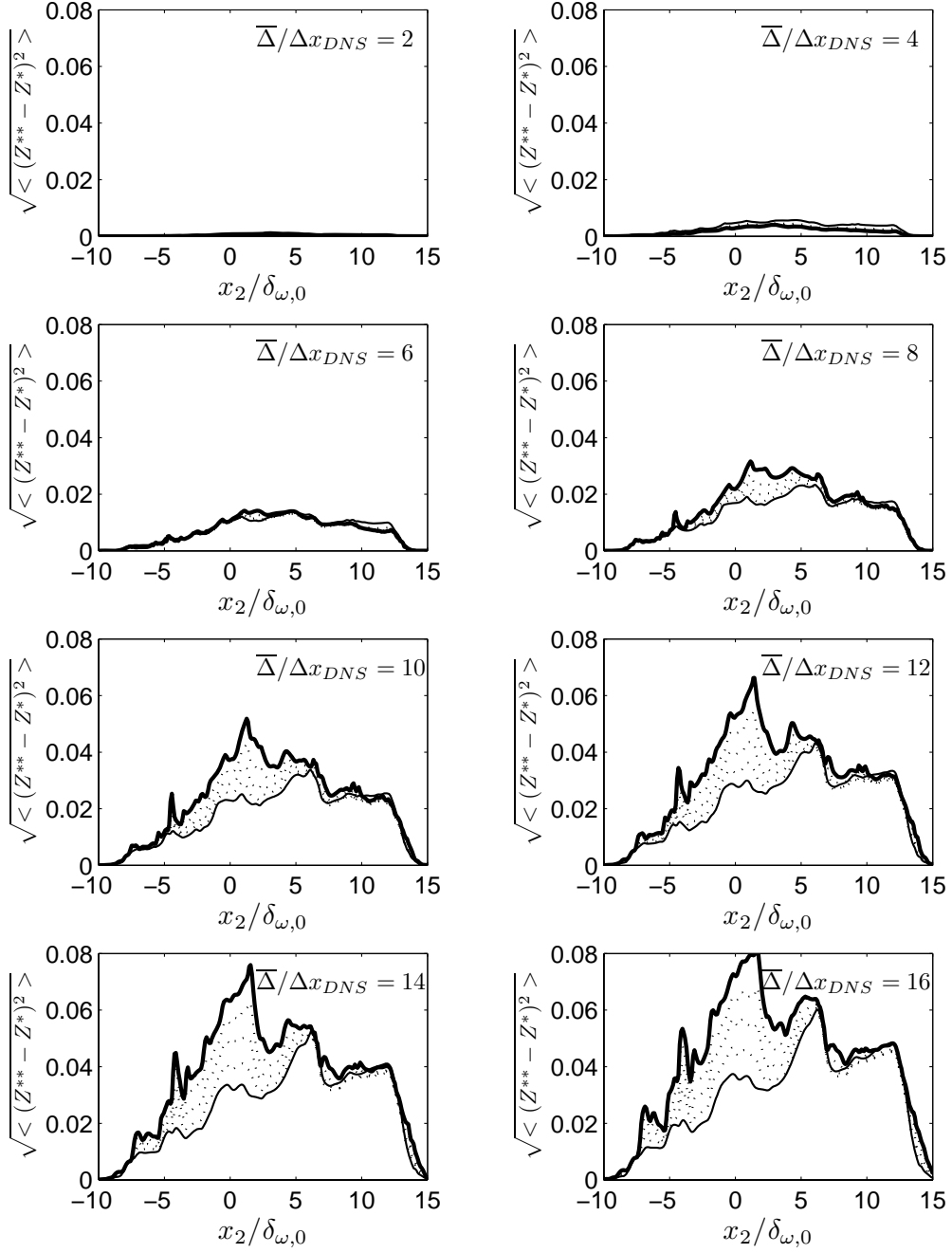


FIG. 11: Planar r.m.s. activity of the field $(Z^{**} - Z^*)$ for several orders of ADM approximation and different filter widths at t_{tr}^* for the HN600 mixing layer. Thin solid line: first order of approximation; thick solid line: fifth order of approximation. Dotted lines are the second to fourth order approximations.

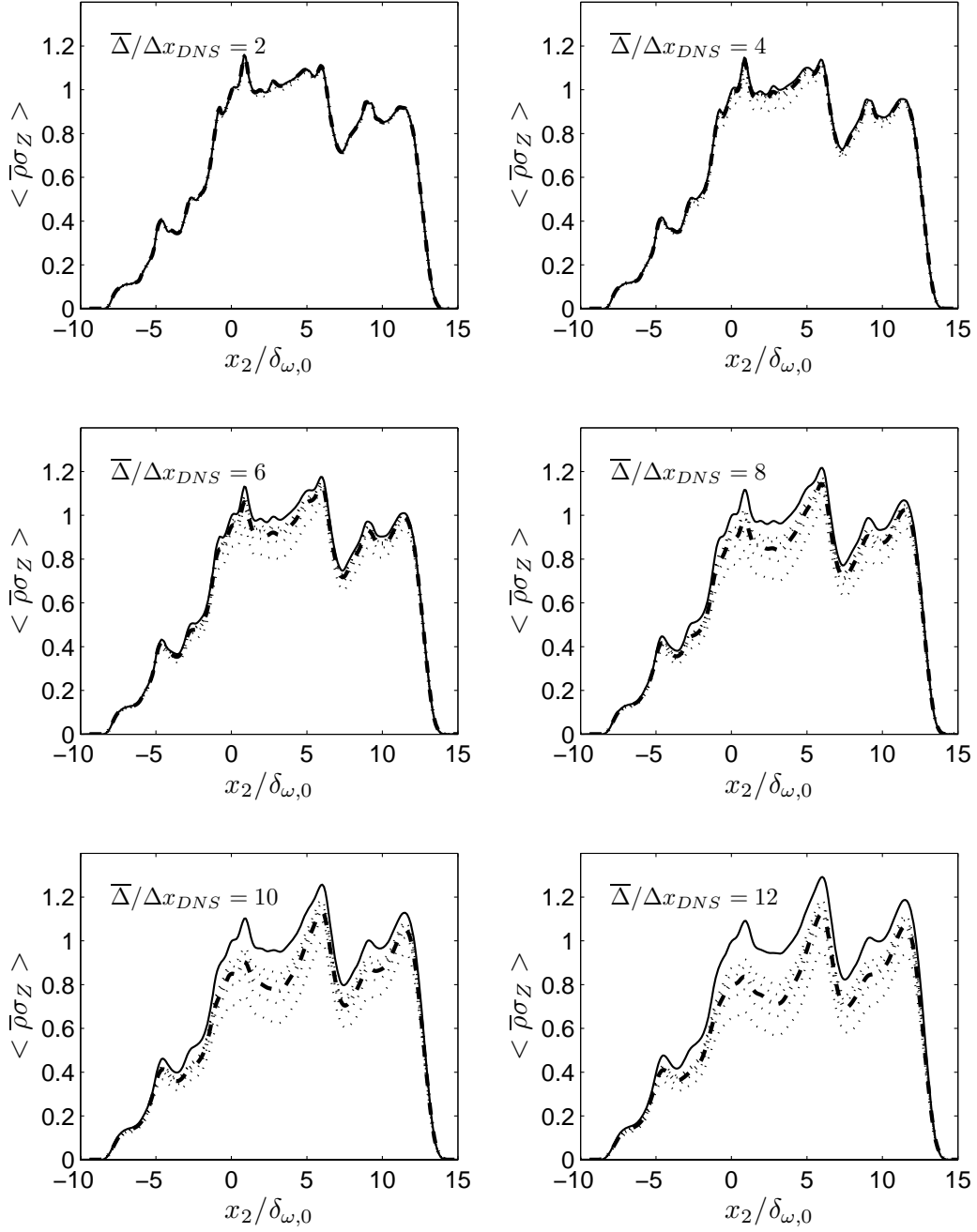


FIG. 12: Predictions of the Favre SGS scalar variance using ADM applied to the primitive quantity. Several orders of approximation are shown for different filter widths at t_{tr}^* for the HN600 mixing layer. Exact SGS scalar variance: solid line. Dotted lines are the first to fifth order approximations, the third order being distinguished by a dash-dotted line. Variances are non-dimensionalized by the exact value at the center of the mixing layer.

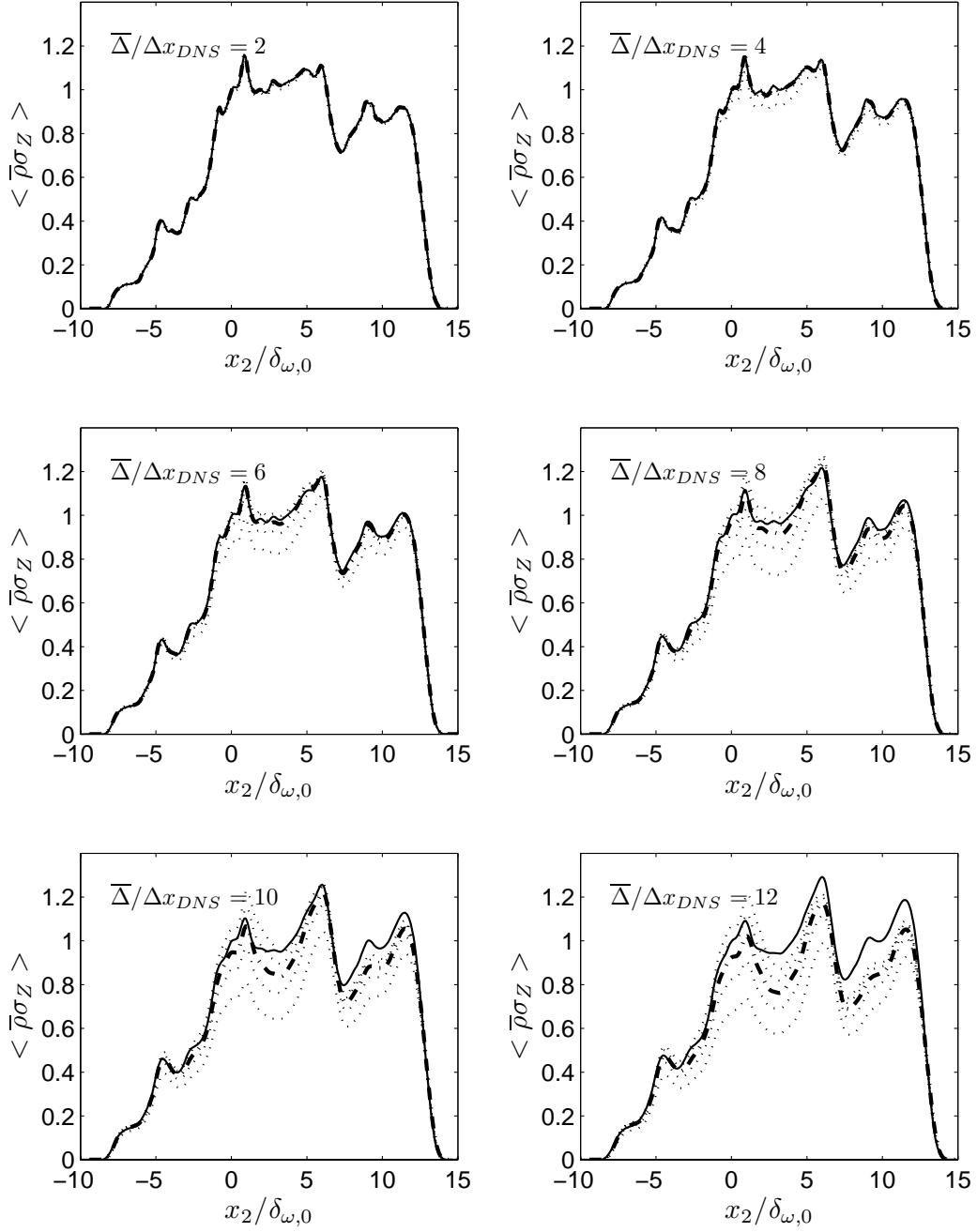


FIG. 13: Predictions of the Favre SGS scalar variance using ADM applied to conservative quantities. Several orders of approximation are shown for different filter widths at t_{tr}^* for the HN600 mixing layer. Exact SGS scalar variance: solid line. Dotted lines are the first to fifth order approximations, the third order being distinguished by a dash-dotted line. Variances are non-dimensionalized by the exact value at the center of the mixing layer.

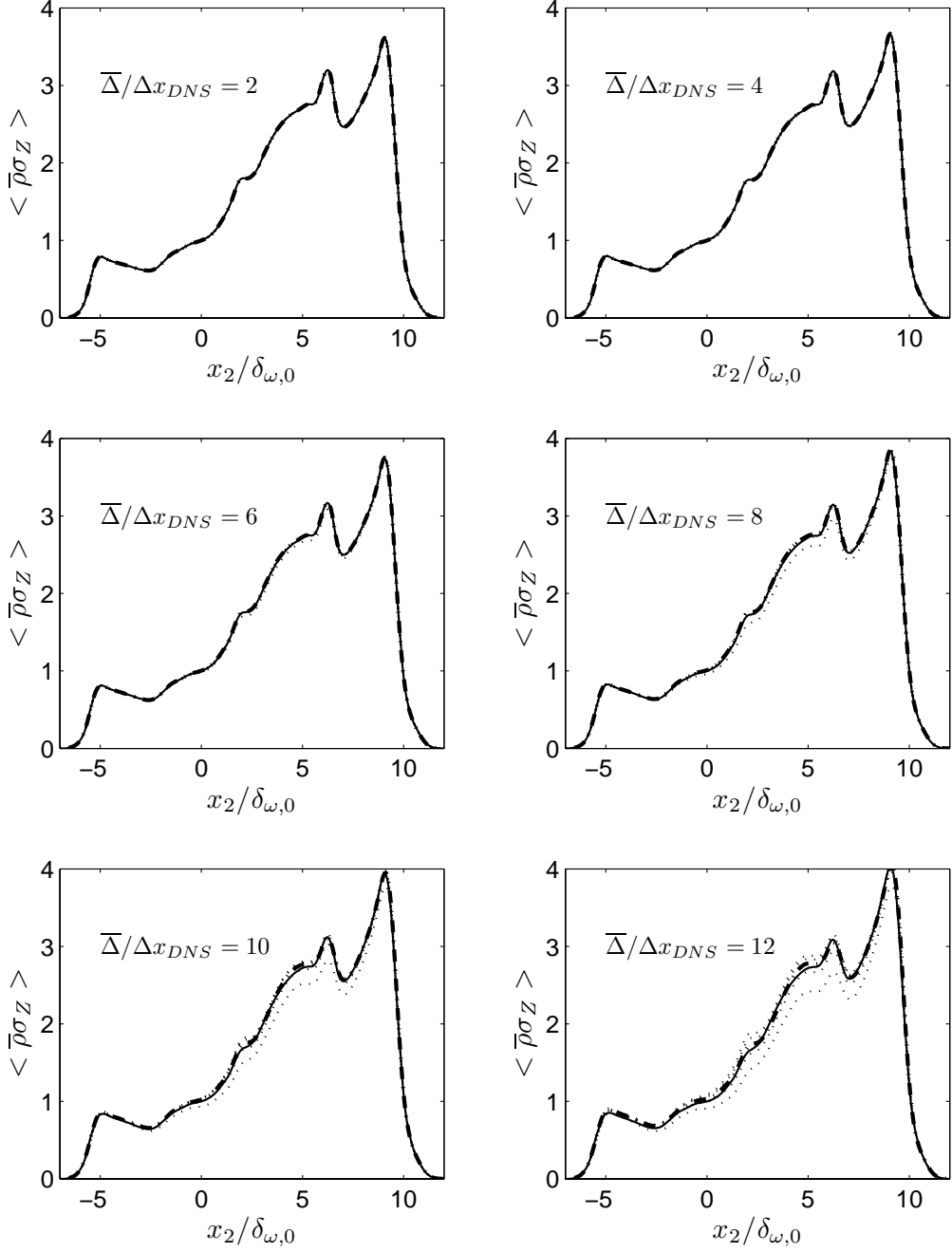


FIG. 14: Predictions of the Favre SGS scalar variance using ADM applied to conservative quantities. Several orders of approximation are shown for different filter widths at t_{tr}^* , for the OH750 mixing layer. Exact SGS scalar variance: solid line. Dotted lines are the first to fifth order approximations, the third order being distinguished by a dash-dotted line. Variances are non-dimensionalized by the exact value at the center of the mixing layer.

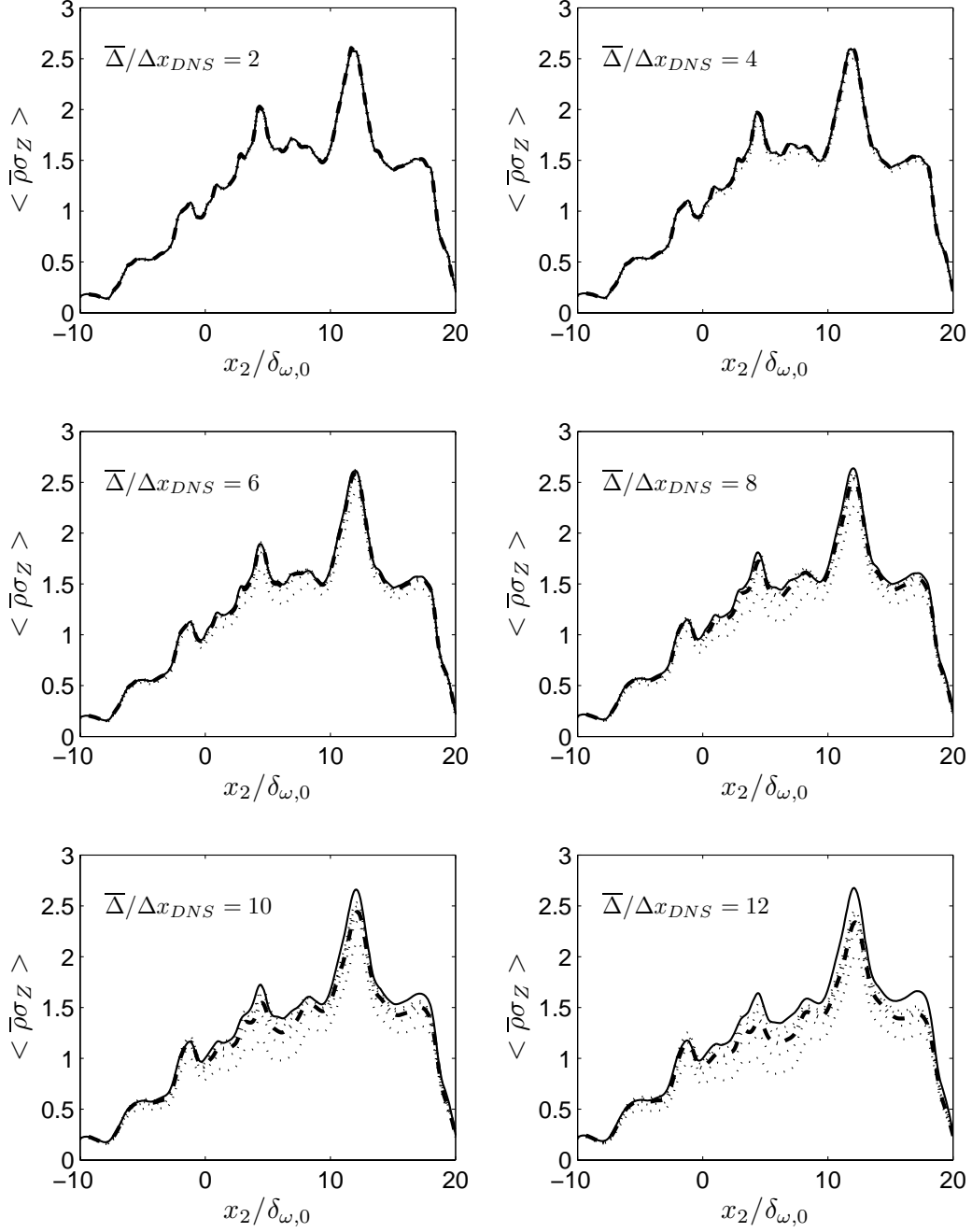


FIG. 15: Predictions of the Favre SGS scalar variance using ADM applied to conservative quantities. Several orders of approximation are shown for different filter widths at t_{tr}^* for the OHe600 mixing layer. Exact SGS scalar variance: solid line. Dotted lines are the first to fifth order approximations, the third order being distinguished by a dash-dotted line. Variances are non-dimensionalized by the exact value at the center of the mixing layer.

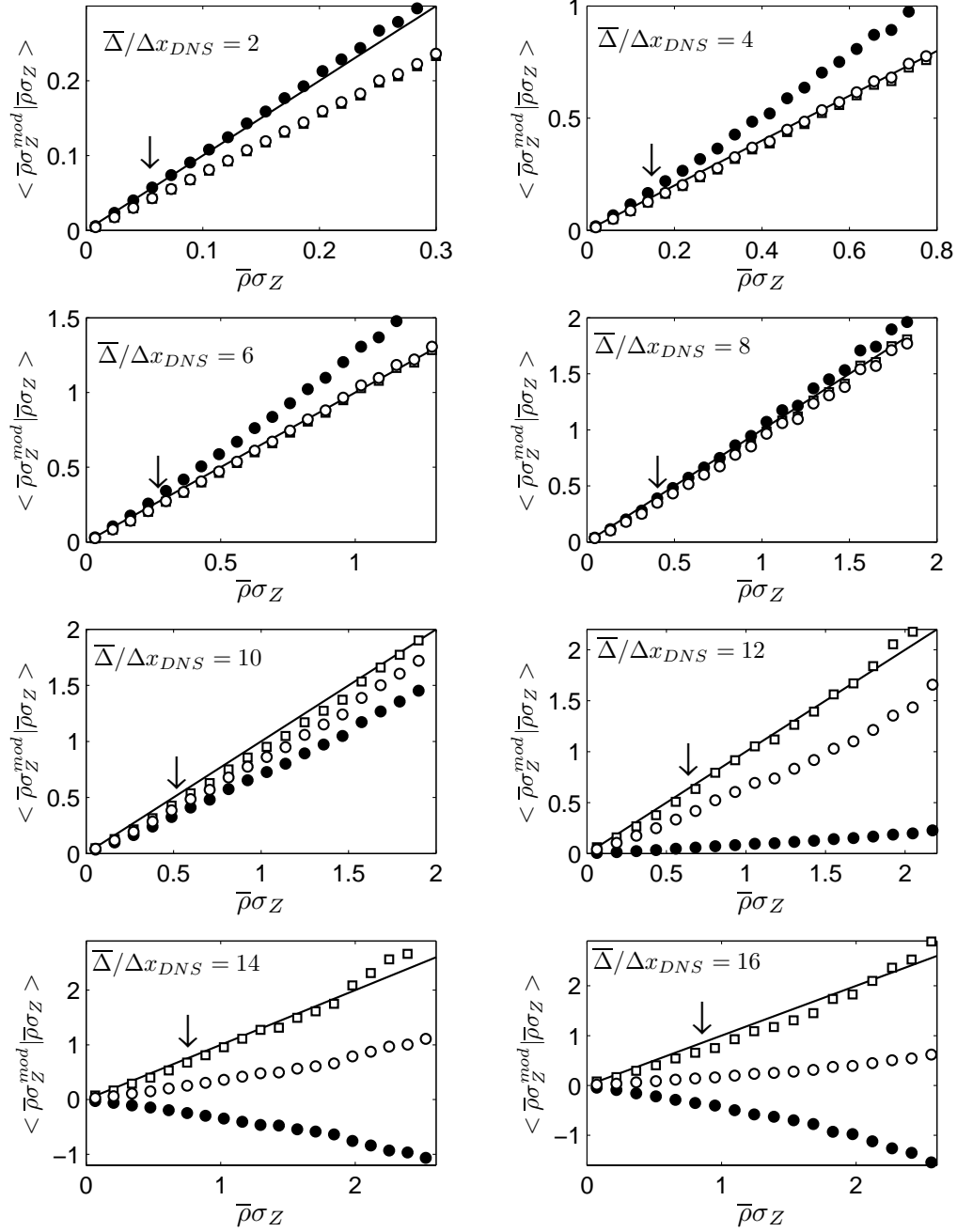


FIG. 16: Planar averages of modeled SGS scalar variances conditioned on the exact ones, evaluated using the filtered HN600 DNS at t_{tr}^* , over the plane $x_2/\delta_{\omega,0} = 0.44$. Coefficients are computed using the new model (Eq.(47)) (squares), and the classical model (Eq.(46)) with either $\hat{\Delta}^2 = \hat{\Delta}^2 + \overline{\Delta}^2$ (empty circles) or $\hat{\Delta} = \hat{\Delta}$ (filled circles). The arrow indicates the mean quantity $\langle \bar{\rho}\sigma_Z \rangle$.

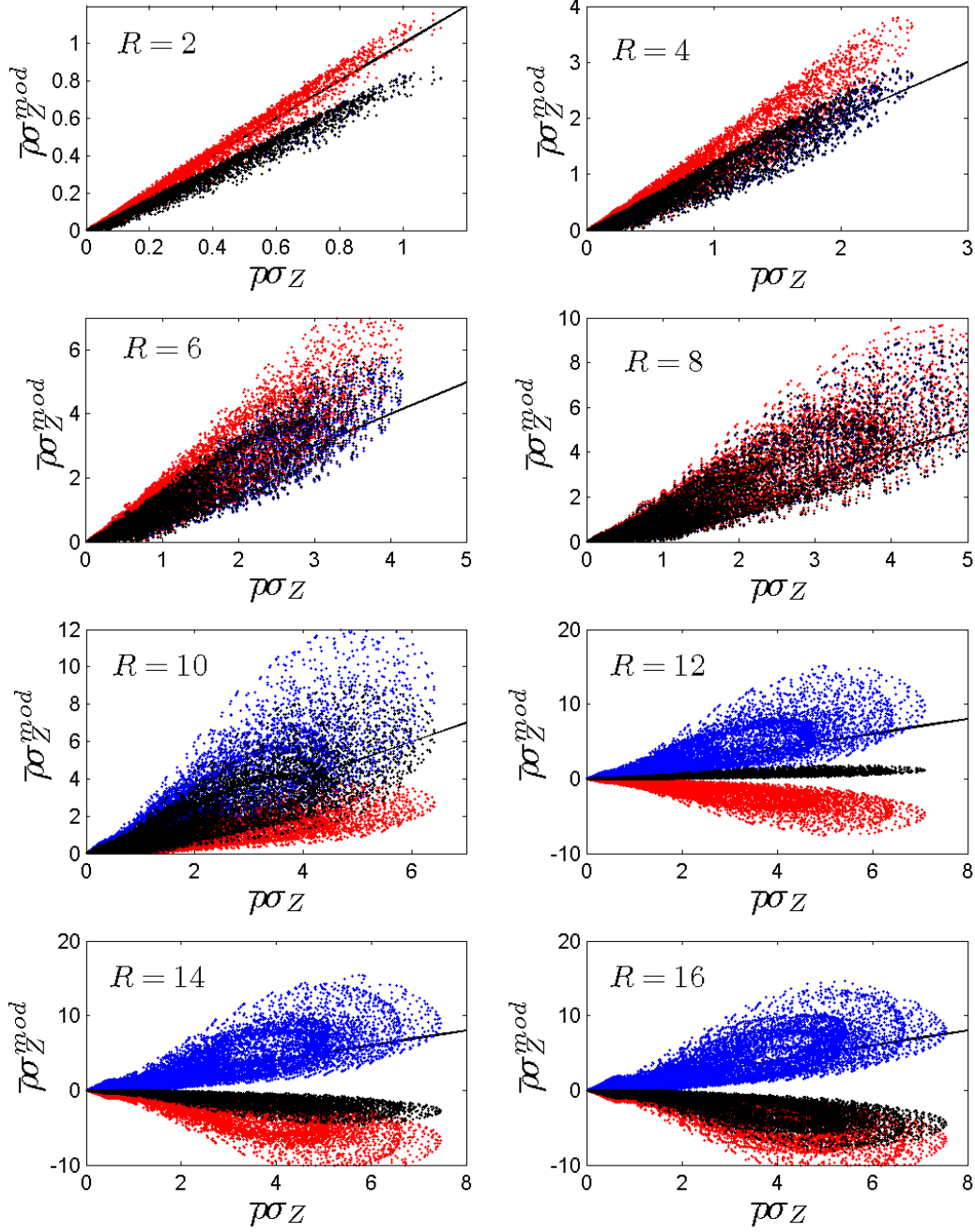


FIG. 17: Scatter plot of modeled against exact SGS scalar variance evaluated using the filtered HN600 DNS at t_{tr}^* , over the plane $x_2/\delta_{\omega,0} = 5.11$. Coefficients are computed using the new model (Eq.(47)) (blue symbols), and the classical model (Eq.(46)) with either $\widehat{\overline{\Delta}}^2 = \widehat{\Delta}^2 + \overline{\Delta}^2$ (black symbols) or $\widehat{\overline{\Delta}} = \widehat{\Delta}$ (red symbols). $R \equiv \overline{\Delta}/\Delta x_{DNS}$.

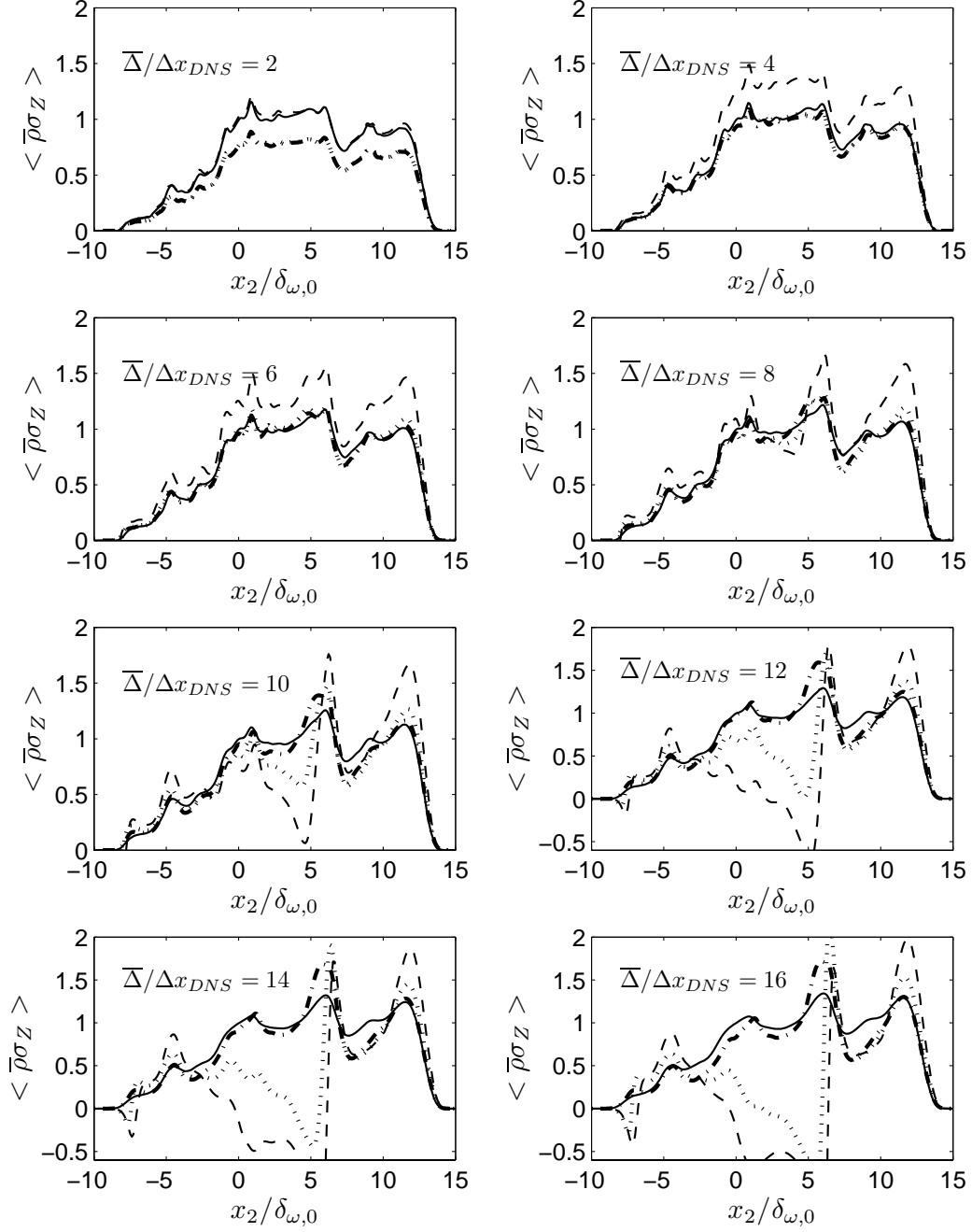


FIG. 18: Profiles of modeled and exact SGS scalar variances, evaluated using the filtered HN600 DNS at t_{tr}^* . Exact values: solid line. New model: dash-dotted line. Classical model using $\widehat{\bar{\Delta}}^2 = \widehat{\Delta}^2 + \bar{\Delta}^2$: dotted line. Classical model using $\widehat{\bar{\Delta}} = \widehat{\Delta}$: dashed line. Variances are non-dimensionalized by the exact value at the center of the mixing layer.

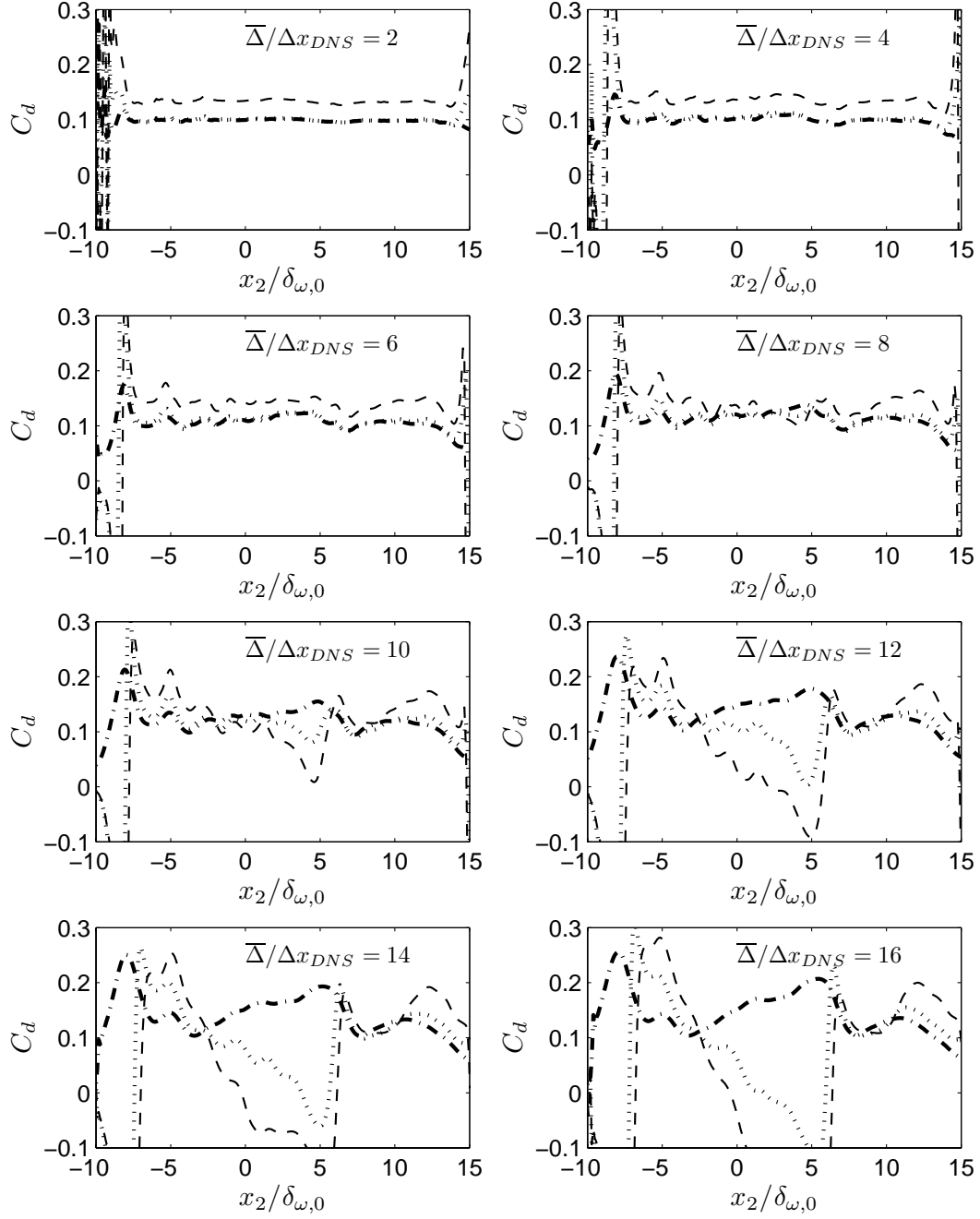


FIG. 19: Model coefficients C_d evaluated using the filtered HN600 DNS at t_{tr}^* . New model: dash-dotted line. Classical model using with $\widehat{\Delta}^2 = \widehat{\Delta}^2 + \overline{\Delta}^2$: dotted line. Classical model using $\widehat{\Delta} = \overline{\Delta}$: dashed line.

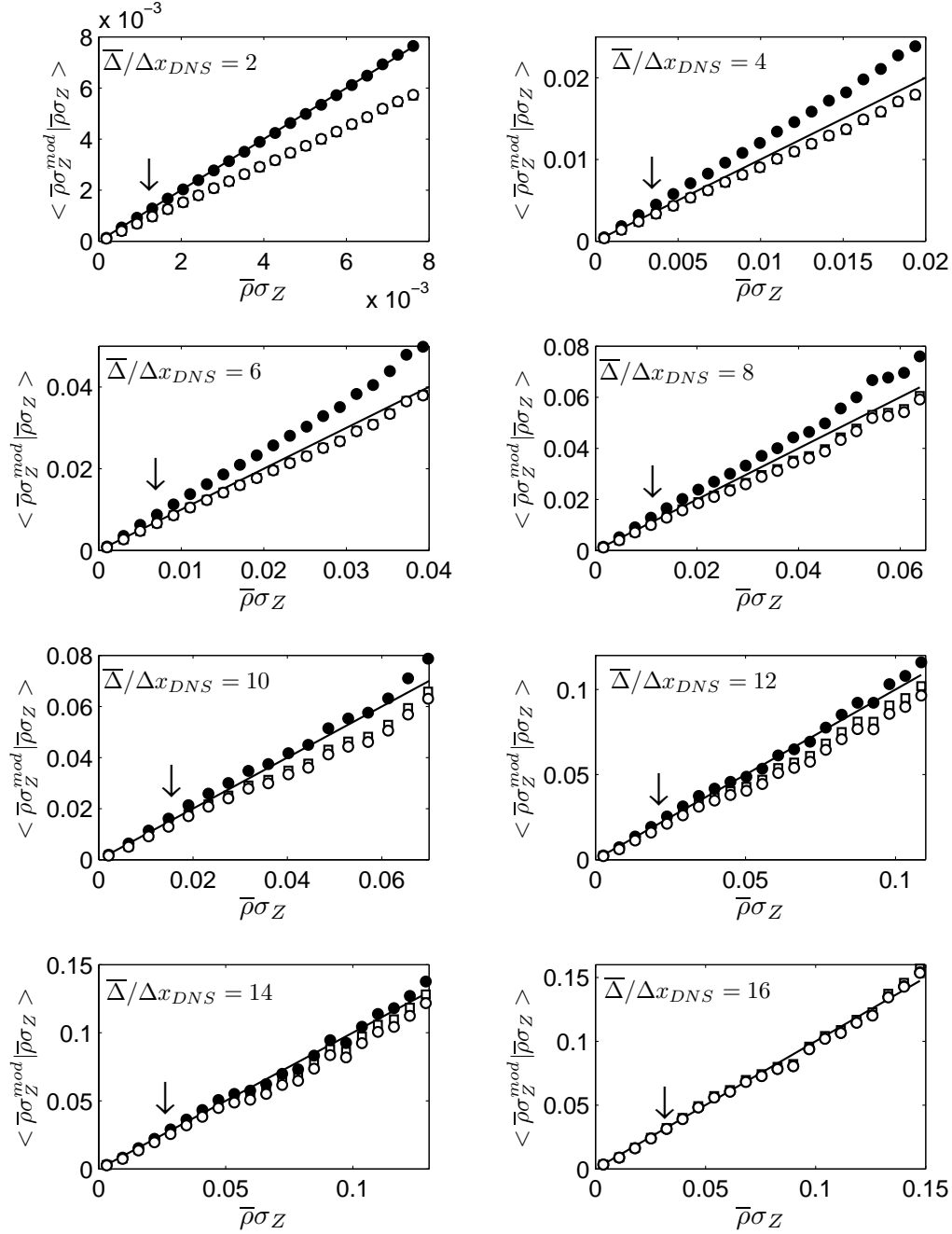


FIG. 20: Planar averages of modeled SGS scalar variances conditioned on the exact ones evaluated using the filtered OH750 DNS at t_{tr}^* over the plane $x_2/\delta_{\omega,0} = 0.44$. Coefficients are computed using the new model (Eq.(47)) (squares) and the classical model (Eq.(46)) with either $\hat{\bar{\Delta}}^2 = \hat{\Delta}^2 + \bar{\Delta}^2$ (empty circles) or $\hat{\bar{\Delta}} = \hat{\Delta}$ (filled circles). The arrow indicates the mean quantity $\langle \bar{\rho} \sigma_Z \rangle$.

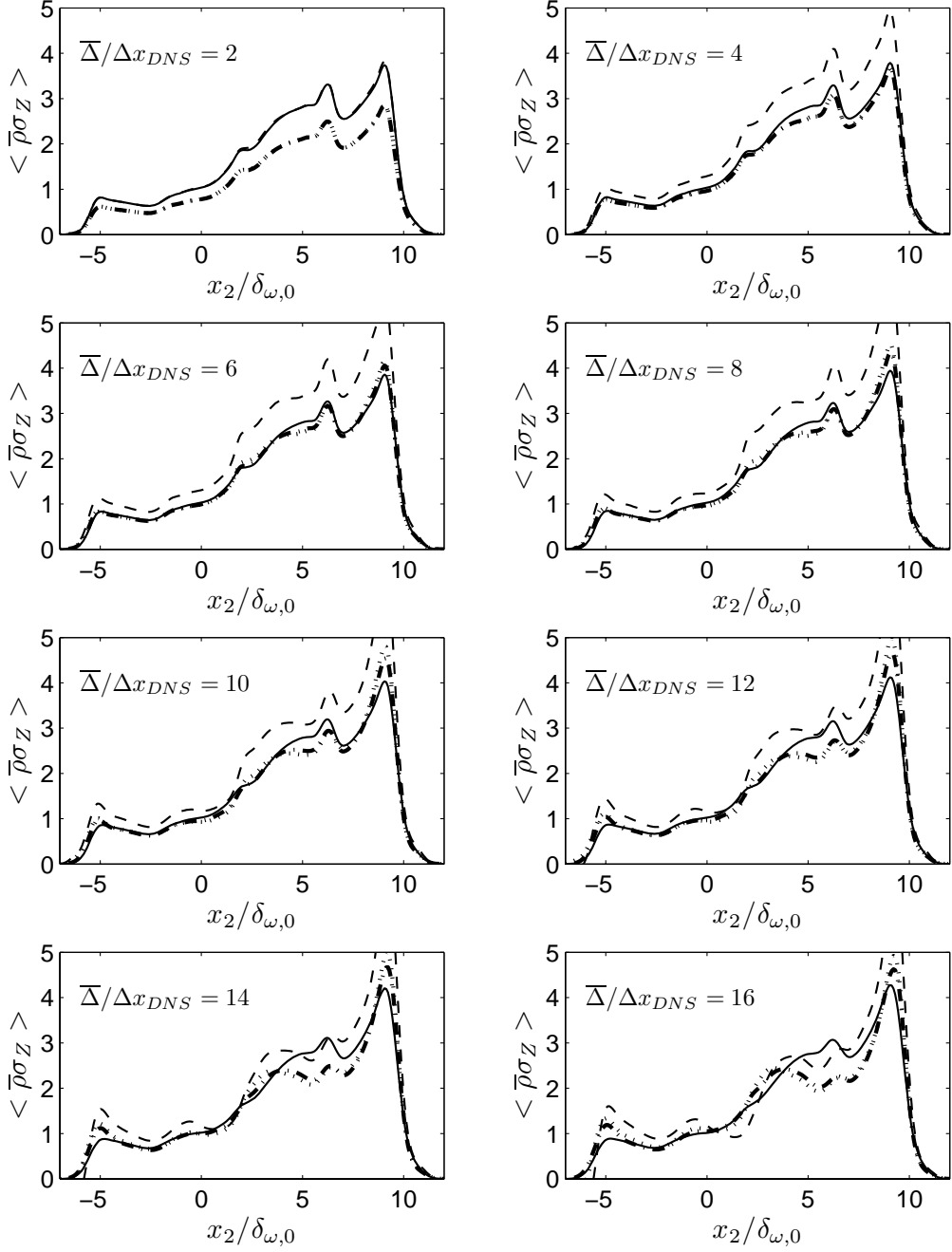


FIG. 21: Profiles of modeled and exact SGS scalar variances evaluated using the filtered OH750 DNS at t_{tr}^* . Exact values: solid line. New model: dash-dotted line. Classical model using $\widehat{\bar{\Delta}}^2 = \widehat{\Delta}^2 + \bar{\Delta}^2$: dotted line. Classical model using $\widehat{\bar{\Delta}} = \widehat{\Delta}$: dashed line. Variances are non-dimensionalized by the exact value at the center of the mixing layer.

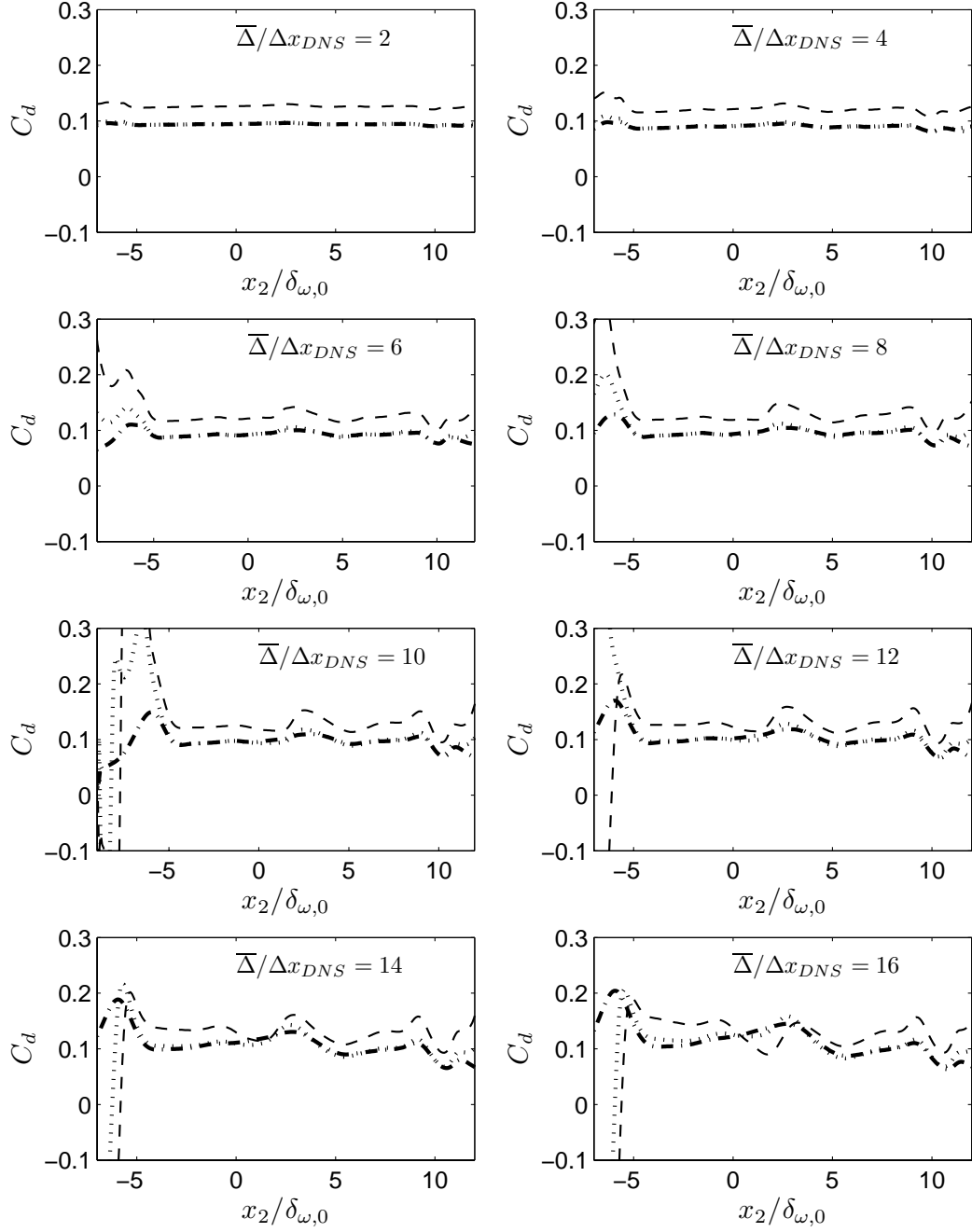


FIG. 22: Model coefficients C_d evaluated using the filtered OH750 DNS at t_{tr}^* . New model: dash-dotted line. Classical model using $\widehat{\Delta}^2 = \widehat{\Delta}^2 + \overline{\Delta}^2$: dotted line. Classical model using $\widehat{\Delta} = \widehat{\Delta}$: dashed line.

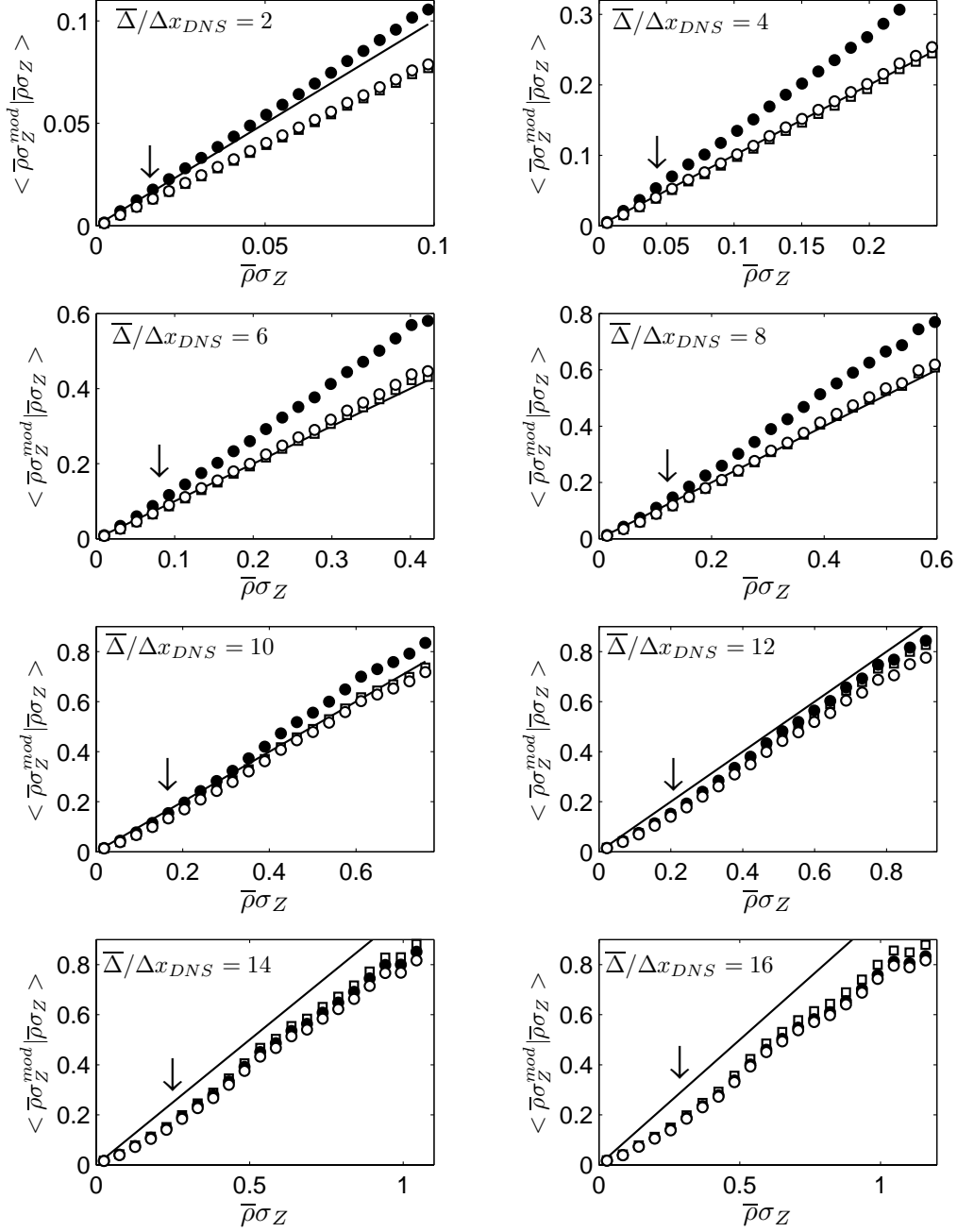


FIG. 23: Planar averages of modeled SGS scalar variances conditional to exact ones evaluated using the OHe600 DNS at t_{tr}^* over the plane $x_2/\delta_{\omega,0} = 0.44$. Coefficients are computed using the new model (Eq.(47)) (squares) and the classical model (Eq.(46)) with either $\hat{\bar{\Delta}}^2 = \hat{\Delta}^2 + \bar{\Delta}^2$ (empty circles) or $\hat{\bar{\Delta}} = \hat{\Delta}$ (filled circles). The arrow indicates the mean quantity $\langle \bar{\rho}\sigma_Z \rangle$.

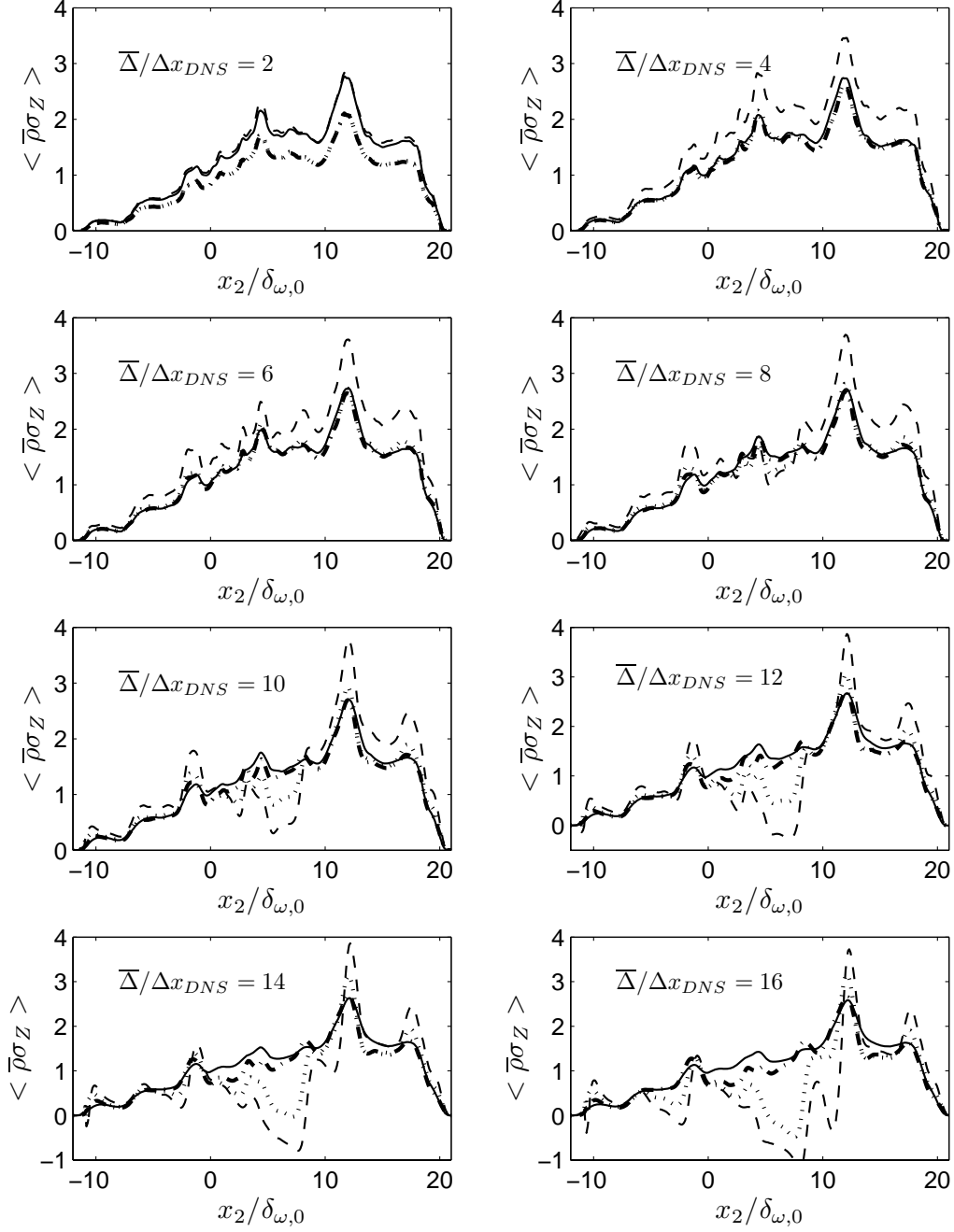


FIG. 24: Profiles of modeled and exact SGS scalar variances evaluated using the filtered OHe600 DNS at t_{tr}^* . Exact values: solid line. New model: dash-dotted line. Classical model using $\widehat{\bar{\Delta}}^2 = \widehat{\Delta}^2 + \bar{\Delta}^2$: dotted line. Classical model using $\widehat{\bar{\Delta}} = \widehat{\Delta}$: dashed line. Variances are non-dimensionalized by the exact value at the center of the mixing layer.

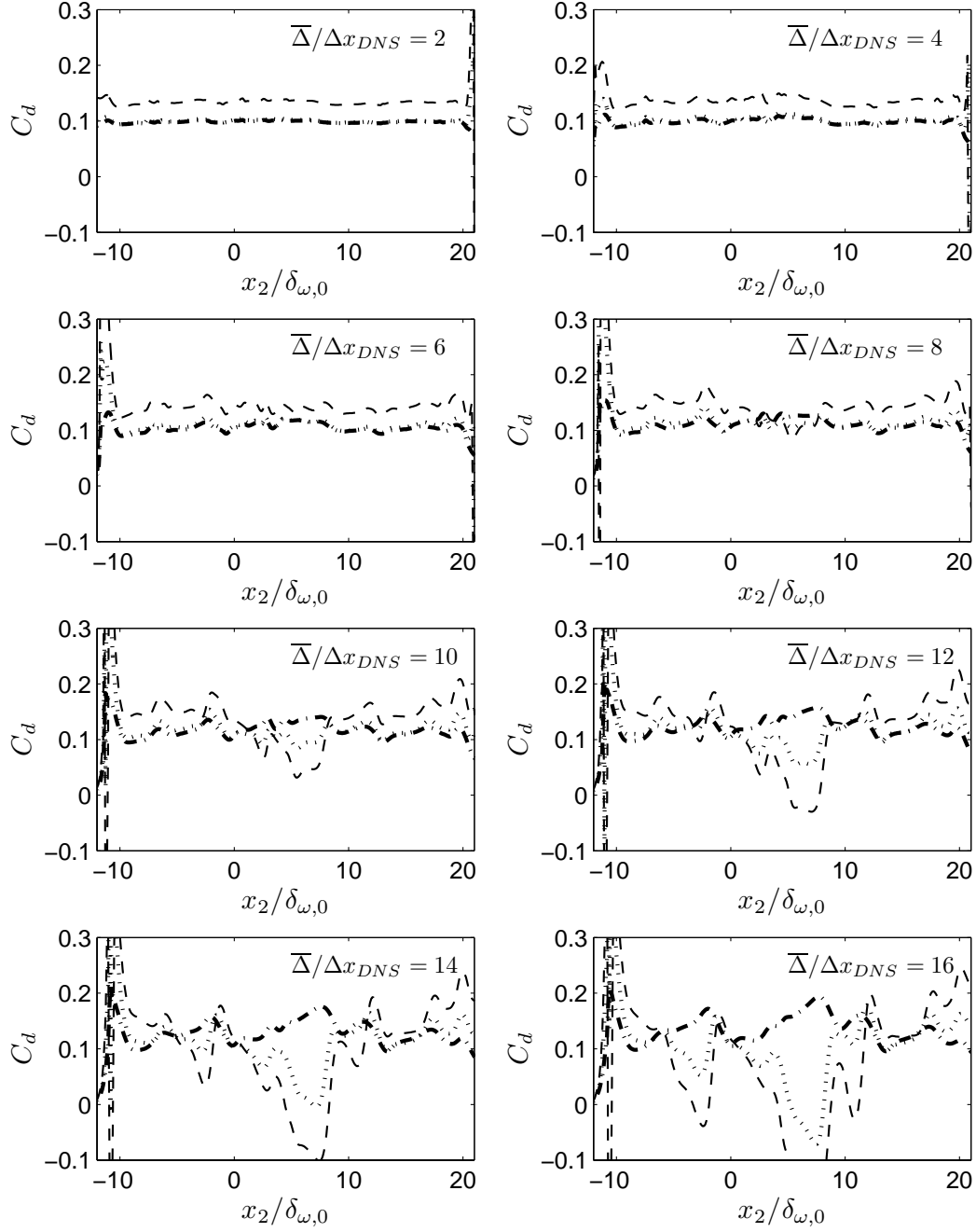


FIG. 25: Model coefficients C_d evaluated by using the filtered OHe600 DNS at t_{tr}^* . New model: dash-dotted line. Classical model using $\widehat{\Delta}^2 = \widehat{\Delta}^2 + \overline{\Delta}^2$: dotted line. Classical model using $\widehat{\Delta} = \overline{\Delta}$: dashed line.

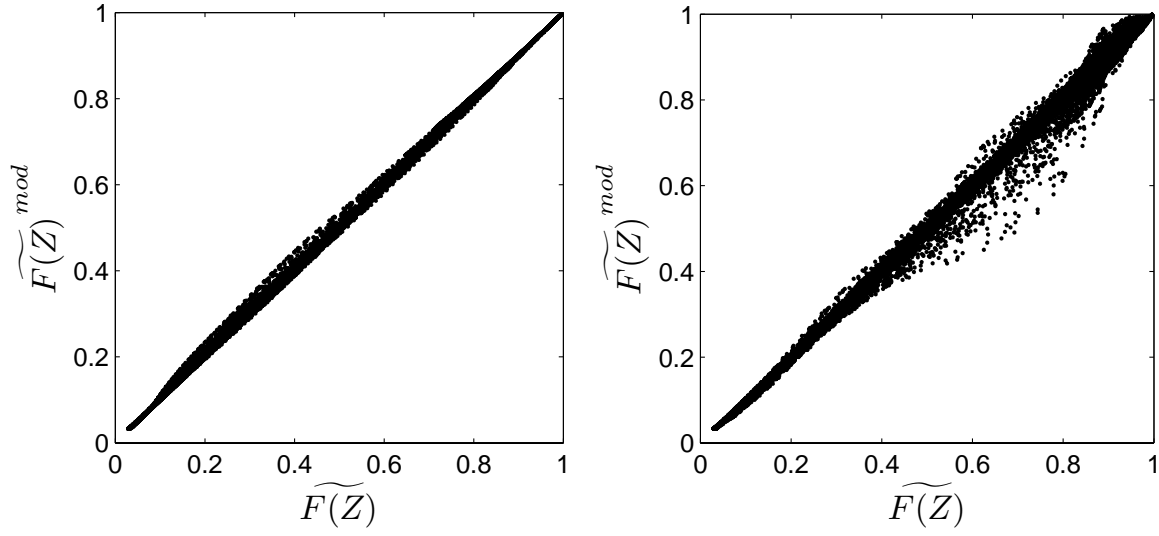


FIG. 26: Scatter plot of the modeled function $\widetilde{F(Z)}^{mod}$ versus the exact quantity $\widetilde{F(Z)}$ computed over the plane $x_2/\delta_{\omega,0} = 0.44$. The evaluation is made for the filtered HN600 DNS at t_{tr}^* , using the scalar variance σ_Z modeled employing a third-order ADM (left), and the new dynamic model (right). $\overline{\Delta}/\Delta x_{DNS} = 8$.

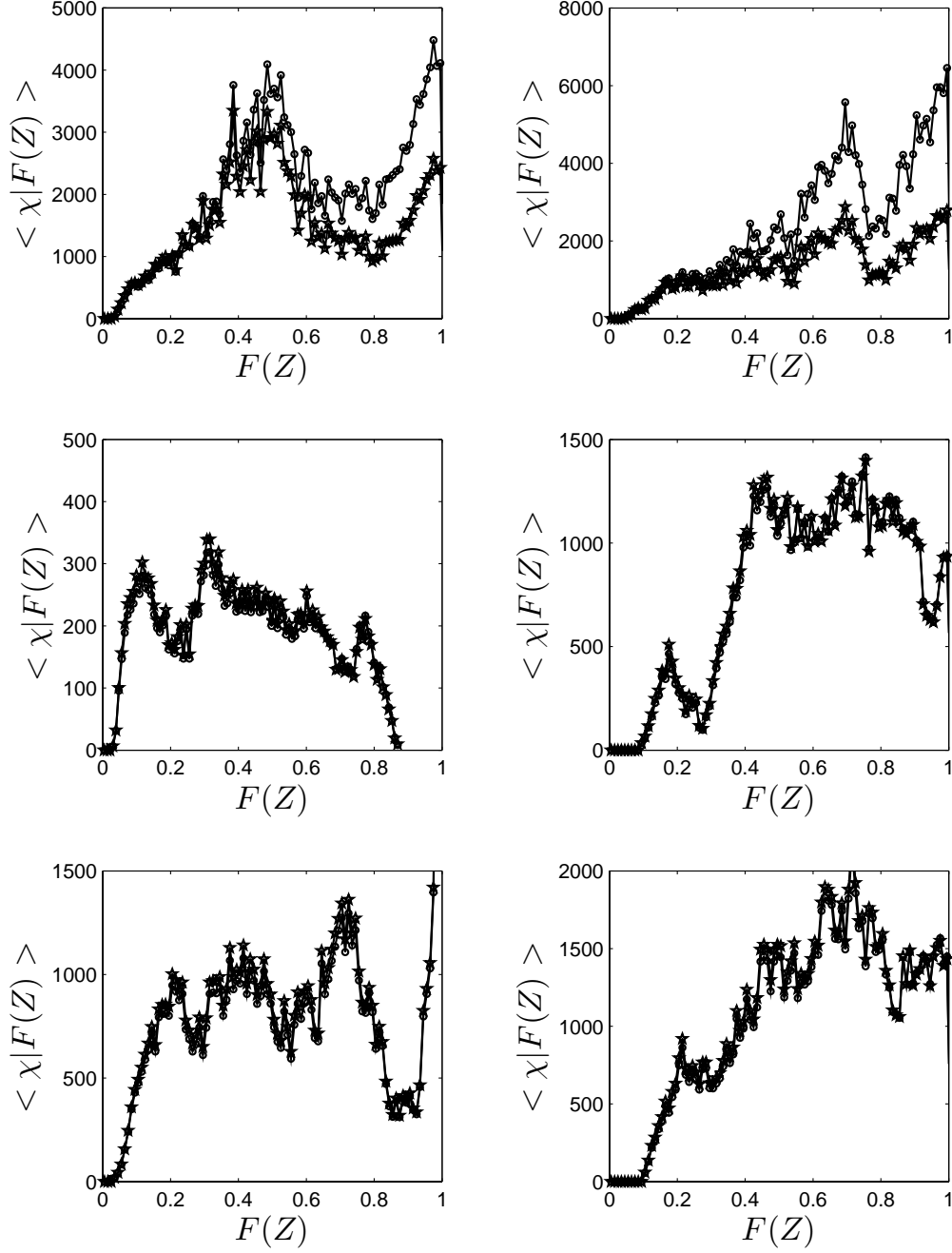


FIG. 27: Conditional average of χ_T (circles) and χ_T (stars) on $F(Z)$ given by Eq. (50). The computations used the HN600 DNS at t_{tr}^* over planes corresponding to $x_2/\delta_{\omega,0} = 0.44$ (left) and $x_2/\delta_{\omega,0} = 5.11$ (right). $\overline{\Delta}/\Delta x_{DNS} = 8$.

Thermomechanical Response of a Reactive Gas to Extremely Rapid Transient, Spatially Distributed Energy Addition: An Asymptotic Formulation

D. R. Kassoy¹, K. Wojciechowski²

Abstract

An asymptotic formulation developed for inert gas heating ((Kassoy, DR., 2010, J. Eng.Math, **68**, 249-262). is extended to describe the thermomechanical response of a reactive gas to a localized, exothermic chemical reaction. The model is developed for a subcritical, perfect gas with one-step, high activation energy exothermic kinetics. A finite volume of gas (the hot spot) is heated initially by an external source on a time-scale short compared to the acoustic time of the region, with the objective of raising the local temperature sufficiently to ignite a robust rapid reaction. The analysis defines physical and chemical conditions compatible with nearly inertially-confined heating. Numerical solutions to the describing equations show that a spatially distributed reaction wave appears spontaneously in the hottest portion of the hot spot, propagates initially through the relatively slowly moving fluid at a supersonic speed (relative to the hot gas speed of sound) and then decelerates significantly and steepens considerably as the front nears the much colder boundary of the hot spot. The configuration evolves toward a discontinuous front separating hot, high-pressure, burned gas on one side from cold, low pressure reactant on the other side. During the relevant heating time scale the entire process occurs in a nearly incompressible medium, leading to an ephemeral, isolated, burned out, hot, high pressure spot embedded in a cold unreacted, lower pressure gas. The large pressure gradient at the front induces a local positive radial fluid velocity. Fluid expelled from the hot spot boundary acts as source of mechanical disturbances propagating into the neighboring cold reactant. The amplitude of those disturbances depends upon the energy addition level during the reactive phase of the hot spot. The formulation also identifies conditions compatible with a fully compressible heat addition process, characterized by a very significant internal expansion Mach number, likely the source of reactive blast wave generation in the environmental reactant.

¹ Professor Emeritus, Mechanical Engineering Department, University of Colorado, Boulder, CO 80309-0427, USA david.kassoy@colorado.edu

² Graduate Student, Mathematics, University of Colorado, Denver, CO

1. Introduction

Oppenheim and Soloukhin [1] state that “Gasdynamics of explosions is best defined as the science dealing with the interrelationship between energy transfer occurring at a high rate in a compressible medium and the concomitant motion set up in the medium.” This perceptive insight challenges the modeler to relate quantitatively transient, spatially resolved energy deposition into a hot spot to changes in the thermodynamic state, and the induced fluid motion, as well as to predict the acoustic and/or gasdynamic disturbances generated in the unheated gaseous environment beyond the hot spot boundary.

An initial step toward developing a comprehensive thermomechanical theory for hot spots has been developed by Kassoy [2]. An external source provides spatially distributed, transient heat addition to a finite volume of inert gas **on a time scale short compared to the acoustic time of the heated region**. Asymptotic methods are used to derive reduced equation systems that describe hot spot evolution resulting from a wide range of energy addition. The results demonstrate that nearly-inertially confined heat addition occurs within the hot spot if the amplitude of energy is less than a critical value. This type of nearly constant volume heating is characterized by a synchronized increase in spatially distributed temperature and pressure, very small changes in density and a tiny internal expansion Mach number. Hot gas expelled from the volume at a locally small Mach number (the “piston” effect [3]) during the heating process generates only acoustics in the neighboring cold gas (the far-field). Sufficiently large energy addition leads to a fully compressible heat addition process. Much larger “piston” Mach numbers are the sources of far-field shock and blast wave propagation. Extension of the theoretical framework to reactive gases and other time scales is the subject of the present work.

Localized hot spots are common in a wide range of reactive gasdynamic processes, most notably detonation initiation [1]. One class of hot spot arises from relatively rapid, localized

thermal energy deposition from an external source into a volume of reactive gas (e.g., laser or spark). Another, the “reaction center” [1] arises spontaneously during the evolution to detonation. The modeling and experimental literature on the subject is extensive, and is referred to within the limited number of references cited in this work.

Sufficiently fast and large energy addition can facilitate a direct initiation. Clarke, Kassoy and Riley [4] and Clarke, Kassoy Maharzi, Riley and Vasantha [5] model detonation initiation following **spatially-resolved transient energy deposition** from a planar boundary via conduction into an adjacent reactive gas in a semi-infinite domain. The Navier-Stokes equations are integrated numerically to reveal a quantitative time-history of spatially resolved reactive gasdynamic processes that lead to planar detonation formation. The authors recognize that “...direct initiation of detonation requires sufficient power input to first of all generate a suitably strong precursor shockwave, which then becomes the trigger to switch on vigorous chemical activity in its wake. The hall mark of this vigor is its capacity to exploit the inertia of the fluid by raising local pressures and temperatures, with little diminution in local density; the pressure waves so formed propagate and increase precursor shock strength which therefore lifts the overall density levels, as well as those of pressure and temperature. All of these processes interlock in a continuously accelerated sequence that progresses towards a steady state....ZND detonation.”

Mazaheri [6] and Eckert, Quirk and Shepherd [7,8], model planar and spherical detonation initiation, respectively, initiated by blast waves subsequent to **instantaneous deposition of energy at a plane or a point**. Energy deposition criteria are used to distinguish between sustained and failed detonations. Computational modeling results demonstrate that blast wave propagation through unreacted gas mixture leads to the formation of localized regions of rapid

chemical heat release (thermal explosions) characterized by relatively high temperature and pressure, similar to those found in Refs. 9-11. These hot spots are the subsequent sources of compression waves that may run up to and strengthen the blast wave front enough to generate and sustain a classical detonation (shock coupled to a reaction zone).

Sileem, Kassoy and Hayashi [12], (SKH), Kassoy, Keuhn, Nabity and Clarke [13,14], (KKNC), Regele, Kassoy and Vasilyev [15] model the reactive gas response to relatively smaller **spatially distributed, transient energy deposition into a finite target volume**. They describe the sequence of reactive gasdynamic events occurring in a deflagration to detonation transition (DDT), including the initially heated volume and the spontaneous appearance of local hot spots far from the original energy deposition. Computational results, based on MacCormack numerical methods with fixed grids [12-14] and the Adaptive Wavelet Collocation Method [15], resolve hot spot transients facilitating the detonation initiation process.

Gu *et al.* [16] use computational solutions to the Euler equations with multistep kinetics relevant to H₂-CO-Air and H₂-Air mixtures to identify five distinct modes of reaction front propagation arising from a **preexisting local hot spot**. They find that evolution of the detonative mode depends on the temperature distribution properties of the hot spot and “...the ratio of the hotspot acoustic time to the heat release rate excitation time...”

Detonation initiation associated with reflected shocks and shock flame interactions, studied intensively by Oran and co-workers beginning in the 1980's, and reviewed by Oran and Gamezo [17] is also affected substantially by hot spot dynamics. In fact, nearly all studies of detonation initiation contain qualitative descriptions of the role played by hot spots in the development of detonations. Since the early experimental observation by Oppenheim [18] of an “explosion in an explosion” (reaction center) it has been argued that hot spots are local sources of compression

waves that strengthen existing lead shocks to promote the existence of coupled reaction zones. That argument depends on the simultaneous local increase in temperature and pressure caused by localized chemical heat release in a nearly inertially confined fluid volume (constant volume heating) characterized by a minimal change in density.

Zeldovich and co-workers [19,20] articulate an intuitive theory for the initiation and “...(spontaneous) propagation of intense chemical reaction...” arising from a **pre-existing hot spot with a localized linear temperature gradient**. The authors describe a model for constant volume thermal explosion phenomena (“...in each particle of the substance, thermal explosion occurs independently.”). The chemico-physical conditions necessary for this type of reaction wave initiation and propagation are not articulated.

Many researchers have endeavored to rationalize the Zeldovich model concept. Jackson, Kapila and Stewart [9], Short [10,11], Kapila, Shwendeman, Quirk and Hawa [21], have used a combination of asymptotic and computational methodologies to model the evolution of spatially distributed thermal explosions arising from a **pre-existing localized linear temperature gradient** in a rigid container. Asymptotic results describe spatially distributed, transient chemical heat release during a relatively lengthy induction period, followed by much shorter periods of extremely rapid energy deposition (the explosion) into a relatively tiny spatial volume. Comprehensive asymptotic and numerical results in Ref. 21 provide an excellent assessment of the impact of the temperature gradient slope on the combustion wave evolution. Many of the observed effects can be attributed to differences in the local chemical heat release time and the local acoustic time, exploited formally in Ref. 2. These confined hot spot theories [9-11,21] describe the thermomechanical properties of the chemically heated gas, but are not formulated to describe the impact of focused rapid heat release on gases external to the heated region.

The current analysis extends the asymptotic methodology in Ref. 2 to a reactive gas with one step, high activation energy Arrhenius kinetics. Initially, an external source provides thermal power to a finite volume of gas on a time scale short compared to the acoustic time of the heat region. The resulting near-constant volume heat addition causes a relatively modest temperature increase, insufficient to initiate the high activation energy reaction. Continued power deposition on a slightly longer time scale, but shorter than the acoustic time of the volume, leads to a temperature increase large enough to facilitate a strong reaction. This strategy obviates the need for a more traditional induction period thermal explosion analysis. The reaction evolution and subsequent front propagation occurs in a near-constant volume process as long as the energy addition is limited. When the energy added reaches a specific critical level, inertial confinement fails and the entire reaction event is described by fully compressible equations. This result provides quantitative chemico-physical conditions for the validity of the Zeldovich spontaneous propagation model.

2. Modeling Concepts

A finite spheroidal volume V' of spatially uniform reactive gas mixture (p'_0, T'_0, ρ'_0) with an average radius R' , is heated by absorbing thermal power P' (J/kg.) from an external source on a heating scale t'_H . How can the modeler quantify the response of the gas volume (the near-field) to the energy deposition, $E' = P't'_H$ (J/kg.)? What are the magnitudes of the induced motion and thermodynamic variable changes? How does the near-field response affect the unheated gaseous environment (the far-field)? Thermo-mechanical concepts can be employed to address these questions. Kassoy [2] has used asymptotic methodologies to describe the consequences of energy deposition, $E' \gg e'_0 = C'_v T'_0$ (the initial internal energy) into a finite volume of **inert gas**

when $\varepsilon \equiv t'_H/t'_A \ll 1$, where $t'_A = R'/a'_0$ is the characteristic acoustic time and a'_0 is the speed of sound based on the initial spot temperature T'_0 . During this brief period of heating, an acoustic disturbance can propagate only a small distance compared to the spot dimension R' . When E' is less than a specific critical value the heating process is nearly constant volume (inertial confinement), characterized by asymptotically small values of density variation along with a large, lowest order, constant volume temperature increase as well as a concomitant large rise in pressure. During this period of near-inertial confinement, the thermo-mechanically induced near-field gas Mach number (based on the local hot speed of sound, $a' = \sqrt{\gamma R' T'}$ is very small, implying that the preponderance of the absorbed thermal power is used to enhance the internal energy of the gas. Very little thermal power is converted to kinetic energy. A limited range of E' -values exist for which the Mach number of the gas expelled from the edge of the volume is asymptotically small. The “piston” effect of the expansion generates only small amplitude acoustic waves in the far-field. Larger values of E' , but less than the aforementioned critical value, are associated with stronger “piston” effects that are the source of more robust gasdynamic disturbances in the far-field, similar that described in [22].

When E' reaches the critical magnitude, the heat addition process is determined to be completely compressible, characterized by large increases in temperature and pressure as well as an $O(1)$ or larger internal Mach number. There is significant conversion of thermal to kinetic energy in the near-field. The relatively violent expansion process is the source of strong blast waves in the far-field [23].

The application of these thermomechanical concepts to a reactive gas is affected by the highly nonlinear temperature dependence of exothermic chemical reactions, particularly for high activation energy kinetics. As a result there will be consequential differences in the outcomes

arising from rapid chemical heat release. The questions raised in the first paragraph of this section remain germane for the reactive case. The answers may help to understand how **transient, spatially distributed** heat release in a reactive flow can be the source of acoustic and gas dynamic disturbances (e.g. solid and liquid rocket engine dynamics, internal combustion engines).

The conceptual model description provides physically-based insights into the thermomechanics of gases affected by localized, relatively rapid, transient energy addition. The mathematical model used in Ref. 2 provides quantitative assessments of the physics, a systematic scheme based on formal asymptotic methods, including a complete understanding of the model limitations. A well-defined thermomechanical analysis for a reacting flow is described in the next section.

2.1 Mathematical Model

Imagine thermal power deposition into a spheroidal volume of characteristic dimension R' during a heating time period t'_H such that $t'_{COLL} \ll t'_H \ll t'_A = R'/a'_0$ where t'_{COLL} is the collision time for the reactive gas mixture. The gas is initially at rest with density, pressure, and temperature ρ'_0 , P'_0 and T'_0 , respectively, while the ambient speed of sound, $a'_0 = (\gamma R' T'_0)^{1/2}$. A simple one-step high activation Arrhenius exothermic reaction, $R \rightarrow P$, is assumed to describe the chemistry.

The mathematical model is based on the equations for a compressible perfect reactive gas with transport effects included. Conservation and state equations in three spatial dimensions (r', θ, ϕ) and time (t') can be written in the nondimensional form:

$$\rho_\tau + \varepsilon \nabla \cdot \rho \underline{u} = 0 \quad (1)$$

$$\rho [\underline{u}_\tau + \varepsilon \underline{u} \cdot \nabla \underline{u}] = -\varepsilon \frac{\nabla p}{\gamma} + \beta \underline{V} \quad (2)$$

$$\frac{\rho}{(\gamma-1)} [T_\tau + \varepsilon \underline{u} \cdot \nabla T] = -\varepsilon p \nabla \cdot \underline{u} + \gamma \Delta H_e \rho \dot{Q} + \beta \left[\frac{\gamma}{(\gamma-1)} \frac{C}{\text{Pr}} + \gamma \Phi \right] \quad (3)$$

$$Y_\tau + \varepsilon \underline{u} \cdot \nabla Y = -\delta Y e^{-T_A/T} + \frac{\beta}{\text{Sc}} \frac{1}{\rho} D, \quad p = \rho T \quad (4a,b)$$

where the three-dimensional vector operators are in spherical coordinates.

The equations can be nondimensionalized initially with variables (unprimed) defined by

$$(\rho, p, T) = (\rho'/\rho'_0, p'/p'_0, T'/T'_0) \quad , \quad \underline{u} = \underline{u}'/a'_0 \quad (5a,b)$$

$$\underline{x} = \underline{x}'/R' \quad , \quad \tau = t'/t'_H \quad (6a,b)$$

$$\underline{V} = \underline{V}' / \frac{\mu'_0 a'_0}{R'^2} \quad , \quad C = C' / \frac{k'_0 T'_0}{R'^2} \quad , \quad \Phi = \Phi' / \frac{\mu'_0 a'^2_0}{R'^2} \quad , \quad D = D' / \frac{\mathcal{D}'_0}{R'^2} \quad (7a,b,c,d)$$

$$\dot{Q} = \dot{Q}_e(r, \theta, \varphi, \tau) + \Omega Y e^{-T_A/T} \quad , \quad T_A = T'_A/T'_0 \quad , \quad T'_A = E'_0/R'_g \quad (8a,b,c)$$

$$\varepsilon = t'_H/t'_A \quad , \quad \beta = t'_H/t'_V \quad , \quad \delta = t'_H B' \quad (9a,b,c)$$

$$\Omega = \frac{\Delta H_{ch} \delta}{\Delta H_e} \quad , \quad \Delta H_{ch} = \Delta H'_{ch}/a'^2_0 \quad , \quad \Delta H_e = \Delta H'_e/a'^2_0 \quad (10a,b,c)$$

where \underline{V} , C , Φ and D are symbols representing the dimensionless viscous vector, scalar conduction, scalar viscous dissipation and scalar mass diffusion, respectively. In addition, μ'_0 , k'_0 and \mathcal{D}'_0 are the characteristic viscosity, conductivity and diffusivity at T'_0 , respectively.

Equation 8a contains the external power source $\dot{Q}_e = \dot{Q}'_e / (\Delta H'_e/t'_H)$ where \dot{Q}'_e is the dimensional power source and $\Delta H'_e/t'_H$ is the characteristic dimensional power deposition, composed of the characteristic energy $\Delta H'_e$ added on the heating time scale t'_H . In addition, Ω is a

nondimensional pre-exponential factor defined in (10a), where ΔH_{ch} is the nondimensional chemical heat of reaction, measured with respect to $a_0'^2 = \gamma(\gamma-1)e_0'$, a surrogate for the initial internal energy, e_0' at T_0' and δ is defined in (9c) as the ratio of the heating time to the inverse pre-exponential factor B'^{-1} , for a one-step reaction. Similarly, ΔH_e , in (10c), is the nondimensional externally added energy, also measured with respect to $a_0'^2$. Y is the mass concentration of fuel, initially distributed uniformly at 1. The nondimensional activation temperature T_A is defined in (8b) with respect to the initial temperature T_0' , where the dimensional activation temperature is defined in (8c) in terms of the dimensional activation energy E_0' and the universal gas constant R'_g . It is assumed that the characteristic heating time $t_H' \ll t_A' = R'/a_0'$ so that the parameter ε defined in (9a) is very small. It is noted from (9b) that the characteristic viscous time $t_v' = R'^2/\nu_0'$ is much larger than the heating time because $\beta = t_H'/t_v' = \varepsilon \left/ \frac{a_0' R'}{\nu_0'} \right.$ where the acoustic Reynolds number $a_0' R'/\nu_0'$ is large for $R' \gg O(10^{-8} m)$.

The Prandtl and Schmidt numbers as well as γ have standard definitions and are treated as $O(1)$ constants, relatively to the small parameter ε .

Equation (3) is written for a constant specific heat to provide a relatively elementary model. This assumption has the disadvantage of precluding activation of internal energy modes at high temperature. Limitations are discussed in Section 3.

The rest-state initial conditions are

$$\tau = 0 : \quad \rho = P = T = 1 \quad , \quad \underline{u} = 0 \quad , \quad \dot{Q}_e = 0 \quad (11)$$

In general, the spatially distributed, time-dependent external source function can be described by

$$\begin{aligned}\dot{Q}_e(r, \theta, \varphi, \tau) &\geq 0 \quad , \quad r \leq r_s(\theta, \varphi) \quad , \\ \dot{Q}_e(r, \theta, \varphi, \tau) &= 0 \quad , \quad r > r_s(\theta, \varphi) \quad ,\end{aligned}\tag{12}$$

where $r_s(\theta, \varphi) = r'_s(\theta, \varphi)/R'$ describes coordinates of the outer surface of the heated region. The volume beyond the spot surface is not heated by the source.

The nondimensional equations, (1)-(4), describe reactive flow dynamics for a wide range of length and time scales. Table 1 provides estimates for the acoustic t'_A and viscous t'_v times for several values of R' and the allowable range of heating time values t'_H , such that $t'_{COLL} \ll t'_H \ll t'_A$. The numerical values for t'_A are defined for a gas initially at $T'_0 = 300$ K and $p'_o = 1$ atm. These ambient values are associated with a mean free path $\lambda' = 5.3 \times 10^{-8}$ m, a collision time $t'_{COLL} = 1.6 \times 10^{-10}$ s and a characteristic kinematic viscosity $\nu'_0 = 1.64 \times 10^{-5}$ m²/s.

Asymptotic methods, based on the time-ratio limit $\varepsilon \rightarrow 0$, are used to obtain reduced equation systems for several phases of the heating process, reaction initiation, and the accompanying generation of gasdynamics waves. It is assumed that $Pr = O(1)$, $Sc = O(1)$, and that $\beta \rightarrow 0$ (see 7b) because the viscous diffusion time defined previously is typically orders of magnitude larger than the heating time. Finally, it is assumed that the activation temperature defined in (8b,c), $T_A = T_A(\varepsilon) \gg 1$, where the specific functional dependence is defined later in the analysis.

Table 1 – Characteristic values of the acoustic time t'_A and the viscous time t'_v and the allowable range of heating times t'_H for a range of characteristic spot dimensions R' when $T'_0 = 300\text{ K}$, $P'_0 = 1\text{ atm}$ and $\nu'_0 = 1.64 \times 10^{-5}\text{ m}^2\text{s}$

$R'(\text{m})$	$t'_A = R'/a'_0(\text{s})$	$t'_H(\text{s})$	$t'_v = R'^2/\nu'_0(\text{s})$
10^{-2}	3×10^{-5}	$\leq 10^{-6}$	6.1
10^{-3}	3×10^{-6}	$\leq 10^{-7}$	6.1×10^{-2}
10^{-4}	3×10^{-7}	$\leq 10^{-8}$	6.1×10^{-4}
10^{-5}	3×10^{-8}	$\leq 10^{-9}$	6.1×10^{-6}
10^{-6}	3×10^{-9}	t'_{COLL}	6.1×10^{-8}
λ'	t'_{COLL}	—	—

2.2 Inert Heating Period: $t' = O(t'_H)$

(a) Internal spot dynamics: $r \leq r_s(\theta, \varphi)$

The limiting forms of (1), (2) and (4a) for $\varepsilon \rightarrow 0$ and $T_A(\varepsilon) \rightarrow \infty$, $\rho_\tau = \mathbf{u}_\tau = Y_\tau = 0$ and the relevant initial conditions in (22) imply that $\mathbf{u}_0 = 0$ and $\rho_0 = y_0 = 1$, where the zero subscript represents the lowest order asymptotic approximation to each of the dependent variables. It follows from (4b) that $p_0 = T_0$ where the temperature distribution is described by the reduced version of (3) and the appropriate initial condition respectively;

$$\begin{aligned} \frac{\partial T_0}{\partial \tau} &= \gamma(\gamma - 1) \Delta H_e \dot{Q}_e(r, \theta, \varphi, \tau) \\ \tau = 0 ; T_0 &= 1 \end{aligned} \tag{13a,b}$$

Equation (13) describes constant volume heating due to energy deposition represented by \dot{Q}_e .

The characteristic changes in temperature, $\Delta T'/T'_0 = O(1)$ and pressure, $\Delta p'_0/p'_0 = O(1)$, occur

for $\Delta H_e = O(1)$ and finite values of τ . Chemical heating plays no role in this time-frame because the activation temperature, T_A in (8b,c), is assumed to be large.

The fluid dynamic response to the spatially distributed temperature and pressure (T_0, p_0) can be obtained by substituting the transformed density and velocity variables,

$$\rho = 1 + \varepsilon^2 R \quad , \quad \underline{u} = \varepsilon \underline{U} \quad (14a,b)$$

Into (1), (2) and (11) and taking the limit $\varepsilon \rightarrow 0$. The reduced momentum and conservation of mass equations, along with initial conditions,

$$\underline{U}_{0,\tau} = -\frac{\nabla p_0}{\gamma} \quad , \quad \underline{U}_0(r, \theta, \varphi, 0) = 0 \quad (15)$$

$$R_{0,\tau} = -\nabla \cdot \underline{U}_0 \quad , \quad R_0(r, \theta, \varphi, 0) = 0 \quad (16)$$

describes gas motion induced by the pressure (temperature) gradient created by spatially distributed heating from \dot{Q}_e , and the concomitant density variation. Equations (5a) and (14b) can be used to show that the local gas speed is characterized by $O(\varepsilon a'_0)$ or the local Mach number, $\underline{u}/T^{1/2} = O(\varepsilon)$, is very small. Solutions to (13), (15) and (16) can be written in quadrature form;

$$T_0 = 1 + \gamma(\gamma - 1) \Delta H_e \int_0^\tau \dot{Q}_e(r, \theta, \varphi, \hat{\tau}) d\hat{\tau} \quad , \quad p_0 = T_0 \quad (17a,b)$$

$$\underline{U}_0 = -\frac{1}{\gamma} \int_0^\tau \nabla T_0 d\tau \quad (18)$$

$$R_0 = -\int_0^\tau \nabla \cdot \underline{U}_0 d\tau \quad , \quad (19)$$

for $r \leq r_s$ (θ, φ) defined in (12) where ∇ represents the gradient operator in spherical coordinates.

Relatively elementary (analytical) solutions can be obtained for a model source function,

$$\dot{Q}_e = w(r)F(\theta, \varphi)g(\tau) \quad , \quad (20a)$$

where

$$w(r) > 0 \quad , \quad r < r_s(\theta, \varphi) \quad , \quad (20b)$$

$$w(r) = 0 \quad , \quad r \geq r_s(\theta, \varphi) \quad , \quad (20c)$$

$$g(0) = 0 \quad , \quad (20d)$$

$$g(\tau) > 0 \quad , \quad \tau > 0 \quad , \quad (20e)$$

$$\lim_{\tau \rightarrow \infty} g(\tau) = g_\infty > 0 \quad , \quad g_\infty = \text{constant} \quad (20f)$$

The energy deposition associated with the source is confined to a targeted region $r < r_s(\theta, \varphi)$, and is assumed to asymptote to a purely spatial distribution for large values of the time variable τ .

The time-varying spatial variation in temperature, found by substituting (20a) into (17), is determined by the product $w(r)F(\theta, \varphi)$;

$$T_0(r, \theta, \varphi, \tau) = 1 + \gamma(\gamma - 1)\Delta H_e w(r)F(\theta, \varphi) \int_0^\tau g(\hat{\tau}) d\hat{\tau} \quad (21)$$

Then from (18) and (19) the velocity and the density perturbation are described by

$$\underline{U}_0(r, \theta, \varphi, \tau) = -(\gamma - 1)\Delta H_e \nabla \left[w(r)F(\theta, \varphi) \right] \int_0^\tau d\hat{\tau} \int_0^{\hat{\tau}} g(\sigma) d\sigma \quad (22)$$

$$R_0(r, \theta, \varphi, \tau) = (\gamma - 1)\Delta H_e \nabla^2 \left[w(r)F(\theta, \varphi) \right] \int_0^\tau d\hat{\tau} \int_0^{\hat{\tau}} d\sigma \int_0^\sigma g(\hat{\sigma}) d\hat{\sigma} \quad (23)$$

The definition of the source function $w(r)$ in (20b,c) can be used in (21) and (22) to show that at the edge of the spot $r = r_s(\theta, \varphi)$, the temperature $T_0(r_s, \theta, \varphi, \tau) = 1$, the radial velocity component is

$$U_{0r}(r_s, \theta, \varphi, \tau) = -(\gamma - 1)\Delta H_e F(\theta, \varphi) \frac{dw(r_s)}{dr} \int_0^\tau d\hat{\tau} \int_0^{\hat{\tau}} g(\sigma) d\sigma \quad (24)$$

while the angular components $U_{0\theta}$ and $U_{0\phi}$ vanish. Equation (23) shows that the density perturbation at the edge $R_0(r_s, \theta, \phi, \tau)$ can be nonzero. When $dw/dr(r_s) \neq 0$, the radial velocity at the spot edge in (24) is the source of acoustic waves in the adjacent cold gas environment that are described in section 2.3, below.

Example solutions of (21)-(23) for a simple spherically symmetric source defined by

$$w(r) = \cos(\pi r/2) \quad , \quad F(\theta, \phi) = 1 \quad , \quad g(\tau) = g_\infty(1 - e^{-\tau}) \quad , \quad r \leq 1 \quad (25a,b,c)$$

are

$$T_0 = 1 + \gamma(\gamma - 1)\Delta H_e g_\infty \cos \frac{\pi r}{2} (\tau - 1 + e^{-\tau}) \quad (21a)$$

$$U_{0r} = (\gamma - 1)\Delta H_e g_\infty \frac{\pi}{2} \sin \frac{\pi r}{2} \left(\frac{\tau^2}{2} - \tau - e^{-\tau} + 1 \right) \quad (22a)$$

$$R_0 = -(\gamma - 1)\Delta H_e g_\infty \frac{\pi}{2} \left(\frac{\pi}{2} \cos \frac{\pi r}{2} + \sin \frac{\pi r}{2} \right) \left(\frac{\tau^3}{6} - \frac{\tau^2}{2} + \tau - 1 + e^{-\tau} \right) \quad (23a)$$

where the spatial structure is determined by $w(r)$ in (25a) and the time dependence follows from $g(\tau)$ in (25c). The temperature distribution in (21a) is radially symmetric with a maximum at each value of τ located at $r = 0$, and a minimum at $r = 1$. The spatial amplitude at each radial location grows linearly with $\tau \gg O(1)$ due to the sustained energy input. Meanwhile, the thermomechanically-induced radial fluid speed increases from zero at $r = 0$ to a maximum at $r = 1$;

$$r = 1 \quad ; \quad U_{0r} = \left(\frac{\pi}{2} \right) (\gamma - 1) \left(\frac{\tau^2}{2} - \tau + 1 - e^{-\tau} \right) \quad . \quad (26)$$

When $t' = O(t'_H)$ or $\tau = O(1)$, this accelerating edge speed, associated with an $O(\varepsilon)$ local Mach number, given the definition in (14b), is a “piston-like” source of acoustic waves [3]. The

waves can move a distance $\Delta r'_w = O(t'_H a'_0) = O(\varepsilon R')$, small compared to the spot dimension itself. It should also be noted that the fluid itself is convected a characteristic distance $\Delta r'_F = O(\varepsilon^2 R')$.

The mass loss at the edge ($r = 1$) compatible with (26) causes a density decrement within the hot spot, described by (23a). The spatial structure function is positive for $0 \leq r \leq 1$ and the spatial amplitude increases like $O(\tau^3)$ for $\tau \gg O(1)$. Note that $R_0(r = 1, \tau) < 0$ implying that the density (14a) is slightly smaller than the initial value.

2.3 Local Linear Acoustics: $r \geq 1$

The acoustic region variables, defined by

$$r = 1 + \varepsilon \bar{r} \quad , \quad \bar{r} \geq 0 \quad , \quad \underline{u} = \varepsilon \underline{U} \quad , \quad (p-1, \rho-1, T-1) = \varepsilon (\bar{p}, \bar{R}, \bar{T}) \quad , \quad (27a,b,c)$$

with $\dot{Q} = 0$ are used to describe an acoustic disturbance in a thin boundary layer around the edge of the spherical spot for the example source functions in (25). The $O(\varepsilon)$ magnitude of the thermodynamic variables perturbation is compatible with an $O(\varepsilon)$ edge Mach number defined by (26) and (27b), valid when $\tau \ll O(1/\varepsilon^{1/2})$. Equation (27) can be used in (1)-(4) and (11) to find linear acoustic equations valid in the limit $\varepsilon \rightarrow 0$,

$$\bar{R}_{0,r} + \nabla \cdot \underline{U}_0 = 0 \quad , \quad \underline{U}_{0,r} = -\frac{1}{\gamma} \nabla \bar{p}_0 \quad (28a,b)$$

$$\bar{p}_0 = \gamma \bar{R}_0 \quad , \quad \bar{p}_0 = \bar{T}_0 + \bar{R}_0 \quad (29a,b)$$

Equations (28) and (29) can be combined to find a simple wave equation for the radial velocity component U_{0r}

$$\frac{\partial^2 U_{0r}}{\partial \tau^2} = \nabla^2 U_{0r} \quad (30)$$

subject to initial conditions,

$$\tau = 0 \quad , \quad U_{0r} = \frac{\partial U_{0r}}{\partial r} = 0 \quad , \quad r > 1 \quad (31)$$

and the boundary condition from (26). The solution can be written in the compact form [23]

$$U_{0r} = \frac{\varphi(\eta)}{r} \quad , \quad \eta = r - \tau \leq 1 \quad (32a)$$

$$= 0 \quad , \quad \eta > 1 \quad (32b)$$

where φ is the function on the right side of (26) with τ replaced by $1 - \eta$. The acoustic velocity disturbance described by (32), and the associated thermodynamic variations found from (28a) and (29) are smooth functions with benign front properties but are valid only for $\eta \ll O(1/\varepsilon^{1/2})$. The limitation arises because the boundary condition in (26) defines an accelerating “piston” speed that eventually exceeds the small Mach number condition implicit in the derivation of (28) and (29). U_{0r} and its first spatial derivative are zero at the front $\eta = 1$. The discontinuity with respect to the undisturbed value for $\eta > 1$ is in the second spatial derivative. These function characteristics arise from the properties of the time-resolved source in (25c). One may note from (26) that the effective “piston speed” associated with the expanding hot gas is $O(\tau^3)$ for $\tau \ll 1$. This relatively gentle startup process should be compared with typical instantaneous acceleration problems, which display solutions with discontinuous functions at the front [22]. In contrast, the edge speed increases like $O(\tau^2)$ for large time values, implying that successively stronger disturbances will appear in the far-field as time evolves. It is noted from (27c) that the acoustic temperature change is $O(\varepsilon)$ implying that the chemical reaction is suppressed in the external environment for $\tau = O(1)$.

Finally, it is noted that more general acoustic results can be obtained by using the edge speed in (24) as the “piston-like” source of disturbances. The acoustic characteristics will depend on the spatial and time dependence of the model source function in (20a).

2.4 Transport Effects near $r = 1$.

The rising temperature in the heated region caused by the source defined in (12) will, in general, lead to a finite temperature gradient near the edge of the spot and conduction into the cold environment. An assessment of the conduction process on the heating time scale t'_H ($\tau = O(1)$) can be obtained by transforming the energy equation (3) with scaled variables that describe small temperature variations from the edge value $T = 1$ in a thin boundary layer in the vicinity of $r_s(\theta, \varphi)$. A balance of energy accumulation, the absorbed heat and the conduction term can be used to show that $T - 1 = O(\beta^{1/2})$ and $r - r_s(\theta, \varphi) = O(\beta^{1/2})$. Given the definition of β and ε in (9a,b), it follows that $\beta^{1/2}$ can be less than ε . In the asymptotic limit, the conduction boundary layer is much thinner than the acoustic layer defined in (27a) and the local temperature variation $O(\beta^{1/2})$ is minute relative to the $O(\varepsilon)$ acoustic temperature disturbance. Finally, the ratio of the characteristic heat loss rate at the surface of the spot to the volumetric power absorption is $O(\beta)$, which is negligible in the limit $\varepsilon \rightarrow 0$.

2.5 Asymptotic Solution Properties: $\tau \rightarrow \infty$

A study of the solution properties for $\tau \rightarrow \infty$ from (17)-(19) provides an opportunity to describe how the rising spot temperature can initiate a high activation energy reaction associated with the kinetics term $e^{-T_A/T}$ where $\lim_{\varepsilon \rightarrow 0} T_A(\varepsilon) \rightarrow \infty$. When the exponential term is $O(1)$, or $T = O(T_A)$, one can anticipate a strong exothermic reaction.

Asymptotic behavior of the temperature, pressure, speed and density can be obtained easily for the generalized deposition heat source

$$\dot{Q}_e = f(r, \theta, \varphi) g(\tau) \quad (33a)$$

where

$$f(r, \theta, \varphi) > 0 \quad , \quad r < r_s(\theta, \varphi) \quad (33b)$$

$$f(r, \theta, \varphi) = 0 \quad , \quad r > r_s(\theta, \varphi) \quad (33c)$$

and $g(\tau)$ has the properties defined in (20e) and (20f).³ Equations (17)-(19) can be evaluated to show that

$$\lim_{\tau \rightarrow \infty} T_0 \sim \tau \quad , \quad \lim_{\tau \rightarrow \infty} p_0 \sim \tau \quad (34a,b)$$

$$\lim_{\tau \rightarrow \infty} U_0 \sim \tau^2 \quad , \quad \lim_{\tau \rightarrow \infty} R_0 \sim \tau^3 \quad (34c,d)$$

In addition, the local Mach number

$$M_\ell \equiv \frac{|u'|}{a'} = \frac{\varepsilon |U_0|}{T_0^{1/2}} \sim \varepsilon \tau^{3/2} \quad (35)$$

The high activation energy reaction is initiated when $T_0 \sim \tau = O(T_A)$. Then (14), (34), and (35) imply that

$$T = O(T_A) \quad , \quad p = O(T_A) \quad , \quad \underline{u} = O(\varepsilon T_A^2) \quad (36a,b,c)$$

$$\rho - 1 = O(\varepsilon^2 T_A^2) \quad , \quad M_\ell = O(\varepsilon T_A^{3/2}) \quad (36d,e)$$

where $T_A \gg O(1)$. The dependence of the local Mach number, M_e , on both ε and T_A can be used to discriminate between two kinds of evolutionary reactive gas-dynamic processes on an extended time scale:

³ Other forms of time-dependence can be evaluated.

$$(a) \text{ incompressible limit: } M_\ell \ll 1 \quad , \quad 1 \ll T_A \ll O(\varepsilon^{-2/3}) \quad (37a,b)$$

$$p = T \ll O(\varepsilon^{-2/3}) \quad , \quad \underline{u} \ll O(\varepsilon^{-1/3}) \quad , \quad (\rho - 1) = o(1) \quad (37c,d,e)$$

$$(b) \text{ compressible limit: } M_\ell = O(1) \quad , \quad T_A = O(\varepsilon^{-2/3}) \quad (38a,b)$$

$$p = T = O(\varepsilon^{-2/3}) \quad , \quad \underline{u} = O(\varepsilon^{-1/3}) \quad , \quad (\rho - 1) = O(1) \quad (38c,d,e)$$

Equations (37b) and (38b) provide explicit limitations on T_A for a prescribed ε , or vice versa. The incompressible case, characterized by a small local Mach number (37a) and small density variation (37e), can be expected to retain the near inertial confinement properties found for the initial heating period $\tau = O(1)$. In contrast, the compressible limit properties in (38) imply a more significant transient gas dynamic process, including the conversion of significant amounts of thermal energy to kinetic energy.

A physical explanation for the failure of inertial confinement when $T_A = O(\varepsilon^{-2/3})$ can be obtained by considering the ratio of the dimensional extended heating time $t'_{He} = t'_H T_A$, derived from $\tau = O(T_A)$, to the dimensional local acoustic time $t'_{Ae} \equiv R'/a' = t'_A / \sqrt{T} = O(t'_A / T_A^{1/2})$,

$$\frac{t'_{He}}{t'_{Ae}} = \varepsilon T_A^{3/2} \quad (39)$$

Inertial confinement can prevail only when the ratio is small, corresponding to case (a). When $T_A = O(\varepsilon^{-2/3})$, the ratio is $O(1)$, implying that acoustic wave can traverse the spot on a time scale comparable to that for extended heating.

The scaling contained in (36)-(38) can now be employed to define rescaled variables and new limiting equations for the reactive initiation portion of the process.

3. Reaction Evolution: $t' = O(T_A t'_H)$

3.1 Incompressible Limit

The temporal nonuniformities of the inert heating period solutions in (34)-(36) imply that the rescaled variables for the reactive incompressible limit are;

$$\tau = T_A \tilde{\tau} \quad , \quad 1 \ll T_A \ll O(\varepsilon^{-2/3}) \quad (40a,b)$$

$$(p, T) = (T_A \tilde{p}, T_A \tilde{T}) \quad (40c,d)$$

$$\rho = 1 + \varepsilon^2 T_A^3 \tilde{R} \quad (40e)$$

$$\underline{u} = \varepsilon T_A^2 \tilde{\underline{u}} \quad (40f)$$

These variables describe an extended period of thermal energy deposition from a combination of external source and exothermic chemical heat release. The definition of \dot{Q}_e below (5)-(10) implies that the characteristic dimensional power deposition during the inert period $\tau = O(1)$ is given by $\dot{Q}'_e = O(\Delta H'_e / t'_H) = O(a_0'^2 / t'_H) = O(e'_0 / t'_H)$ where definitions below (5)-(10) have been used. It follows that energy deposition during that period $t' = O(t'_H)$ is simply $\dot{Q}'_e t'_H = O(e'_0)$. In contrast, energy deposition on the extended time scale $t' = O(T_A t'_H)$ is $\dot{Q}'_e t'_H T_A = O(e'_0 T_A) = O(C'_v T'_A)$. The inequality in (40b) implies that $T'_A \ll T'_0 / \varepsilon^{2/3}$. It follows that characteristic energy deposition for the incompressible limit is restricted to $\dot{Q}'_e t'_H T_A \ll O(C'_v T'_0 / \varepsilon^{2/3}) = O(e'_0 / \varepsilon^{2/3})$. In other words, the nearly inertially confined heating process will occur only if the energy added during the extended heating period is sufficiently small. This class of limitation, identical to that found in Ref. [2] for inert gas thermomechanics must be a universal characteristic of rapid localized heat addition to a variable density fluid. The

extreme case of energy addition corresponding to $T_A = O(1/\varepsilon^{2/3})$ is associated with a fully compressible, high internal Mach number flow. Details are given in Section 3.2.

The temperature and pressure changes are large, while the density variation is small. Examination of (40f) shows that the nondimensional speed, based on a'_o (see (5b)), can take on a wide range of values. In particular, at the edge of the spot ($T' = T'_o$), the edge Mach number

$$u'_e/a'_0 \ll O(1) \quad , \quad 1 \ll T_A \ll \varepsilon^{-1/2} \quad , \quad \tau \ll \varepsilon^{-1/2} \quad (41a)$$

$$u'_e/a'_0 = O(1) \quad , \quad T_A = O(\varepsilon^{-1/2}) \quad , \quad \tau = O(\varepsilon^{-1/2}) \quad (41b)$$

$$u'_e/a'_0 \gg O(1) \quad , \quad \varepsilon^{-1/2} \ll T_A \ll \varepsilon^{-2/3} \quad , \quad \tau \ll \varepsilon^{-2/3} \quad (41c)$$

where $u'_e = |\underline{u}'_e|$ and the third inequality in each of (41) follows from the time transformation in (40a). The subsonic edge Mach number in (41a) is compatible with the linear acoustic solution in (32a), due to the specified time extent $\tau \ll \varepsilon^{-1/2}$.

Accordingly, the character of the gasdynamics in the cold external environment, driven by gas expansion at the edge will differ considerably, depending on the particular value of T_A . In contrast, the local Mach number inside the spot $M_e = |\underline{u}'|/a' = |\underline{u}|/\sqrt{T} = O(\varepsilon T_A^{3/2}) \ll 1$.

Equation (40) can be substituted into (1)-(4) to derive the describing equations for the extended heating period $\tau = O(T_A)$.

$$\tilde{R}_{\tilde{\tau}} + \nabla \cdot (\rho \tilde{\underline{u}}) = 0 \quad (42a)$$

$$\rho \left(\tilde{\underline{u}}_{\tilde{\tau}} + \varepsilon^2 T_A^3 (\tilde{\underline{u}} \cdot \nabla) \tilde{\underline{u}} \right) = -\frac{\nabla \tilde{p}}{\gamma} - \beta T_A^{1+n} \tilde{\underline{V}} \quad (42b)$$

$$\frac{1}{(\gamma-1)} \rho \left(\tilde{T}_{\tilde{\tau}} + \varepsilon^2 T_A^3 \tilde{\underline{u}} \cdot \nabla \tilde{T} \right) = -\varepsilon^2 T_A^3 \tilde{p} \nabla \cdot \tilde{\underline{u}} + \gamma \Delta H_e \rho \dot{Q} + \beta T_A^{1+n} \left[\frac{\gamma}{(\gamma-1)} \frac{\tilde{C}}{\text{Pr}} + \gamma \varepsilon^2 T_A^3 \tilde{\Phi} \right] \quad (42c)$$

$$Y_{\tilde{r}} + \varepsilon^2 T_A^3 \tilde{\underline{u}} \cdot \nabla Y = -\delta T_A Y e^{-1/\tilde{T}} + \frac{\beta}{Sc} T_A^m \frac{\tilde{D}}{\rho} \quad (42d)$$

$$\dot{Q} = \tilde{Q}_e + \Omega Y e^{-1/\tilde{T}} \quad (42e)$$

$$\tilde{p} = (1 + \varepsilon^2 T_A^3 \tilde{R}) \tilde{T} \quad (42f)$$

where power law dependence for viscosity, conductivity and diffusion coefficient, respectively, defined by $\mu = T^n$, $k = T^n$ and $D = T^m/p$, where $n < 1$ and $m < 1$, are assumed for the nondimensional transport equations to provide a model that includes high temperature transport effects.

Eq. (42) reduces to a relatively elementary system in the limit $\varepsilon \rightarrow 0$ because all of the transport term parameters are vanishingly small (see the definition of β in (9b), and Table 1 for characteristic values of t'_v , while $T_A \leq 50$ is typical).

$$\tilde{R}_{0_{\tilde{r}}} + \nabla \cdot \tilde{\underline{u}}_0 = 0 \quad , \quad \tilde{\underline{u}}_{0_{\tilde{r}}} = -\frac{\nabla \tilde{p}_0}{\gamma} \quad (43a,b)$$

$$\frac{1}{(\gamma-1)} \tilde{T}_{0_{\tilde{r}}} = \gamma \Delta H_e \left[\dot{Q}_e + \Omega Y_0 e^{-1/\tilde{T}_0} \right] \quad , \quad \dot{Q}_e = \dot{Q}_e(r, \theta, \varphi, \tilde{\tau}) \quad (43c,d)$$

$$Y_{0_{\tilde{r}}} = -\delta T_A Y_0 e^{-1/\tilde{T}_0} \quad , \quad \tilde{p}_0 = \tilde{T}_0 \quad (43e,f)$$

where Ω and δ are defined in (10a) and (9c), respectively, and \dot{Q}_e represents the effect of continued external thermal power deposition. It is assumed that the heat of reaction $\Delta H_{ch} = O(T_A)$ in order to assure that the temperature increase due to exothermicity is of the same magnitude as that due to external source effects on the time scale $\tilde{\tau} = O(1)$. In addition, it is assumed that $\delta = O(1/T_A)$ to assure $O(1)$ reactant consumption on the time scale $\tilde{\tau} = O(1)$. Both assumptions are physically viable. Equation (43) describes an extended period of nearly-inertially confined thermal power deposition, including a small change in density in an internally

low Mach number expansion process. Equations (43c) and (43e) can be combined to define a Schwab-Zeldovich variable [24] used to find $Y_0 = Y_0(\tilde{T}_0)$;

$$Y_0 = 1 + \frac{\Delta H_e}{\Delta \tilde{H}_{ch}} \int_0^{\tilde{\tau}} \dot{Q}_e d\tilde{\tau}^* - \frac{\tilde{T}_0}{\Delta \tilde{H}_{ch} \gamma (\gamma - 1)} \quad , \quad \Delta \tilde{H}_{ch} = \frac{\Delta H_{ch}}{T_A} = O(1) \quad (44)$$

Equation (44) can be used to find the maximum temperature $\tilde{T}_0(\tau = \infty)$ associated with complete reactant consumption $Y_0 = 0$

$$\tilde{T}_0(\tilde{\tau} = \infty) = \gamma(\gamma - 1) \left[\frac{\Delta H_{ch}}{T_A} + \Delta H_e \int_0^{\infty} \dot{Q}_e(r, \theta, \varphi, \tilde{\tau}) d\tilde{\tau} \right] \quad (45)$$

where the first term on the right-hand side represents the adiabatic temperature rise from constant volume complete reactant consumption and the second term is the total temperature rise associated with the sustained external source energy deposition.

An equation for \tilde{T}_0 is found by combining (43c), (44) and (45)

$$\tilde{T}_{0\tilde{\tau}} = \gamma(\gamma - 1) \Delta H_e \dot{Q}_e + \frac{\Delta H_e}{\Delta \tilde{H}_{ch}} \Omega e^{-1/\tilde{T}_0} \left[(\tilde{T}_0(\infty) - \tilde{T}_0) - \gamma(\gamma - 1) \Delta H_e \int_{\tilde{\tau}}^{\infty} \dot{Q}_e d\tilde{\tau}^* \right] \quad (46)$$

The initial condition on \tilde{T}_0 is found formally by using the matching expression from (40d) $\tilde{T}_0(\tilde{\tau} \rightarrow 0) = T(\tau \rightarrow \infty)/T_A = 0$, meaning that looking back in time to the period $\tau = O(1)$, the temperature is asymptotically small compared to that when $\tilde{\tau} = O(1)$. Equation (46) can be integrated numerically to find $\tilde{T}_0(r, \theta, \varphi, \tilde{\tau})$ for a specified external heat source \dot{Q}_e . Reactant consumption is defined by (44). The locally high pressure, defined by (43f), can be used in (43b) to find the local thermomechanically induced fluid motion. Finally the density distribution is found by integrating (43a). The equation system bears a striking resemblance to that discussed in Ref. [2] in the context of the response of an inert gas to extremely rapid transient, spatially resolved energy addition.

The systematically derived reduced equations (43-46) provide a formal validation for the Zeldovich [19] detonation initiation model based on constant volume thermal explosion evolution. The current analysis provides specific parametric conditions for which the model is valid and those for which it is not (see Section ?). Related concepts have been developed earlier by Jackson *et al.* [9] and Short [10, 11].

Once \tilde{T}_0 and Y_0 are found from (46) and (44), respectively, 43b and f can be used to find the thermomechanically-induced velocity

$$\tilde{u}_0 = -\int_0^{\tilde{\tau}} \frac{\nabla \tilde{T}_0}{\gamma} d\tilde{\tau}^* \quad (47)$$

Finally, the small density distribution represented by \tilde{R}_0 in the context of (51e) is found from

$$\tilde{R}_0 = -\int_0^{\tilde{\tau}} \nabla \cdot \tilde{u}_0 d\tilde{\tau}^* \quad (48)$$

A numerical solution to (46) for $\tilde{T}_0(r, \tilde{\tau})$ with the initial condition $\tilde{T}_0(r, 0) = 0$ has been found for the axisymmetric source $\dot{Q}_e = (1 - \tilde{\tau}) \cos \pi(r/2)$, ($0 < r \leq 1$) when $0 \leq \tilde{\tau} \leq 1$, and $\dot{Q}_e = 0$ when $\tilde{\tau} \geq 1$ for a few values of the parameters ΔH_e and Ω with $\Delta H_{ch} = 1$ (see (44)). Beyond the edge of the spot located at $r = 1$, $\dot{Q} = 0$. The radial dependence of the scaled temperature \tilde{T}_0 is given in Fig. 1 for several values of the scaled time when $\Delta H_e = 5$ and $\Omega = 10$. At each value of r , the temperature varies from 0 to a maximum value obtained from (45). Source heating causes the temperature to rise in $0 \leq r \leq 1$ for $\tilde{\tau} \leq 0.1$. Thereafter, localized chemical heat release causes a relatively rapid temperature increase in the hottest portion of the spot. By the time $\tilde{\tau} = 1$ when the source is turned off, approximately 85% of the spot has reached the maximum temperature value. A substantial radial temperature gradient appears in the vicinity of the $r = 0.9$ and becomes steeper as time increases. Fig. 2 shows the evolution of the gradient near the edge of the

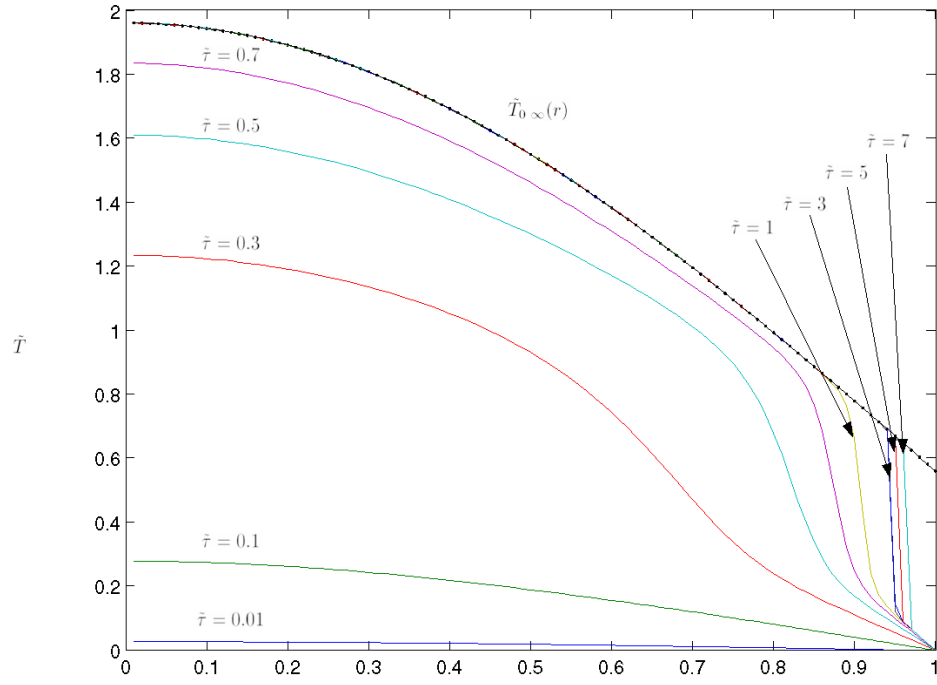


Fig. 1. Temperature Profiles: $\Delta H = 5$. $\Omega = 10$

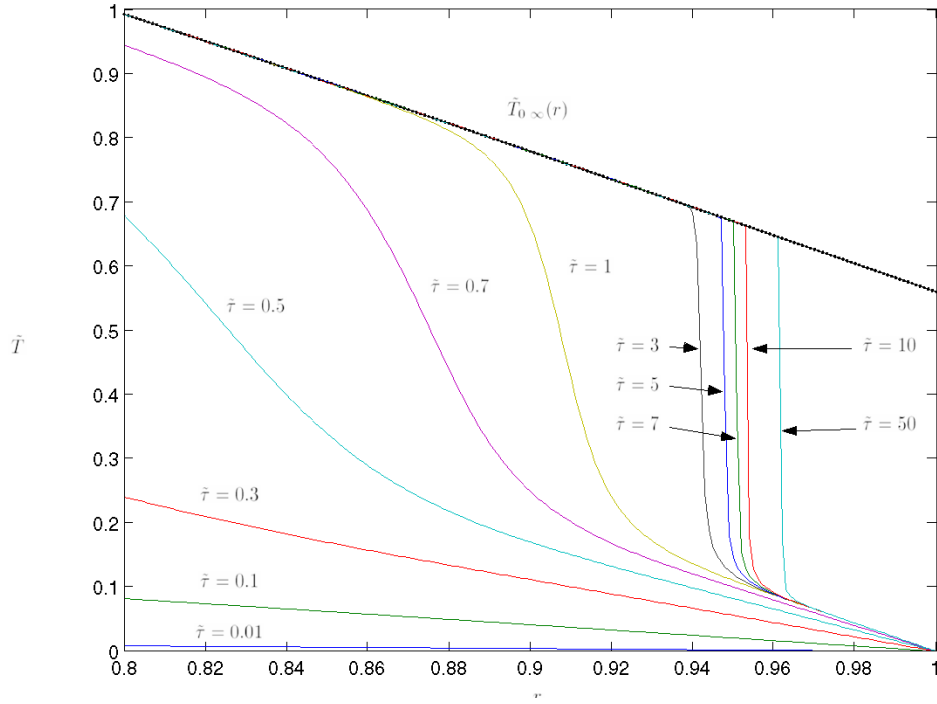


Fig. 2. Temperature Profiles: $\Delta H = 5$. $\Omega = 10$

spot for much larger times. The temperature distribution is evolving to a discontinuous function near the edge, $r \rightarrow 1$. This essentially constant volume process is characterized by $\tilde{p}_0 = \tilde{T}_0$, so that the high temperature gas region is also at a locally large pressure. Equation 47 implies that the large gradient region is a source of localized fluid acceleration.

The narrow spatial region denoted by the large gradient separates hot burned gas on the left from cold unburned material on the right. Results for the spatial distribution of reactant Y , shown in Fig. 3, can be interpreted in terms of a reaction front propagating through the spot. If one examines the change in the location of the $Y = 0.5$ value with time during the period $0.3 \leq \tilde{\tau} \leq 1$ and converts the results to dimensional values (e.g, using (6a,b), (40a,d)) it can be shown that the front propagation speed, relative to the local (hot) speed of sound, a' , is $V_F'/a' = V_F'/\sqrt{T_A}\tilde{T} = O(1)$ with respect to the limit $\varepsilon \rightarrow 0$. Results in Fig. 2 for large values of time shows that the front speed decelerates drastically as it moves into the colder gas ahead where the local “explosion” time is much longer than that in the hotter gas region. Near $r = 1^-$, the temperature distribution is essentially frozen for $\tilde{\tau} \geq 1$ because the source is extinguished and the gas is too cold to produce any significant amount of thermal energy. The local finite gradient implies that fluid expelled from the hot spot edge (e.g, (47)) will be a continuing source of acoustic or stronger disturbances (e.g, see (41)) in the external cold gas with consequences similar to these described in [22].

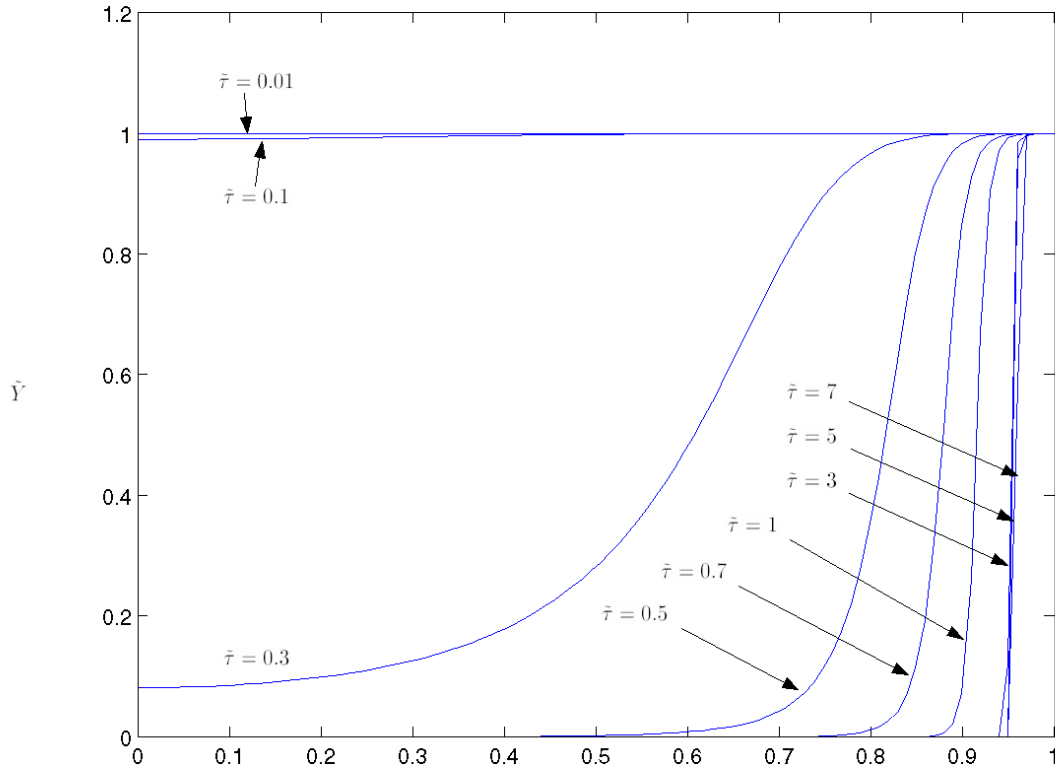


Fig. 3. Concentration Profiles: $\Delta H = 5$, $\Omega = 10$

Temperature results for the parameter values $\Delta H_c = 1$ and $\Omega = 50$ are given in Fig. 4. In this case the reaction process is initiated more slowly because the source strength is reduced by a factor five. However the reactive phase is stimulated by a much larger value of Ω . The thermomechanically induced radial fluid velocity, shown in Fig. 5 for a limited range of the time variable, is caused by the large local gradient in temperature and pressure as defined by (43b) and (47). Larger time values are displayed in Fig. 6. These results show rather substantial growth in the maximum speed values, nondimensionalized with respect to the cold speed of sound, a'_0 . The maximum values listed in the inset in Fig. 6 are quite large. These results should be interpreted with the knowledge that the local Mach number, with reference to the hot speed of sound is very small, as noted below (41c).

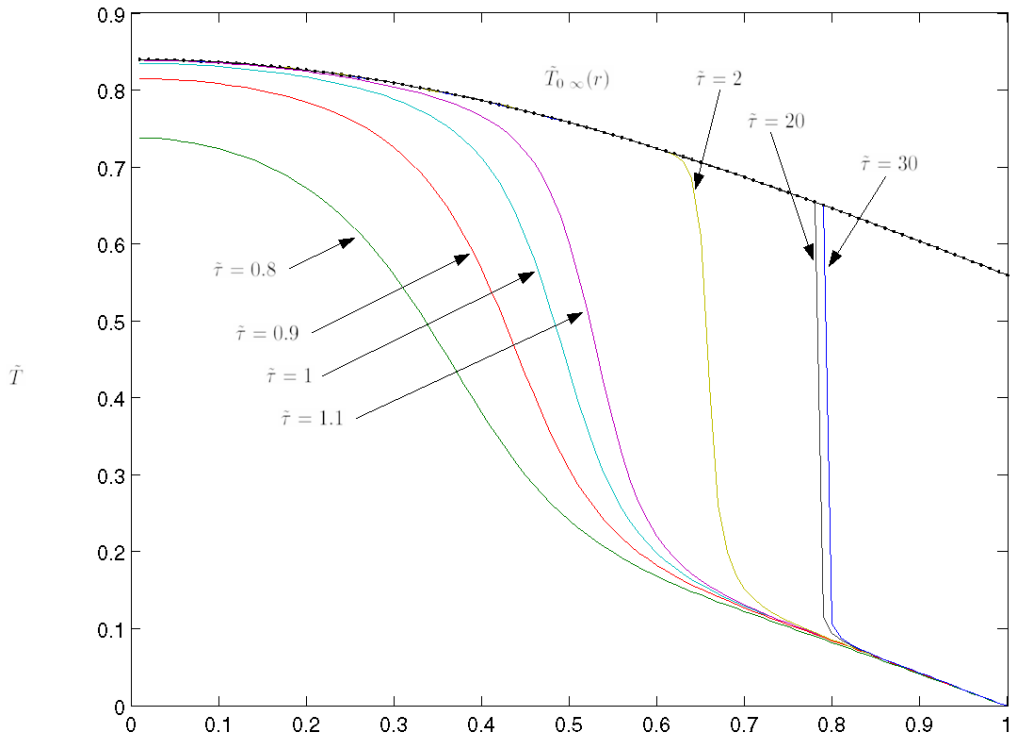


Fig. 4. Temperature Profiles: $\Delta H = 1$. $\Omega = 50$

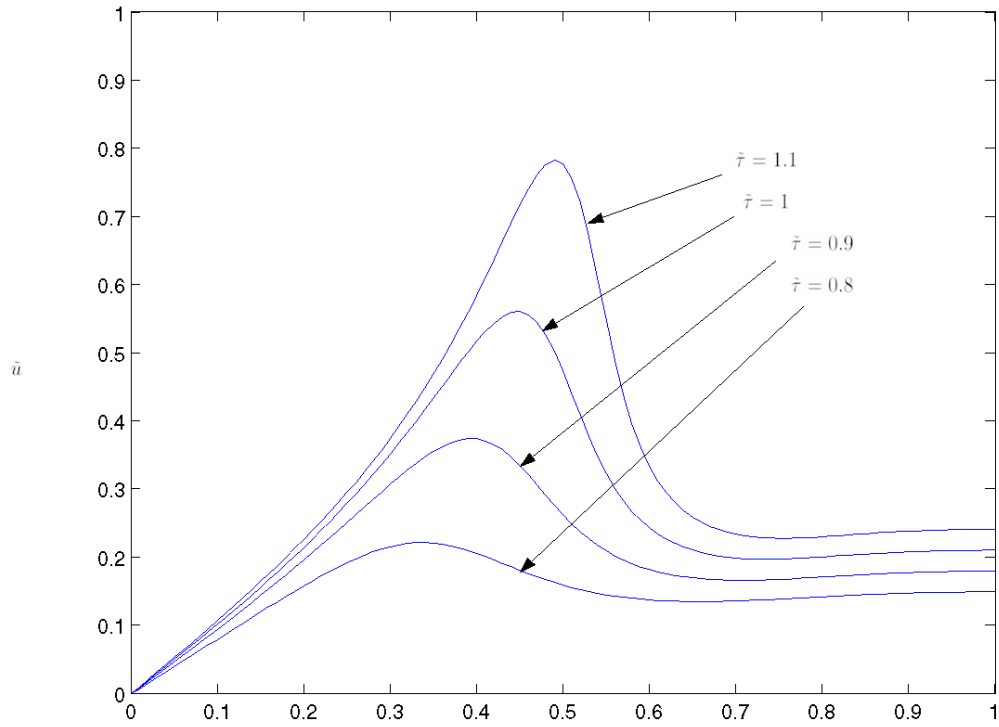


Fig. 5. Velocity Profiles: $\Delta H = 1$. $\Omega = 50$

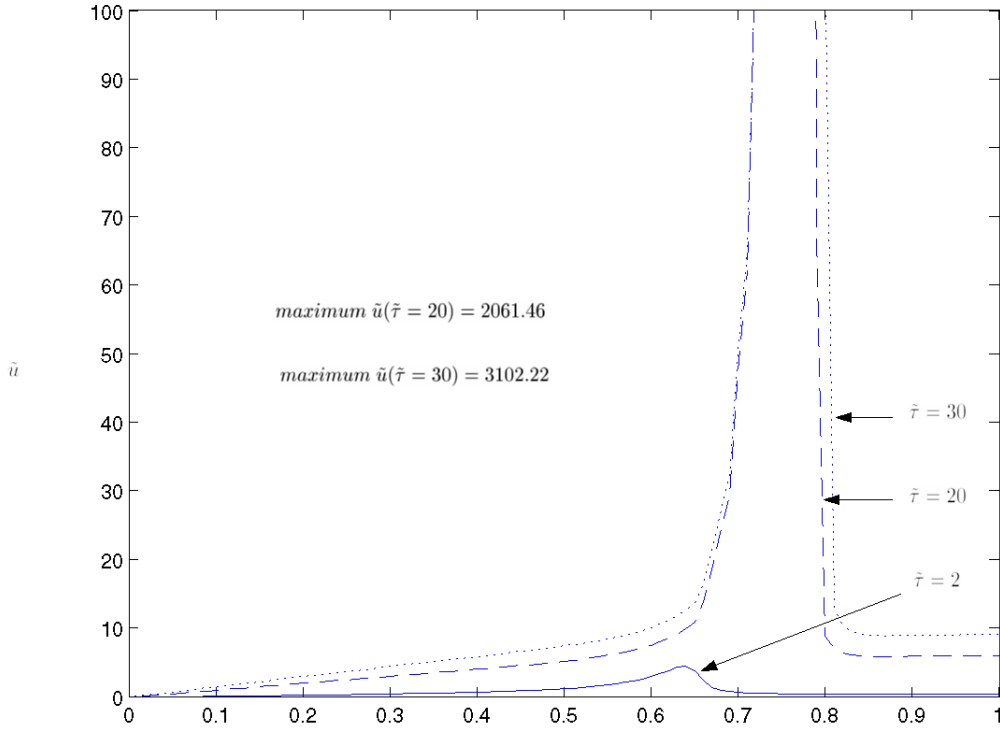


Fig. 6. Velocity Profiles: $\Delta H = 1$. $\Omega = 50$

It may be tempting to associate the pressure, temperature and reactant concentration jumps observed in the figures with a reactive shock. However, on the reactive heating time-scale of interest (40a) the physical process is occurring in a primarily incompressible fluid and the front is observed to stagnate. In fact, an ephemeral hot, high pressure, low speed, burned out spot has been generated by a momentary inertial confinement process during the extended chemical heating time. The huge pressure gradient across the front will be the source of a localized relaxation process, characterized by hot spot gas expansion on the longer acoustic time scale of the spot. The front will be driven into the surrounding unburned reactant leading to the appearance of new localized combustion waves. Elucidation of this relaxation process is the subject of a current investigation.

The nondimensional results in Figs. 1-6 can be interpreted in terms of a dimensional example based on the following data.

$$R' = 10^{-3} \text{ m} , \quad T'_0 = 300 \text{ K} , \quad p'_0 = 1 \text{ atm} , \quad a'_0 = 340 \text{ m/s} , \quad t'_A = 2.9 \times 10^{-6} \text{ s} ,$$

$$t'_H = 10^{-7} \text{ s} , \quad \varepsilon = .034 ,$$

$$\Delta H_e = O(10^5 \text{ J/kg}) , \quad T_A = 1/\varepsilon^{1/2} = 5.42 ,$$

where the T_A value is midrange in (40). The characteristic high temperature $T_A T'_0$ is about 1600K and the corresponding high pressure $T_A p'_0$ about 5.5 atm (see (40)). The small density change is $O(\varepsilon^{1/2})$ and the local Mach number is $O(\varepsilon^{1/4})$.

3.1.1 Linear Acoustic Wave Evolution: $\tilde{t} = O(1)$

Acoustic disturbances of $O(\varepsilon)$ amplitude described in Section 2.3 by (27) propagate at a characteristic dimensional speed a'_0 during the interval $t' = O(t'_H)$. The characteristic distance traveled is $O(\varepsilon R')$, small compared to the hot spot dimension R' . During the extended heating time period, defined by (40a), the wave front moves a greater distance characterized by $O(\varepsilon T_A R')$. Meanwhile, larger linear acoustic disturbances are generated by the small edge Mach number defined in (41a) during the time period characterized by $\tilde{t} = O(1)$. The variable transformations

$$(p-1) , (\rho-1) , (T-1) = \varepsilon T_A^2 (\hat{p}, \hat{\rho}, \hat{T}) , \quad \underline{u} = \varepsilon T_A^2 \underline{\hat{u}} \quad (49\text{a,b,c,d})$$

$$\tau = T_A \tilde{\tau} , \quad r = 1 + \varepsilon T_A \xi \quad (50\text{a,b})$$

and the limit $\varepsilon \rightarrow 0$ can be employed in (1)-(4) to derive linear acoustic equations describing larger acoustic disturbances

$$\hat{\rho}_{\tilde{\tau}} + \nabla \cdot \hat{\underline{u}} = 0 \quad (51\text{a})$$

$$\hat{\underline{u}}_{\tilde{\tau}} = -\frac{\nabla \hat{p}}{\gamma} \quad (51\text{b})$$

$$\frac{\hat{T}_{\hat{\tau}}}{(\gamma-1)} = -\nabla \cdot \hat{\underline{u}} \quad (51c)$$

$$\hat{p} = \hat{\rho} + \hat{t} + O(\varepsilon) \quad (51d)$$

where the differential operators are written in spherically symmetric form .

These equations are subject to initial conditions associated with the much weaker wave disturbances generated during the earlier period, $\tau = O(1)$, so that the initial value of all variables $(\hat{p}, \hat{\rho}, \hat{T}, \hat{\underline{u}})$ is zero. In contrast, the fluid expelled from the hot spot boundary observed in Figs. 5 and 6 provide the boundary condition that drives the disturbances. In conclusion, there will be a sequence of acoustic disturbances of increasing amplitude propagating through the unbound gas beyond the hot spot. Further solution development for the acoustic problem is anticipated.

3.2 Compressible Limit

The rescaled variables appropriate in the compressible limit are also implied by the temporal nonuniformities in (34)-(36) when $\varepsilon T_A^{3/2} = O(1)$.

$$\tau = T_A \hat{\tau} \quad , \quad T_A = O\left(\frac{1}{\varepsilon^{2/3}}\right) \quad (49a,b)$$

$$(p, T) = T_A (\hat{p}, \hat{T}) \quad (49c)$$

$$\rho = \hat{\rho} \quad (49d)$$

$$\underline{u} = \varepsilon T_A^2 \hat{\underline{u}} = O(T_A^{1/2}) \quad (49e)$$

It follows that the conservation of mass, momentum, energy and species, as well as the state equation in (1)-(4) can be written as

$$\hat{\rho}_{\hat{\tau}} + \nabla \cdot \hat{\rho} \hat{\underline{u}} \quad (50)$$

$$\hat{\rho}(\hat{\underline{u}}_{\hat{\tau}} + \hat{\underline{u}} \cdot \nabla \hat{\underline{u}}) = -\frac{\nabla \hat{p}}{\gamma} + \beta T_A^{(1+n)} \hat{\underline{V}} \quad (51)$$

$$\frac{\hat{\rho}}{(\gamma-1)}(\hat{T}_{\hat{\tau}} + \hat{\underline{u}} \cdot \nabla \hat{T}) = -\hat{p} \nabla \cdot \hat{\underline{u}} + \gamma \Delta H_e \hat{\rho} \dot{Q} + \beta T_A^{(1+n)} \left(\frac{\gamma}{(\gamma-1)} \frac{\hat{C}}{\text{Pr}} + \gamma \hat{\Phi} \right) \quad (52)$$

$$Y_{\hat{\tau}} + \hat{\underline{u}} \cdot \nabla Y = -T_A \delta Y e^{-1/\hat{T}} + \beta T_A^m (\hat{D}/\hat{\rho} Sc) \quad (53)$$

$$\hat{p} = \hat{\rho} \hat{T} \quad (54)$$

$$\dot{Q} = \dot{Q}_e(r, \theta, \varphi, \hat{\tau}) + \frac{\Delta H_{ch} \delta}{\Delta H_e} Y e^{-1/T} \quad (55)$$

where the transport properties are identical to those below (42) and $\delta = O(1/T_A)$, $\frac{\Delta H_{ch}}{\Delta H_e} \delta = O(1)$.

The internal Mach number,

$$M = \frac{|u'|}{a'} = \frac{|u|}{\sqrt{T}} = \frac{\varepsilon T_A^2 |\hat{u}|}{T_A^{1/2} \sqrt{\hat{T}}} = O(\varepsilon T_A^{3/2}) = O(1) \quad (56)$$

Equations (50)-(55) describe a fully compressible, reactive flow with primarily small transport effects except where velocity, temperature, and concentration gradients are exceptionally large. The internal Mach number is substantial and can be supersonic. The internal dynamics of the reactive hot spot must be determined by a numerical solution of (50)-(55). The consequences of those dynamics will determine the gasdynamic disturbances in the far-field. Kassoy [2] has shown that the inert analogue of (50)-(55) is compatible with a strong blast wave in the unheated external environment. In fact, it can be demonstrated, using the results in [2] that the blast wave is actually initiated within the inert near-field volume, far from the origin and at a large value of the relevant time scale. One can expect similar properties for the near-field gas dynamics in a reactive hot spot. Numerical solutions are required to understand the details and will be the subject of a future communication.

4. Context, Summary and Conclusions

4.1 Context

Transient, spatially distributed combustion in a turbulent flow is thought to be the source of acoustic and stronger mechanical disturbances in a LRE chamber. Surprisingly, a quantitative model for mechanical wave generation in a transient, spatially distributed reacting flow does not appear to be available in the technical literature. Kassoy's thermomechanics-based formulation [2] for related processes in an inert gas identifies a quantitative relationship between time resolved, localized power deposition into a finite volume of gas and the magnitude of acoustic or stronger disturbances generated in the neighboring unheated, unconfined gas. The results demonstrate that the thermomechanical response of the heated gas depends on a complex relationship between the magnitude of energy deposited and the time scale for that deposition, but not simply on the power deposition alone. The theory is limited to heating time scales small compared to the acoustic time of the volume, a condition necessary for the pressure to rise with temperature (while the density change is marginal). When the energy deposition is quantitatively limited, nearly constant volume heating occurs (near-inertial confinement), characterized by a small internal gas expansion Mach number defined with respect to the high temperature hot spot speed of sound. Temperature and pressure rise together within the hot spot. Localized high pressure, relative to that in the cold neighboring gas, is necessary to create the pressure gradient source of induced mechanical motion (both fluid speed and acoustic disturbances). Gas expelled from the boundary of the hot spot (the "piston effect") is the source of mechanical disturbances in the unheated environmental gas. The expelled gas Mach number, defined with respect to the cold gas speed of sound will be exceptionally small when the energy deposition is sufficiently small relative to the quantitative limitation referred to above. The resulting mechanical

disturbances in the cold environment are linear acoustic waves. Larger energy deposition within the quantitative limitation is associated with much larger expelled gas Mach numbers and significantly stronger shock wave propagation in the cold environmental gas. Beyond the quantitative limitation referred to above, the heating process is fully compressible, characterized by a very large internal Mach number. The asymptotic theory demonstrates that this type of thermomechanical response to energy deposition is the source of strong blast waves [23] in the unheated external environment.

4.2 Summary and Conclusions

The theoretical framework in Ref. 2 has been used in the present work to quantify the thermomechanical response of a reactive gas affected by a localized exothermic chemical reaction. The extension is formulated for a subcritical perfect gas with one-step, high activation energy exothermic kinetics. The asymptotic formulation demonstrates that the thermomechanical response of a reactive gas to localized, rapid⁴ chemical heat addition is similar in nature to that for an inert gas with external heating. Nearly inertially-confined heating occurs only when the chemical heat release and the high activation energy are quantitatively restricted. Within that limitation one finds linear acoustic wave generation for the smallest range of energy addition and stronger wave generation for more significant energy deposition.

Numerical solutions to the equations describing the nearly-inertially confined reaction-generated heat addition process show that a spatially distributed reaction wave appears spontaneously in the hottest portion of the hot spot, and propagates through the relatively slowly moving fluid at a supersonic speed, relative to the hot gas speed of sound. As the front nears the much colder boundary of the hot spot it decelerates significantly and steepens considerably. The configuration evolves toward a discontinuous front separating hot, high-pressure, burned gas on

⁴ Heating time-scale short compared to the local acoustic time.

one side from cold, low pressure reactant on the other side. Although the pressure, temperature and reactant concentration jumps across the front are reminiscent of a reactive shock wave, the front does not propagate at a supersonic speed relative to the unburned cold reactant near the boundary of the hot spot. In fact, during the relevant heating time scale the entire process occurs in a nearly incompressible medium. The heating process on the time scale of interest has created an ephemeral, isolated, burned out, hot, high pressure spot embedded in a cold unreacted, lower pressure gas. The large pressure gradient at the front induces a local positive radial fluid velocity. Fluid expelled from the hot spot boundary acts as source of mechanical disturbances propagating into the neighboring cold gas. The amplitude of those disturbances depends upon the energy addition level during the reactive phase of the hot spot. Of course there must be a subsequent longer time-scale process in which the pressure differential is relaxed. One can anticipate that a combustion wave will be driven into the neighboring reactant.

This type of asymptotic formulation and analysis can provide fundamental insights into the sources of mechanical disturbances within a LRE chamber containing a turbulent reacting flow, consisting of spatially distributed regions of transient combustion. In addition the results define crucial length and time scales, as well as dominant physico-chemical mechanisms. These outcomes can inform the numerical modeler seeking to develop code capable of resolving transient, compressible, reactive turbulent flows.

Acknowledgment: This research has been supported by a Phase I STTR contract FA9550-10-C-0088 sponsored by the Air Force Research Laboratory (AFRL). The author appreciates the support of the Program Manager, Dr. Mitat Birkan, of AFOSR.

Bibliography

1. Oppenheim AK, Soloukhin RI (1973) Experiments in the gasdynamics of explosions. *Annu Rev Fluid Mech* 5:31-55
2. Kasoy DR (2010) The response of a compressible gas to extremely rapid transient, spatially resolved energy addition: An asymptotic formulation. *J Eng Math* 68:249-262
3. Kevorkian J, Cole JD (1981) *Perturbation methods in applied mathematics. Applied Mathematical Sciences.* 34, p.482, Springer-Verlag, New York
4. Clarke JF, Kasoy DR, Riley N (1986) On the direct initiation of a plane detonation. *Proc Roy Soc Lond A* 408:129-148
5. Clarke J.F, Kasoy DR, Maharzi NE, Riley N, Vasantha R (1990) On the evolution of plane detonations. *Proc Roy Soc Lond A* 429:259-283
6. Mazaheri K (1997) Mechanism of the onset of detonation in direction initiation. Department of Mechanical Engineering, McGill University, Canada
7. Eckett CA, Quirk JJ, Shepherd JE (1997) An analytical model for direct initiation of gaseous detonation waves, in 21st International Symposium on Shock Waves, 2100
8. Eckett CA, Quirk JJ, Shepherd JE (2000) The role of unsteadiness in direct initiation of gaseous detonations. *J Fluid Mech* 421:147-183
9. Jackson TL, Kapila AK, Stewart DS (1989) Evolution of a reaction center in an explosive material. *SIAM J App Math* 49:452-458
10. Short M (1995) The initiation of detonation from general non-uniformly distributed initial conditions. *Phil Trans R Soc Lond A* 353:173-203
11. Short M (1997) On the critical conditions for the initiation of a detonation in nonuniformly perturbed reactive fluid. *SIAM J Appl Math* 57:1242-1280

12. Sileem A, Kassoy DR, Hayashi AK (1991) Thermally initiated detonation through deflagration to detonation transition. *Proc Roy Soc Lond A* 435:459-482
13. Kassoy DR, Kuehn JA, Nabity MW, Clarke JF (2008) Detonation initiation on the microsecond time scale: DDTs. *Combust Theory and Model* 12:1009-1047
14. Kassoy DR, Kuehn JA, Nabity MW, Clarke JF (2005) Modeling detonation initiation on the microsecond time scale. *AIAA 2005-1169 43rd Aerospace Science Meeting and Exhibit*, Jan 10-13, 2005, Reno, NV, 2005-1169
15. Regele JD, Kassoy DR, Vasilyev OV (2011) submitted, *Comb. Modeling and Theory*
16. Gu XJ, Emerson DR, Bradley D (2003) Modes of reaction front propagation from hot spots. *Comb Flame* 133:63-74.
17. Oran ES, Gamezo VN (2007) Origins of the deflagration-to-detonation transition in gas-phase combustion. *Combustion and Flame* 148:4-47.
18. Oppenheim AK (2006) *Dynamics of combustion systems*. Springer, New York
19. Zeldovich YB (1980) Regime classification of an exothermic reaction with nonuniform initial conditions. *Comb Flame* 39:211-214
20. Zeldovich Y, Librovich G, Makhviladze G, Sivashinsky G (1970) Development of detonation in a non-uniformly preheated gas. *Astronautica Acta* 15:313-321
21. Kapila AK, Schwendeman DW, Quirk JJ, Hawa T (2002) Mechanism of detonation formation due to a temperature gradient. *Comb Theory Modeling* 6:533-594
22. Clarke JF, Kassoy DR, Riley N (1984) Shocks generated in a confined gas due to rapid heat addition at the boundary. II. Strong shock waves. *Proc Roy Soc Lond A* 393:331-351
23. Whitham GB (1974) *Linear and nonlinear waves*. Wiley Interscience, New York